The Thesis Committee for David Edward Gagnon
certifies that this is the approved version of the following thesis:

Bispectral Analysis of Nonlinear Acoustic Propagation

APPROVED BY

SUPERVISING COMMITTEE:

Mark F. Hamilton, Supervisor

Mark S. Wochner

Bispectral Analysis of Nonlinear Acoustic Propagation

by

David Edward Gagnon, B.A.; B.S.E.E.

THESIS

Presented to the Faculty of the Graduate School of

The University of Texas at Austin

in Partial Fulfillment

of the Requirements

for the Degree of

MASTER OF SCIENCE IN ENGINEERING

THE UNIVERSITY OF TEXAS AT AUSTIN

May 2011

This thesis is dedicated to my wife, Nicole. I think she's really neat.

Acknowledgments

I would like to thank my advisor, Mark Hamilton, for his extensive help through the process of research and thesis writing. Mark Wochner provided invaluable assistance with the nonlinear propagation code. Yurii Ilinskii and the late Melvin Hinich are gratefully acknowledged for their insights on statistics. Funding for this project was provided by the Applied Research Laboratories at The University of Texas at Austin through the McKinney Fellowship in Acoustics. I am also grateful for Marcia Isakson's support and patience after the conclusion of the McKinney Fellowship while I worked in her lab and continued writing this thesis.

Bispectral Analysis of Nonlinear Acoustic Propagation

David Edward Gagnon, M.S.E.
The University of Texas at Austin, 2011

Supervisor: Mark F. Hamilton

Higher-order spectral analysis of acoustical waveforms can provide phase information that is not retained in calculations of power spectral density. In the propagation of high intensity sound, nonlinearity can cause substantial changes in the waveform as frequency components interact with one another. The bispectrum, which is one order higher than power spectral density, may provide a useful measure of nonlinearity in propagation by highlighting spectral regions of interaction. This thesis provides a review of the bispectrum, places it in the context of nonlinear acoustic propagation, and presents spectra calculated as a function of distance for numerically propagated acoustic waveforms. The calculated spectra include power spectral density, quad-spectral density, bispectrum, spatial derivative of the bispectrum, bicoherence, and skewness function.

Table of Contents

List of Figures

List of Symbols

Most symbols used in this thesis are provided here. Some symbols are assigned multiple definitions (such as σ, which can mean standard deviation or non-dimensional distance), but intended usage is clarified in the text.

b	bicoherence
b_n	n^{th} harmonic coefficient
B_n	n^{th} normalized harmonic coefficient
c_0	small-signal sound speed
c_p	specific heat at constant pressure
c_v	specific heat at constant volume
C	covariance function
$E[\cdot]$	expected value of $[\cdot]$
f	frequency
$f(\cdot), f'$	function and its derivative
f_0	center frequency
I	intensity
j	$\sqrt{-1}$
$\Im[\cdot]$	imaginary part of $[\cdot]$
k	record number
K	number of data records
l, m, n	vector indices
N	data record length

$O[\cdot]$	order of $[\cdot]$
p	acoustic pressure
P	coherency index or non-dimensional pressure p/p_0
Q_{p^2p}	quad-spectral density
R	correlation function
$\Re[\cdot]$	real part of $[\cdot]$
s	skewness function
S_{xx}	power spectral density of signal x
S_{xy}	cross-spectral density of signals x and y
S_{xxx}	bispectrum of signal x
S_{x^n}	n^{th}-order spectrum
t	time
T	time window
x	propagation distance
x, y, z	time-domain signals
X, Y, Z	frequency-domain signals
Z	bifrequency spectral density
β	coefficient of nonlinearity
γ	skewness
δ	Dirac delta function or diffusivity of sound
ε	Mach number
Γ	Gol'dberg number
κ	thermal conductivity
μ	shear viscosity
μ_B	bulk viscosity
μ_x	mean value of signal x

ψ	time delay
θ	non-dimensional retarded time $\omega_0\tau$
ρ_0	ambient mass density
σ	non-dimensional distance scaled to shock formation distance
σ^2	variance
τ	retarded time
ω	$2\pi f$, angular frequency
Ω	domain
ξ^2_{xy}	coherence function

Chapter 1

Introduction

Spectral techniques are used to reveal information about frequency content from time-series data. Although the second-order power spectral density is found frequently in engineering analysis, spectra of higher order that can incorporate larger numbers of signals and frequency components also exist. The spectrum at the third order is known as the bispectrum, which shows phase relationships in data from three signals on two frequency axes.

This thesis seeks to apply the bispectrum to nonlinear sound propagation. In linear acoustics, different frequency components may attenuate at different rates, but no energy moves from one frequency to another. However, linear acoustics requires the small-signal assumption that all field variables can be modeled as infinitesimal fluctuations about their mean values. When this assumption no longer holds, additional terms in the equations must be considered to account for nonlinear effects. More details concerning the analytic theory of nonlinear acoustics will be considered in Sec. 3.1.

Nonlinear acoustics has many applications, and the motivation for the present research was found in the propagation of jet engine noise. For certain aircraft, pressure from jet turbulence can reach levels at which nonlinear

behavior becomes substantial, dramatically affecting the frequency content of the signal that reaches the listener. This signal is complicated by the inherent randomness in the turbulence. Thus, it can be difficult to distinguish between patterns in the initial noise waveform and actual nonlinearity in the propagation. Power spectral densities show frequency content without phase information, which can suggest nonlinearity when comparisons are made near and far from the source. At the next order, however, the bispectrum retains information about phase relationships between frequency components. As a result, bispectral analysis provides additional information on nonlinearity in data obtained at a single geographic point. To that end, this thesis lays a foundation for applying bispectral analysis to nonlinearly-propagated sound waves.

1.1 Jet Noise

As was mentioned, high-power jet engines, such as those used in military aircraft, generate turbulence that radiates sound at high amplitude. Research in recent decades has worked to accurately model aircraft noise and quantify the effects of nonlinearity in propagation.

Morfey and Howell [1] analyzed flyover noise tests and found that high frequencies (5–10 kHz) attenuate much less than expected according to linear models of propagation. Through a statistical analysis of nonlinear noise propagation, they showed that nonlinear effects provide a reasonable explanation for this anomalously low attenuation. In the process, they introduced a "spectral

transfer term" Q_{p^2p}, which is the imaginary part of a cross-spectral density between pressure and pressure squared. They used this term to indicate the presence of nonlinearity.

Falco [2], who refers to Q_{p^2p} as the quad-spectral density, further explored the physical significance of this quantity. Q_{p^2p} may be regarded as a representation of the direction of energy flow into or out of a frequency band, depending on the sign.

More recent tests have further corroborated the idea that nonlinearity is responsible for the lower than expected attenuation in the upper frequencies of jet noise. For clarity in this discussion, we introduce several papers by Gee et al. in chronological order and will refer to them by year of publication: Gee et al. 2004 [3], Gee et al. 2005 [4], Gee et al. 2007 [5], Gee et al. 2008 [6], and Gee et al. 2010 [7]. Various other authors contributed to specific papers.

In two papers, Gee et al. 2004 and 2008 [3, 6] measured pressure fields from grounded jets at a variety of angles and ranges for several different engine power levels. Power spectral densities were compared between data, linear predictions, and nonlinear predictions, and it was shown that nonlinear effects are significant at both high and medium power levels. These effects were observed at a range of angles, not just at peak radiation angle. It was also concluded that the assumption of Gaussian statistics for the source waveform does not adequately model loud jet noise, and that phase information may be significant for analysis and prediction of noise propagation.

Also relating to the significance of wave structure, Gee et al. 2007 [5] looked specifically at waveform time-derivative statistics as an indicator for "crackle," a percussive sound often described as annoying to listeners. Crackle was first addressed by Ffowcs Williams et al. [8], who used waveform skewness as an indicator of the presence of crackle. However, Gee et al. 2007 [5] showed that skewness alone is insufficient to account for the existence of crackle, as it is possible for waveforms with high skewness to exhibit no crackle. They also found that the statistics of the time derivative of the waveform differ substantially between cases with and without crackle, suggesting that such statistics indicate the presence of crackle more accurately than do statistics of the waveform itself.

Gee et al. 2005 [4] have also looked at wave structure through bispectral analysis. They calculated bicoherences of the data given in Gee et al. 2004 [3] and found that plots of bicoherence tend to exhibit higher values when nonlinearity is present.

More recently, Gee et al. 2010 [7] applied bispectral analysis to model-scale jet noise. They calculated both power spectral density and bicoherence at a variety of angles and distances from the turbulence caused by the jet. The bicoherence enabled them to distinguish between nonlinear and geometric near-field effects, which was not possible with power spectral density alone. It was recommended that further research be conducted on bispectrum evolution as it relates to nonlinear propagation.

This thesis supports that goal in gathering information about bispectral

analysis of nonlinear acoustic waves and providing examples of spectra for waveforms that have been numerically propagated with known conditions.

1.2 Propagation Codes

Although analytical solutions have been obtained for finite amplitude sound radiated by monofrequency sources, as will be discussed in Sec. 3.1, adding multiple frequency components with random phase causes the problem to become analytically intractable. As a result, we turn to numerical solutions to describe the nonlinear propagation of complicated waveforms. The present review is limited to numerical solutions of the Burgers equation which describe the essential physics of nonlinear propagation and form the basis of the numerical simulations employed by the author.

Approaches to modeling the Burgers equation can be divided into three categories: fully frequency domain, hybrid time-frequency domain, and fully time domain. For the present review, we follow the review by Ginsberg and Hamilton [9], which contains greater detail on computational methods for nonlinear propagation.

In the frequency-domain approach, a Fourier series representation is used to describe the wave structure, provided that the waveform is periodic in nature. Fenlon [10] developed a numerical procedure for calculating harmonic amplitude and phase through coupled spectral equations. Later, Korpel [11] derived coupled spectral equations to account for arbitrary absorption and dispersion. For waveforms with limited frequency content, performing calcu-

lations entirely in the frequency domain can be very efficient. Noise, however, requires prohibitive computation time in this approach.

A foundational hybrid time-frequency code developed by Pestorius and Blackstock [12] has come to be known as the Pestorius algorithm. It was designed to handle shock behavior and boundary layer attenuation and dispersion for arbitrarily-shaped input waveforms, especially noise. The algorithm alternated small steps in the time domain for weak shock propagation with correction steps in the frequency domain for attenuation and dispersion, all while keeping track of shock locations. This approach was validated with an air-filled progressive-wave tube experiement, and good agreement was observed between the experimental and computed results for a noise waveform input.

Nonlinear propagation has also been modeled exclusively in the time domain with a finite-difference algorithm developed by Lee and Hamilton [13]. This code modeled the pressure field in pulsed sound beams from axisymmetric sources in homogeneous, thermoviscous fluids. Relaxation and focusing techniques were also discussed. The algorithm was adapted for one-dimensional propagation with relaxation and medium inhomogeneity by Cleveland, Hamilton, and Blackstock [14]. It compared very well to weak shock theory and two other mixed time-frequency codes [15].

Because it is convenient for propagating finite amplitude noise, a time-domain approach was used in this thesis. This code, called BurgersTX, is available at `http://people.bu.edu/robinc/kzk/burgers.html`.

1.3 Overview

The remainder of this work is divided as follows. Chapter 2 describes the statistical framework for bispectral analysis, with special attention given to normalization conventions. In Chap. 3, connections are drawn between bispectral analysis and nonlinear acoustics, especially in the prediction of energy flow between spectral components. Considerations for numerical modeling are explained in Chap. 4. The results of propagation and bispectral analysis for several types of waveforms are then shown in Chap. 5. Suggestions for future work are contained in Chap. 6.

Chapter 2

The Bispectrum

The bispectrum is one tool among a set of statistical functions known as higher-order spectra, also known as polyspectra. Second-order statistics, such as the power spectrum and autocorrelation, are used frequently in signal processing. However, second-order statistics can only provide a full statistical description of a process when that process is Gaussian and linear, and they retain no phase information [16]. Spectra of order greater than two are therefore used to identify nonlinearities, phase relationships, and non-Gaussian behavior in time series [16]. The third-order spectrum, also known as the bispectrum, is discussed here. Where possible, we will follow the notation conventions of Bendat and Piersol [17].

2.1 Spectral and Bispectral Densities

The bispectrum is defined as the double Fourier transform of the third-order covariance function of a signal, also known as the third-order cumulant sequence of a signal [16, 18–20]. For clarity, we begin with definitions of second-order quantities and then approach third-order definitions in a similar fashion.

The second-order covariance functions for stationary signals are

$$C_{xx}(\psi) = E\left[(x_k(t) - \mu_x)(x_k(t+\psi) - \mu_x)\right] \tag{2.1a}$$

$$C_{yy}(\psi) = E\left[(y_k(t) - \mu_y)(y_k(t+\psi) - \mu_y)\right] \tag{2.1b}$$

$$C_{xy}(\psi) = E\left[(x_k(t) - \mu_x)(y_k(t+\psi) - \mu_y)\right] \tag{2.1c}$$

where x_k and y_k are time series variables over the index k, t is time, ψ is a time delay, and μ_x and μ_y are the mean values of x_k and y_k, respectively [17]. The time series variables can represent any quantity that varies with time, but in this thesis x_k and y_k will generally refer to pressure signals. A covariance function describes how well signal components at one time match signal components at another time. Note that for nonstationary signals, μ would be a function of time, but in this thesis, we will work only with stationary signals because we are interested in jet engine noise in its steady state.

When ψ is zero, C_{xx} becomes the variance for x, C_{yy} becomes the variance for y, and C_{xy} becomes the covariance between x and y [17].

The covariance function closely resembles the correlation function:

$$R_{xx}(\psi) = E\left[x_k(t)x_k(t+\psi)\right] \tag{2.2a}$$

$$R_{yy}(\psi) = E\left[y_k(t)y_k(t+\psi)\right] \tag{2.2b}$$

$$R_{xy}(\psi) = E\left[x_k(t)y_k(t+\psi)\right] \tag{2.2c}$$

The difference between C and R occurs in the removal of the mean from the variable of interest. For variables with zero mean, C and R can be used interchangeably.

The power spectrum is the Fourier transform of the covariance function:

$$S_{xx}(\omega) = \int_{-\infty}^{\infty} C_{xx}(\psi) e^{-i\omega\psi}\, d\psi \tag{2.3a}$$

$$S_{yy}(\omega) = \int_{-\infty}^{\infty} C_{yy}(\psi) e^{-i\omega\psi}\, d\psi \tag{2.3b}$$

$$S_{xy}(\omega) = \int_{-\infty}^{\infty} C_{xy}(\psi) e^{-i\omega\psi}\, d\psi \tag{2.3c}$$

We now follow a similar line of reasoning for the bispectrum. At third order, the covariance functions for stationary signals are

$$C_{xxx}(\psi_1, \psi_2) = E\left[(x_k(t) - \mu_x)(x_k(t+\psi_1) - \mu_x)(x_k(t+\psi_2) - \mu_x)\right] \tag{2.4a}$$

$$C_{yyy}(\psi_1, \psi_2) = E\left[(y_k(t) - \mu_y)(y_k(t+\psi_1) - \mu_y)(y_k(t+\psi_2) - \mu_y)\right] \tag{2.4b}$$

$$C_{zzz}(\psi_1, \psi_2) = E\left[(z_k(t) - \mu_z)(z_k(t+\psi_1) - \mu_z)(z_k(t+\psi_2) - \mu_z)\right] \tag{2.4c}$$

$$C_{xyz}(\psi_1, \psi_2) = E\left[(x_k(t) - \mu_x)(y_k(t+\psi_1) - \mu_y)(z_k(t+\psi_2) - \mu_z)\right] \tag{2.4d}$$

where x_k, y_k, and z_k are time series variables with respective means μ_x, μ_y, and μ_z. If $\mu = 0$, the covariance function again becomes the correlation function:

$$R_{xxx}(\psi_1, \psi_2) = E\left[x_k(t) x_k(t+\psi_1) x_k(t+\psi_2)\right] \tag{2.5a}$$

$$R_{yyy}(\psi_1, \psi_2) = E\left[y_k(t) y_k(t+\psi_1) y_k(t+\psi_2)\right] \tag{2.5b}$$

$$R_{zzz}(\psi_1, \psi_2) = E\left[z_k(t) z_k(t+\psi_1) z_k(t+\psi_2)\right] \tag{2.5c}$$

$$R_{xyz}(\psi_1, \psi_2) = E\left[x_k(t) y_k(t+\psi_1) z_k(t+\psi_2)\right] \tag{2.5d}$$

From the covariance function, the bispectra are obtained by taking the

double Fourier transform:

$$S_{xxx}(\omega_1, \omega_2) = \int_{-\infty}^{\infty} \int_{-\infty}^{\infty} C_{xxx}(\psi_1, \psi_2) e^{-i(\omega_1 \psi_1 + \omega_2 \psi_2)} \, d\psi_1 d\psi_2 \tag{2.6a}$$

$$S_{yyy}(\omega_1, \omega_2) = \int_{-\infty}^{\infty} \int_{-\infty}^{\infty} C_{yyy}(\psi_1, \psi_2) e^{-i(\omega_1 \psi_1 + \omega_2 \psi_2)} \, d\psi_1 d\psi_2 \tag{2.6b}$$

$$S_{zzz}(\omega_1, \omega_2) = \int_{-\infty}^{\infty} \int_{-\infty}^{\infty} C_{zzz}(\psi_1, \psi_2) e^{-i(\omega_1 \psi_1 + \omega_2 \psi_2)} \, d\psi_1 d\psi_2 \tag{2.6c}$$

$$S_{xyz}(\omega_1, \omega_2) = \int_{-\infty}^{\infty} \int_{-\infty}^{\infty} C_{xyz}(\psi_1, \psi_2) e^{-i(\omega_1 \psi_1 + \omega_2 \psi_2)} \, d\psi_1 d\psi_2 \tag{2.6d}$$

Higher-order spectra exist in several forms, so we must specify that the bispectrum is a second-order cumulant spectrum. Provided that $x(t)$ is a stationary, real random process, Eqs. (2.1) and (2.4) describe the second- and third-order cumulants, respectively [16, 18]. Moment spectra also exist, but they are typically applied to deterministic signals, whereas cumulant spectra are typically applied to stochastic signals [16]. Cumulant spectra above second order are zero for Gaussian processes, so nonzero values indicate the extent to which a process is non-Gaussian [18]. Also, for the sum of two independent, stationary processes with nonzero means, the cumulant spectrum is equal to the sum of the two individual cumulant spectra [16]. That is, cumulant spectra for such processes add linearly, which is not true of moment spectra. Furthermore, Brillinger [21] has shown that the requirements for assuming ergodicity are more easily satisfied in the estimation of cumulant spectra than of moment spectra. When a process is ergodic, time-average operations can be considered to have the same properties as ensemble-average operations. For a real stationary random process, both moments and cumulants depend only on time

delays [16].

Although we have made a formal distinction between moment and cumulant spectra, they are not always different from one another in practice. For a zero-mean random variable, the moments and cumulants are identical below fourth order. This means that the bispectrum can technically be both a moment spectrum and a cumulant spectrum, provided that the variable of interest has a mean of zero [16].

We can also define the bispectrum in terms of Fourier components, which is the chosen method of Haubrich [22] and Kim and Powers [23]. For a time signal $x_k(t)$ where k is the realization number, the Fourier transform over window length T is given by

$$X_k(f,T) = \int_0^T x_k(t) e^{-j2\pi ft}\, dt \tag{2.7a}$$

$$Y_k(f,T) = \int_0^T y_k(t) e^{-j2\pi ft}\, dt \tag{2.7b}$$

$$Z_k(f,T) = \int_0^T z_k(t) e^{-j2\pi ft}\, dt \tag{2.7c}$$

according to notation conventions of Bendat and Piersol [17]. The frequency-domain representation can then be used to find the power spectral density,

$$S_{xx}(f) = \lim_{T\to\infty} \frac{1}{T} E\left[X_k^*(f) X_k(f)\right] \tag{2.8a}$$

$$S_{yy}(f) = \lim_{T\to\infty} \frac{1}{T} E\left[Y_k^*(f) Y_k(f)\right] \tag{2.8b}$$

$$S_{xy}(f) = \lim_{T\to\infty} \frac{1}{T} E\left[X_k^*(f) Y_k(f)\right] \tag{2.8c}$$

Equations (2.8) are often called the power spectra of a signal (or cross-power spectrum in the case of S_{xy}), but it is more technically correct to call them power spectral densities. Since time series in this thesis will be acoustic pressures, the appropriate unit for power spectral density is $\mathrm{Pa}^2/\mathrm{Hz}$.

We now use a similar approach to explore the next-higher-order spectrum, or bispectrum. Given the definition of Fourier transform from Eq. (2.7), the bispectrum is

$$S_{xxx}(f_1, f_2) = \lim_{T\to\infty} \frac{1}{T} E\left[X_k^*(f_1 + f_2) X_k(f_1) X_k(f_2)\right] \tag{2.9a}$$

$$S_{yyy}(f_1, f_2) = \lim_{T\to\infty} \frac{1}{T} E\left[Y_k^*(f_1 + f_2) Y_k(f_1) Y_k(f_2)\right] \tag{2.9b}$$

$$S_{zzz}(f_1, f_2) = \lim_{T\to\infty} \frac{1}{T} E\left[Z_k^*(f_1 + f_2) Z_k(f_1) Z_k(f_2)\right] \tag{2.9c}$$

$$S_{xyz}(f_1, f_2) = \lim_{T\to\infty} \frac{1}{T} E\left[X_k^*(f_1 + f_2) Y_k(f_1) Z_k(f_2)\right] \tag{2.9d}$$

with units of $\mathrm{Pa}^3/\mathrm{Hz}^2$. We see that the bispectrum is the expected value of interacting frequency components. For the bispectrum to be nonzero, there must be a statistical dependence between the Fourier transforms of signals evaluated at frequencies f_1 and f_2 and at their sum frequency f_1+f_2, which in the context of nonlinear wave interactions is also known as three-wave coupling. Since the Fourier transforms contain negative as well as positive frequencies, the bispectrum is also nonzero when there is a statistical dependence on the difference frequency corresponding to f_1 and f_2. This characteristic indicates that the bispectrum measures phase coherence between frequency components [19]. In the context of acoustics, this coupling is associated with resonant nonlinear

spectral interactions such as those occurring in plane waves in nondispersive fluids, because all frequency components propagate at the same speed.

Power spectral densities are related to familiar statistical parameters such as variance and skewness. Variance is given in several forms, for example,

$$\sigma_x^2 = E\left[x_k^2(t)\right] = \int_{-\infty}^{\infty} S_{xx}(f)\, df = C_{xx}(0) \tag{2.10}$$

and we see that the variance is equivalent to the second-order moment and cumulant [4, 16, 21]. At the next order we have the skewness

$$\gamma_x = E\left[x_k^3(t)\right] = \int_{-\infty}^{\infty}\int_{-\infty}^{\infty} S_{xxx}(f_1, f_2)\, df_1 df_2 = C_{xxx}(0,0) \tag{2.11}$$

and we see that the third-order cumulant of a signal is similarly represented by the bispectrum.

Equations (2.8) and (2.9) will be significant later in this thesis as we use them to calculate the power spectral density and bispectral density, respectively.

2.2 Normalizations

The bispectrum is often presented not in its raw form but rather in a normalized form called the "bicoherence" [4, 19, 22, 23], "bicoherency" [16], "bicoherence index" [18], or "skewness function" [4, 24]. Depending on the reference, such terms may refer to slightly different normalizations, so one must take care to distinguish them. In this section we will highlight the distinctions between these various forms.

Normalizations are not always necessary, but they can be useful for finer distinctions in data analysis. Because the bispectrum depends on amplitudes of spectral components, a peak in the bispectrum could be interpreted as a strong coherence between weak spectral components or a small coherence between strong spectral components. Reducing the influence of the spectral amplitudes via normalization can therefore aid in data interpetation [23]. Furthermore, the bispectrum is nonzero for non-Gaussian processes, but it does not distinguish between processes that are nonlinear (and inherently non-Gaussian) and processes that are linear and happen to also be non-Gaussian. For linear systems, the magnitude of the bicoherence is constant for all frequencies, whereas the bicoherence of nonlinear systems is frequency dependent [16, 18]. Identifiable harmonically-related peaks in the bicoherence may also indicate the relative amount of phase coupling [18], though the bicoherence may serve more reliably as an indicator rather than a quantifier of phase coupling when the bicoherence is estimated parametrically [16]. The normalization used by Kim and Powers [23] limits values of the bicoherence to between 0 and 1, thus enabling the interpretation of bicoherence as a fraction of power involved in phase coupling. However, the validity of that normalization is disputed [24] and will be discussed later in this section.

We now consider specific formulas of normalized spectra. The most general of these is the coherency index, which compares a higher-order spectrum of arbitrary order n to its power spectrum for every relevant combination of frequency components. According to Nikias and Petropulu [16], this index

is defined as

$$P_{x^n}(\omega_1,\omega_2,\ldots,\omega_{n-1}) \triangleq \frac{S_{x^n}(\omega_1,\omega_2,\ldots,\omega_{n-1})}{[S_{xx}(\omega_1)\cdot S_{xx}(\omega_2)\cdots S_{xx}(\omega_{n-1})\cdot S_{xx}(\omega_1+\omega_2+\cdots+\omega_{n-1})]^{\frac{1}{2}}} \tag{2.12}$$

The coherence function, which applies to cross-spectral densities, is given by Bendat and Piersol [17] as

$$\xi^2_{xy}(f) = \frac{|S_{xy}(f)|^2}{S_{xx}(f)S_{yy}(f)} \tag{2.13}$$

For both Eqs. (2.12) and (2.13), a statistical function of interest is divided by a product of power spectral densities. However, Eq. (2.13) is limited to second-order spectra, is a function of only one frequency, and is bounded by 0 and 1. Equation (2.12), on the other hand, applies to higher-order spectra at multiple frequencies without an *a priori* bound. We draw attention to these two equations to show that coherence generally involves the comparison of a statistical function with its corresponding power spectral density or densities, but there are differing views on how coherence is calculated. With regard to acoustics, statistical coherence may be loosely interpreted as a ratio of energies in the sound wave.

The bicoherence model put forth by Kim and Powers [23] provides a normalization that applies to the bispectrum and also remains bounded between 0 and 1. They accomplish this by incorporating a bifrequency spectral density

$$Z(f_1,f_2) = \lim_{T\to\infty}\frac{1}{T}E\left[|X_k(f_1)X_k^*(f_2)|^2\right] \tag{2.14}$$

where values of X at two different frequencies are combined into a single expectation [4]. The overall bicoherence then becomes

$$b(f_1, f_2) = \frac{|S_{xxx}(f_1, f_2)|}{\sqrt{Z(f_2, f_2)S_{xx}(f_1 + f_2)}} \tag{2.15}$$

or, in expanded form,

$$b(f_1, f_2) = \frac{|E\left[X_k(f_1)X_k(f_2)X_k^*(f_1 + f_2)\right]|}{\sqrt{E\left[|X_k(f_1)X_k(f_2)|^2\right] E\left[|X_k(f_1 + f_2)|^2\right]}} \tag{2.16}$$

To estimate this bicoherence digitally, Kim and Powers give the formula

$$\hat{b}(m, n) = \frac{\left|\frac{1}{K}\sum_{k=1}^{K} X_k(m)X_k(n)X_k^*(m + n)\right|}{\left[\frac{1}{K}\sum_{k=1}^{K} |X_k(m)X_k(n)|^2\right]^{1/2} \left[\frac{1}{K}\sum_{k=1}^{K} |X_k^*(m + n)|^2\right]^{1/2}} \tag{2.17}$$

where K is the number of data records of length N points, X is an individual record, and m and n are vector indices that can apply to time or frequency. Each X is a discrete Fourier transform given as

$$X_k(m) = \frac{1}{N}\sum_{n=1}^{N} x_k(n)e^{-i2\pi mn/N} \tag{2.18}$$

where $m = 1, \cdots, N/2$ and $k = 1, \cdots, K$.

Equation (2.16) is bounded by 0 and 1 according to the Schwarz inequality, and Kim and Powers suggest that the squared bicoherence can then be interpreted as the fraction of power due to three-wave coupling [23].

Although Kim and Powers' normalization is found frequently in engineering signal processing literature, Hinich and Wolinsky [24] point out that this normalization depends on the resolution bandwidth of the sample bispectrum. Instead, they recommend the normalization put forth by

Brillinger [21] and also used by Haubrich [22], Hinich [25], and Hinich with colleagues Clay [26] and Messer [27]. This normalization, which Hinich calls the "skewness spectrum," is

$$\hat{s}(f_1, f_2) = \frac{|S_{xxx}(f_1, f_2)|}{\sqrt{S_{xx}(f_1)S_{xx}(f_2)S_{xx}(f_1 + f_2)}} \tag{2.19}$$

or, in expanded form,

$$\hat{s}(f_1, f_2) = \frac{|E\left[X_k(f_1)X_k(f_2)X_k^*(f_1 + f_2)\right]|}{\sqrt{E\left[|X_k(f_1)|^2\right] E\left[|X_k(f_2)|^2\right] E\left[|X_k(f_1 + f_2)|^2\right]}} \tag{2.20}$$

The skewness spectrum is consistent with the coherency index described in Eq. (2.12), in which the main statistical function is divided by power spectral densities. It is more conventional than the bicoherence of Kim and Powers in the sense that it does not require any bifrequency spectral density but rather relies on well established statistical functions. This adherence to convention is not the primary reason for using the skewness function, however. Hinich and Wolinsky argue for the skewness spectrum on statistical grounds, showing that the Kim and Powers normalization depends on the resolution bandwidth of the sample bispectrum. This means that with the Kim and Powers normalization, the number of data points per unit frequency has an effect on the statistical significance of values in the bicoherence, causing uncertainty in interpretation.

Another strength of the skewness spectrum is that it highlights the relationship between the bispectrum and the skewness of a time series. Average skewness can be calculated as

$$\bar{\gamma} = (2\pi)^{-2} \iint_{\Omega} \frac{|S_{xxx}(\omega_1, \omega_2)|^2}{S_{xx}(\omega_1)S_{xx}(\omega_2)S_{xx}(\omega_1 + \omega_2)}\, d\omega_1 d\omega_2 \tag{2.21}$$

where Ω is the principal domain [25]. Inserting Eq. (2.19) into Eq. (2.21), we find that

$$\bar{\gamma} = (2\pi)^{-2} \iint_{\Omega} \hat{s}^2(f_1, f_2)\, d\omega_1 d\omega_2 \tag{2.22}$$

showing that the skewness spectrum provides a frequency-based distribution of the skewness.

In Chap. 5 of this thesis we will plot both the bicoherence and the skewness functions of simulated noise in order to provide a visual comparison. The expanded forms of these functions are given in Eqs. (2.16) and (2.20).

In this chapter we have developed equations for the power spectral density, bispectrum, bicoherence, and skewness function. Several more spectral quantities will be introduced in the next chapter, where we connect these concepts to nonlinear acoustical propagation.

Chapter 3

Analysis of Nonlinear Propagation

Having established the mathematical framework for bispectral analysis in Chap. 2, we now apply it to nonlinear acoustic wave propagation. In linear propagation, frequency components may be absorbed, but no new frequency components are generated. However, in nonlinear propagation, energy can be transferred from one frequency component to another, resulting in an evolving spectral distribution of energy. The statistics of the waveform, then, can be used to indicate the presence of nonlinear behavior. Here, we explore the evolution of a propagating wave's power spectrum and then we similarly build a framework for describing the evolution of its bispectrum.

3.1 Basic Formulas in Nonlinear Acoustics

In this section, we review equations that describe properties of nonlinear progressive waves that relate to the present work, relying heavily on Blackstock, Hamilton, and Pierce [28]. Fundamentals of nonlinear acoustics are also explained in a paper by Hamilton [29] and texts by Beyer [30] and Naugolnykh and Ostrovsky [31], which may further assist the reader.

For plane progressive waves in a lossless fluid, propagation in the posi-

tive x direction is given by the reduced wave equation

$$\frac{\partial u}{\partial t} + (c_0 + \beta u)\frac{\partial u}{\partial x} = 0 \tag{3.1}$$

where u is particle velocity, t is time, c_0 is the small-signal sound speed, and β is the coefficient of nonlinearity. From Eq. (3.1), which is exact for a perfect gas, it can be found that for a point of constant phase on the waveform, the propagation speed of any point on the waveform is a function of the local particle velocity:

$$\left.\frac{dx}{dt}\right|_u = c_0 + \beta u \tag{3.2}$$

As a result of this dependence, peaks propagate faster than troughs, and the waveform steepens in regions of compression and becomes less steep in regions of rarefaction. Examples of this process can be observed in the figures of Chap. 5, which includes example waveforms at various stages of distortion.

Shocks appear at points on the waveform where vertical tangents form, and therefore shock formation is associated with infinite slope in the waveform. The distance at which shocks form is found from the solution to Eq. (3.1). For a source condition specified at $x = 0$ such that $u(0, t) = f(t)$,

$$u = f\left(t - \frac{x}{c_0 + \beta u}\right) \tag{3.3}$$

is the implicit solution. The slope is found by writing the time derivative of Eq. (3.3) as follows:

$$\frac{\partial u}{\partial t} = \frac{f'}{1 - \beta x f'/(c_0 + \beta u)^2} \tag{3.4}$$

where the prime indicates the derivative of f with respect to its argument. Infinite slope occurs when the denominator of Eq. (3.4) reaches zero. Thus, the distance at which a vertical tangent forms, x_{vt}, is

$$x_{\mathrm{vt}} = \frac{(c_0 + \beta u)^2}{\beta f'} \tag{3.5}$$

The shock formation distance is then defined as the minimum distance at which Eq. (3.5) is satisfied. If $\beta|u| \ll c_0$, which can be reasonably assumed in much of nonlinear acoustics,[1] the smallest value of Eq. (3.5) becomes

$$\bar{x} = \frac{c_0^2}{\beta f'_{\max}} \tag{3.6}$$

which depends on the maximum slope of the time waveform at the source. For a sinusoidal source such that $u(0,t) = u_0 \sin \omega t$, the maximum positive slopes occur at zero-crossings and have the value $f'_{\max} = \omega u_0$, and thus Eq. (3.6) becomes

$$\bar{x} = \frac{1}{\beta \varepsilon k} \tag{3.7}$$

where $\varepsilon = u_0/c_0$ is the acoustic Mach number and $k = \omega/c_0$ is the wavenumber. For progressive plane waves, and for $\beta|u|/c_0 \ll 1$ as already assumed, acoustic pressure and particle velocity may be related using the linear impedance relation $p = \rho_0 c_0 u$, where p is the acoustic pressure and ρ_0 is the ambient density. As a result, Eq. (3.7) can be rewritten as

$$\bar{x} = \frac{\rho_0 c_0^3}{\beta p_0 \omega} \tag{3.8}$$

[1]For example, if u_0 is the peak particle velocity of a sinusoidal waveform, the value $u_0/c_0 = 10^{-2}$ corresponds to a sound pressure level of 154 dB re 20 μPa in air. The values of β normally used for air and water are 1.2 and 3.5, respectively.

which corresponds to the source condition $p(0,t) = p_0 \sin \omega t$. Equation (3.8) shows that the shock formation distance is inversely proportional to the amplitude and frequency of the wave at the source.

The shock formation distance for a sinusoid provides a convenient length scale for calculations in nonlinear acoustics. The dimensionless coordinate is thus taken to be

$$\sigma = \frac{x}{\bar{x}} = \beta \varepsilon k x \tag{3.9}$$

such that $\sigma = 1$ at the shock formation distance for a sinusoidal source waveform in a lossless fluid. Shock formation may occur earlier or later for other waveforms, but σ still serves as a useful scale for waveforms that are periodic in nature.

The waveform steepening associated with shock formation also corresponds to the generation of harmonics of the source frequency. Analytic solutions have been developed for the sinusoidal source condition. The Fubini solution, which is valid in the pre-shock region ($\sigma < 1$), is in the form of a Fourier series:

$$p(\sigma, \tau) = p_0 \sum_{n=1}^{\infty} B_n(\sigma) \sin n\omega\tau \tag{3.10}$$

where $\tau = t - x/c_0$ is retarded time, the amplitude of the n^{th} harmonic B_n is

$$B_n = \frac{2}{n\sigma} J_n(n\sigma) \tag{3.11}$$

and where J_n is the Bessel function of order n.

The Fubini solution is valid only before shocks form, but weak shock theory enables the development of solutions beyond the shock formation distance. In weak shock theory, it is assumed that dissipation is concentrated at the shocks, such that all other regions of the waveform can still be regarded as lossless, and shock thickness is negligible, such that the change in pressure at the shock can be modeled as a discontinuity.

Using weak shock theory, Blackstock [32] obtained the following result for the harmonic amplitudes in the region $\sigma > 1$:

$$B_n = \frac{2}{n\pi} P_{\mathrm{sh}} + \frac{2}{n\pi\sigma} \int_{\Phi_{\mathrm{sh}}}^{\pi} \cos\left[n(\Phi - \sigma \sin \Phi)\right] \, d\Phi \tag{3.12}$$

where P_{sh} is the dimensionless shock amplitude defined by the relation $P_{\mathrm{sh}} = \sin \sigma P_{\mathrm{sh}}$, with P_{sh} and Φ_{sh} related through $\Phi_{\mathrm{sh}} = \sigma P_{\mathrm{sh}}$.

Shown in Fig. 3.1 are the first five harmonic amplitudes given by Eq. (3.11) for $\sigma < 1$ and by Eq. (3.12) for $\sigma > 1$ [although Eq. (3.12) is equivalent to Eq. (3.11) for $\sigma < 1$ because in the preshock region $P_{\mathrm{sh}} = \Phi_{\mathrm{sh}} = 0$]. In the region $\sigma > 3$, Eq. (3.12) is given approximately by

$$B_n = \frac{2}{n(1+\sigma)} \tag{3.13}$$

which is referred to as the sawtooth solution because of the shape of the waveform. In this sawtooth region the harmonic amplitudes are inversely proportional to distance, the continual decrease with distance being due to energy loss at the shocks.

When losses must be taken into account explicitly, rather than being modeled within the framework of weak shock theory, the Burgers equation

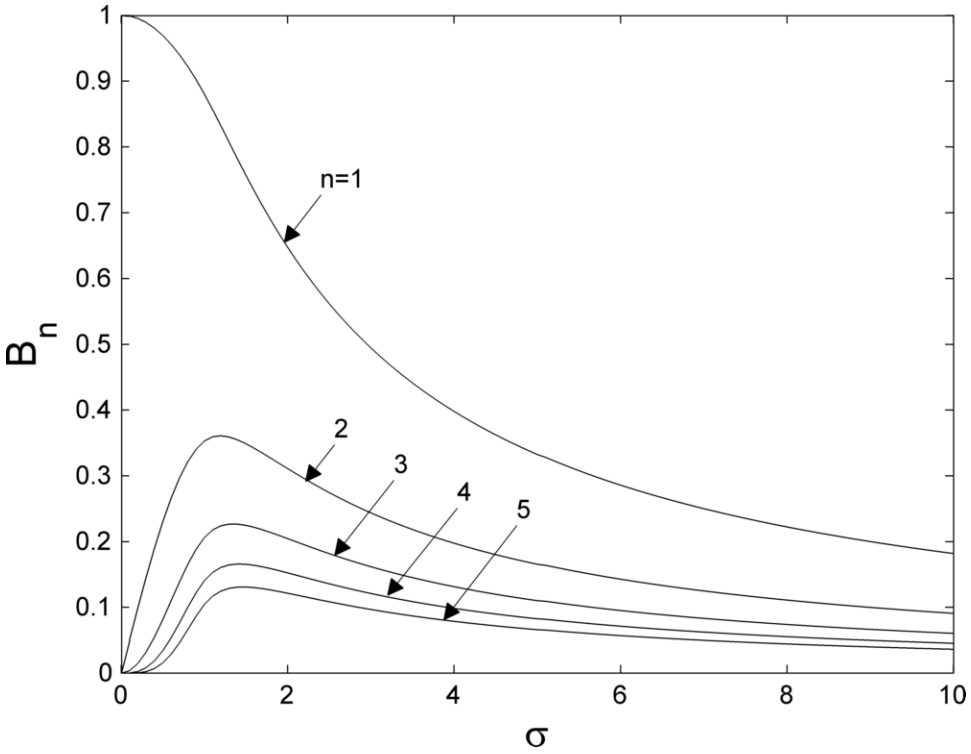

Figure 3.1: Amplitudes B_n for the first five harmonics in a plane wave that starts out as a sinusoid.

may be used:

$$\frac{\partial p}{\partial x} - \frac{\delta}{2c_0^3}\frac{\partial^2 p}{\partial \tau^2} = \frac{\beta p}{\rho_0 c_0^3}\frac{\partial p}{\partial \tau} \tag{3.14}$$

where δ is the diffusivity of sound, defined by

$$\delta = \frac{1}{\rho_0}\left[\frac{4}{3}\mu + \mu_B + \kappa\left(\frac{1}{c_v} - \frac{1}{c_p}\right)\right] \tag{3.15}$$

where μ is shear viscosity, μ_B is bulk viscosity, κ is thermal conductivity, and c_v and c_p are the specific heats at constant volume and constant pressure, respectively. In the limit of vanishing diffusivity, Eqs. (3.11) and (3.12) are solutions of Eq. (3.14). For finite but still very small diffusivity, or alterna-

tively for very large source amplitudes, an important asymptotic solution of Eq. (3.14) for the harmonic amplitudes in the region $\sigma > 3$ is the Fay solution:

$$B_n = \frac{2/\Gamma}{\sinh[n(1+\sigma)/\Gamma]} \tag{3.16}$$

The quantity Γ, which must be large for the Fay solution to be valid ($\Gamma \gg 1$), is referred to as the Gol'dberg number and is defined by

$$\Gamma = \frac{1}{\alpha \bar{x}} \tag{3.17}$$

where $\alpha = \delta\omega^2/2c_0^3$ is the linear thermoviscous attenuation coefficient at the source frequency.

The Burgers equation was solved numerically for all simulations of nonlinear wave propagation presented in Chap. 5.

3.2 Evolution Equations for the Autocorrelation Function and Power Spectral Density

In this section we develop model equations for the evolution of statistical properties of nonlinear acoustic waves as a function of propagation distance. Specifically, evolution equations are derived for the autocorrelation function and the corresponding power spectral density. Various forms of these evolution equations have appeared previously in the literature (see, for example, Menounou and Blackstock [33], and their review of related literature). These derivations are not only useful by themselves, but they lay the foundation for the derivations in Sec. 3.3 of evolution equations at second order for

the covariance function and the corresponding bispectrum. To the author's knowledge, these second-order evolution equtions are new.

To describe the evolution of a sound wave over distance and time, we begin with the lossless form of the Burgers equation, Eq. (3.14), which accounts for the essential physics needed to describe nonlinear propagation of plane acoustic waves prior to shock formation. This equation is

$$\frac{\partial p}{\partial x} = \frac{\beta}{2\rho_0 c_0^3}\frac{\partial p^2}{\partial \tau} \tag{3.18}$$

which is Eq. (3.14) without the dissipation term. Losses are ignored here simply for clarity. Moreover, since the loss term is linear its contribution to the evolution equations is trivial to include, as shown below in the present section. Also for clarity in subsequent equations, we combined the constants on the right-hand side as

$$\eta = \frac{\beta}{2\rho_0 c_0^3} \tag{3.19}$$

such that Eq. (3.18) becomes

$$\frac{\partial p}{\partial x} = \eta\frac{\partial p^2}{\partial \tau} \tag{3.20}$$

We begin by deriving the evolution equation for the autocorrelation function, which is the expected value of the product of the acoustic pressure in a waveform at two different instants in time [recall the first of Eqs. (2.2)]. Thus let p_0 and p_1 be an acoustic pressure waveform at a given location and a delayed replica of the same waveform at the same location, respectively, such

that

$$p_0 = p(x,\tau) \qquad p_1 = p(x,\tau+\psi) \tag{3.21}$$

where ψ is time delay. Since ψ is arbitrary, each of these pressures obeys Eq. (3.20) such that

$$\frac{\partial p_0}{\partial x} = \eta \frac{\partial p_0^2}{\partial \tau} \qquad \frac{\partial p_1}{\partial x} = \eta \frac{\partial p_1^2}{\partial \tau} \tag{3.22}$$

Now multiply each of Eqs. (3.22) by the pressure in the other to obtain

$$p_1 \frac{\partial p_0}{\partial x} = \eta p_1 \frac{\partial p_0^2}{\partial \tau} \qquad p_0 \frac{\partial p_1}{\partial x} = \eta p_0 \frac{\partial p_1^2}{\partial \tau} \tag{3.23}$$

the sum of which may be expressed as

$$\frac{\partial (p_0 p_1)}{\partial x} = \eta \left(p_0 \frac{\partial p_1^2}{\partial \tau} + \frac{\partial p_0^2}{\partial \tau} p_1 \right) \tag{3.24}$$

The expected value of $p_0 p_1$ is the autocorrelation function for p as defined in Eq. (2.2) if we assume that p_0 and p_1 have zero mean. Taking the expectation of both sides of Eq. (3.24) thus yields

$$\frac{\partial R_{pp}}{\partial x} = \eta \left(E\left[p_0 \frac{\partial p_1^2}{\partial \tau} \right] + E\left[\frac{\partial p_0^2}{\partial \tau} p_1 \right] \right) \tag{3.25}$$

The rate of change, or evolution, of the first-order statistical function R_{pp}, which depends quadratically on the acoustic pressure, is thus determined by the sum of two statistical functions that depend cubically on the pressure. The latter can be expressed in terms of the second-order covariance functions defined in Eqs. (2.5).

In order to manipulate the right-hand side of Eq. (3.25), we begin by looking at general properties of the expectation $E\left[x(\partial y/\partial\tau)\right]$, where either $x(\tau)$ or $y(\tau)$ may be delayed by time ψ with respect to the other. The variables x and y will represent either p_0 and p_1^2, respectively, as in the first expected value in Eq. (3.25), or p_1 and p_0^2 as in the second expectation. Using the fundamental definition of a derivative, we can rewrite $E\left[x(\partial y/\partial\tau)\right]$ as follows:

$$\begin{aligned} E\left[x(\tau)\frac{dy(\tau+\psi)}{d\tau}\right] &= E\left[x(\tau)\lim_{\epsilon\to 0}\frac{y(\tau+\psi+\epsilon)-y(\tau+\psi)}{\epsilon}\right] \\ &= \lim_{\epsilon\to 0}\frac{R_{xy}(\psi+\epsilon)-R_{xy}(\psi)}{\epsilon} \\ &= \frac{d}{d\psi}R_{xy}(\psi) \end{aligned} \tag{3.26}$$

If we reverse the positions of x and y and perform a similar set of operations, we see that a negative sign appears due to the difference in which term has the time delay:

$$\begin{aligned} E\left[\frac{dx(\tau)}{d\tau}y(\tau+\psi)\right] &= E\left[\lim_{\epsilon\to 0}\frac{x(\tau+\epsilon)-x(\tau)}{\epsilon}y(\tau+\psi)\right] \\ &= \lim_{\epsilon\to 0}\frac{R_{xy}(\psi-\epsilon)-R_{xy}(\psi)}{\epsilon} \\ &= -\frac{d}{d\psi}R_{xy}(\psi) \end{aligned} \tag{3.27}$$

Applying Eqs. (3.26) and (3.27) to the expected values in Eq. (3.25) yields

$$E\left[p_0\frac{\partial p_1^2}{\partial\tau}\right] = \frac{\partial}{\partial\psi}R_{pp^2}(\psi) \qquad E\left[\frac{\partial p_0^2}{\partial\tau}p_1\right] = -\frac{\partial}{\partial\psi}R_{p^2p}(\psi) \tag{3.28}$$

Now we can write Eq. (3.25) entirely in terms of correlation functions:

$$\frac{\partial R_{pp}(\psi)}{\partial x} = \eta\frac{\partial}{\partial\psi}\left[R_{pp^2}(\psi)-R_{p^2p}(\psi)\right] \tag{3.29}$$

Since, as is easily shown, $R_{xy}(\psi) = R_{yx}(-\psi)$, Eq. (3.29) can be rewritten as

$$\frac{\partial R_{pp}(\psi)}{\partial x} = \eta \frac{\partial}{\partial \psi} \left[R_{pp^2}(\psi) - R_{pp^2}(-\psi) \right] \tag{3.30}$$

which is in the form of the result obtained by Menounou and Blackstock [33].

The corresponding evolution equations for the power spectral density are obtained by taking a Fourier transform according to Eqs. (2.3). From Eq. (3.29) one thus obtains

$$\frac{\partial S_{pp}(\omega)}{\partial x} = j\omega\eta \left[S_{pp^2}(\omega) - S_{p^2p}(\omega) \right] \tag{3.31}$$

Equation (3.31) shows that the rate at which the power spectral density S_{pp} changes with distance depends on the higher-order cross spectral densities S_{pp^2} and S_{p^2p}.

Similarly, the Fourier transform of Eq. (3.30) yields

$$\frac{\partial S_{pp}(\omega)}{\partial x} = j\omega\eta \left[S_{pp^2}(\omega) - S_{pp^2}(-\omega) \right] \tag{3.32}$$

Because R_{pp^2} is a real function, its Fourier transform exhibits the property $S_{pp^2}(-\omega) = S^*_{pp^2}(\omega)$, and since for any complex number $z - z^* = j2\Im(z)$, Eq. (3.32) can be rewritten in the form

$$\frac{\partial S_{pp}(\omega)}{\partial x} = -2\eta\omega\Im \left\{ S_{pp^2}(\omega) \right\} \tag{3.33}$$

Alternatively, since $S_{xy}(\omega) = S_{yx}(-\omega)$, Eq. (3.32) also takes the form

$$\frac{\partial S_{pp}(\omega)}{\partial x} = 2\eta\omega\Im \left\{ S_{p^2p}(\omega) \right\} \tag{3.34}$$

This last form, Eq. (3.34), has been written by Morfey and Howell [1] as

$$\frac{\partial S_{pp}}{\partial x} = 2\omega\eta Q_{p^2p} \tag{3.35}$$

where

$$Q_{p^2p} = \Im(S_{p^2p}) \tag{3.36}$$

Morfey and Howell [1] refer to Q_{p^2p} as a spectral transfer term, and Falco [2] refers to Q_{p^2p} as the quad-spectral density. However, Eq. (3.35) differs from the evolution equation used by Falco, who has a minus sign on the right-hand side. We suggest that a sign error may have been made in the relation $S_{p^2p} = \Re(S_{p^2p}) - j\Im(S_{p^2p})$, in which a plus sign may have been used in place of the minus sign. It should be noted that this discrepancy with Eq. (3.35) does not affect any of Falco's conclusions.

It was noted above that it is straightforward to include the losses taken into account by the second term in Eq. (3.14). Proceeding as before, and following steps as in Eqs. (3.26) and (3.27) to show that

$$E\left[x(\tau)\frac{d^2y(\tau+\psi)}{d\tau^2}\right] = E\left[\frac{d^2x(\tau)}{d\tau^2}y(\tau+\psi)\right] = \frac{d^2}{d\psi^2}R_{xy}(\psi) \tag{3.37}$$

one obtains for the evolution of the autocorrelation function $R_{pp}(x,\psi)$, in place of Eq. (3.29),

$$\frac{\partial R_{pp}}{\partial x} = \frac{\beta}{2\rho_0 c_0^3}\left(\frac{\partial R_{pp^2}}{\partial \psi} - \frac{\partial R_{p^2p}}{\partial \psi}\right) + \frac{\delta}{c_0^3}\frac{\partial^2 R_{pp}}{\partial \psi^2} \tag{3.38}$$

where the definition of η in Eq. (3.19) has been reinstated. In place of Eq. (3.31) one likewise obtains for the evolution of the power spectral den-

sity $S_{pp}(x,\omega)$

$$\frac{\partial S_{pp}}{\partial x} = \frac{j\omega\beta}{2\rho_0 c_0^3}\left(S_{pp^2} - S_{p^2p}\right) - 2\alpha S_{pp} \tag{3.39}$$

where $\alpha = \delta\omega^2/2c_0^3$ is again the linear thermoviscous attenuation coefficient for the sound pressure at angular frequency ω. The solution of Eq. (3.39) when acoustic nonlinearity is disregarded is thus $S_{pp}(x,\omega) = S_{pp}(0,\omega)e^{-2\alpha x}$, as expected, such that changes in the power spectral density are due only to the dependence of the attenuation coefficient on frequency, and the power spectrum is thus low-pass filtered.

Finally, the rate of change with distance of the (first-order) power spectral density due to nonlinearity can be expressed in terms of the (second-order) bispectrum. This formulation was introduced in the work of Gurbatov et al. [34]. Making use of Eqs. (2.5), we begin by writing

$$R_{pp^2}(\psi) = E[p(\tau)p^2(\tau+\psi)] = R_{ppp}(\psi,\psi) \tag{3.40}$$

$$R_{p^2p}(\psi) = E[p^2(\tau)p(\tau+\psi)] = R_{ppp}(0,\psi) = R_{ppp}(\psi,0) \tag{3.41}$$

The next step is to take the Fourier transform of Eq. (3.29), beginning with the Fourier transform of R_{pp^2} on the right-hand side:

$$S_{pp^2}(\omega) = \int_{-\infty}^{\infty} R_{pp^2}(\psi)e^{-j\omega\psi}\,d\psi \tag{3.42}$$

Now express $R_{ppp}(\psi)$ in terms of its spectral density $S_{ppp}(\omega)$ by means of its inverse Fourier transform:

$$R_{ppp}(\psi_1,\psi_2) = \frac{1}{(2\pi)^2}\iint_{-\infty}^{\infty} S_{ppp}(\omega_1,\omega_2)e^{j\omega_1\psi_1 + j\omega_2\psi_2}\,d\omega_1 d\omega_2 \tag{3.43}$$

From Eq. (3.40) we thus have

$$R_{pp^2}(\psi) = \frac{1}{(2\pi)^2} \iint_{-\infty}^{\infty} S_{ppp}(\omega_1, \omega_2) e^{j(\omega_1+\omega_2)\psi} \, d\omega_1 d\omega_2 \tag{3.44}$$

the substitution of which into Eq. (3.42) yields

$$S_{pp^2}(\omega) = \frac{1}{(2\pi)^2} \iiint_{-\infty}^{\infty} S_{ppp}(\omega_1, \omega_2) e^{j(\omega_1+\omega_2-\omega)\psi} \, d\omega_1 d\omega_2 d\psi \tag{3.45}$$

Integrating first over ψ, we arrive at

$$\begin{aligned} S_{pp^2}(\omega) &= \frac{1}{(2\pi)^2} \iint_{-\infty}^{\infty} S_{ppp}(\omega_1, \omega_2) \delta(\omega_1 + \omega_2 - \omega) \, d\omega_1 d\omega_2 \\ &= \frac{1}{(2\pi)^2} \int_{-\infty}^{\infty} S_{ppp}(\omega_1, \omega - \omega_1) \, d\omega_1 \end{aligned} \tag{3.46}$$

where δ is the Dirac delta function.

It remains to address the second term on the right-hand side of Eq. (3.29). Proceeding in the same fashion we begin by writing

$$S_{p^2p}(\omega) = \int_{-\infty}^{\infty} R_{p^2p}(\psi) e^{-j\omega\psi} \, d\psi \tag{3.47}$$

Next, from Eqs. (3.41) and (3.43) we have

$$R_{p^2p}(\psi) = \frac{1}{(2\pi)^2} \iint_{-\infty}^{\infty} S_{ppp}(\omega_1, \omega_2) e^{j\omega_2\psi} \, d\omega_1 d\omega_2 \tag{3.48}$$

Now substitute Eq. (3.48) in Eq. (3.47) to obtain

$$\begin{aligned} S_{p^2p}(\omega) &= \frac{1}{(2\pi)^2} \iiint_{-\infty}^{\infty} S_{ppp}(\omega_1, \omega_2) e^{j(\omega_2-\omega)\psi} \, d\omega_1 d\omega_2 d\psi \\ &= \frac{1}{(2\pi)^2} \iint_{-\infty}^{\infty} S_{ppp}(\omega_1, \omega_2) \delta(\omega_2 - \omega) \, d\omega_1 d\omega_2 \\ &= \frac{1}{(2\pi)^2} \int_{-\infty}^{\infty} S_{ppp}(\omega_1, \omega) \, d\omega_1 \end{aligned} \tag{3.49}$$

Finally, from Eqs. (3.29), (3.46), and (3.49), we have

$$\frac{\partial S_{pp}(\omega)}{\partial x} = \frac{j\omega\eta}{4\pi^2}\int_{-\infty}^{\infty}\left[S_{ppp}(\omega-\Omega,\Omega) - S_{ppp}(\omega,\Omega)\right]d\Omega \tag{3.50}$$

which is the result presented by Gurbatov et al. [34]. The value of Eq. (3.50) is that we now have a description of spectral energy transfer in terms of the bispectrum.

The intergral over $S_{ppp}(\omega_1,\omega_2) = S_{ppp}(\omega-\Omega,\Omega)$ accounts for all resonant sum and difference frequency interactions contributing to the growth or decay of the power spectral density at frequency ω because $\omega_1+\omega_2=\omega$, and all values of both ω_1 and ω_2, both positive and negative, contribute to the integral. Precisely this sort of intergral, but over the product of the acoustic pressure at frequencies $\omega-\Omega$ and ω, determines the growth or decay of the acoustic pressure at frequency ω. However, unlike the evolution equation for the acoustic pressure at frequency ω, Eq. (3.50) contains a second, different type of integral, this one with $S_{ppp}(\omega_1,\omega_2) = S_{ppp}(\omega,\Omega)$ for its integrand. In this case $\omega_1=\omega$ and $\omega_2=\Omega$, which indicates that the growth or decay of the power spectral density at frequency ω is also directly affected by resonant nonlinear spectral interactions between the frequency ω itself and all other frequencies in the spectrum, the sum or difference frequencies of which cannot equal ω for nonzero Ω.

A visual representation of the integration contours is provided in Fig. 3.2 for (dimensionless) angular frequency $\omega/\omega_0=4$ in the power spectral density. The coordinates $(\omega-\Omega,\Omega)$ correspond to integration along a negative-slope

line with an intercept of $\omega_1/\omega_0 = 4$ on the horizontal axis and an intercept of $\omega_2/\omega_0 = 4$ on the vertical axis. The coordinates (ω, Ω) correspond to integration along a vertical line with an intercept of $\omega_1/\omega_0 = 4$ on the horizontal axis. The dots signify all resonant nonlinear interactions for a single-frequency source radiating at frequency $\omega/\omega_0 = 1$, the field of which is described by the Fourier series in Eq. (3.10).

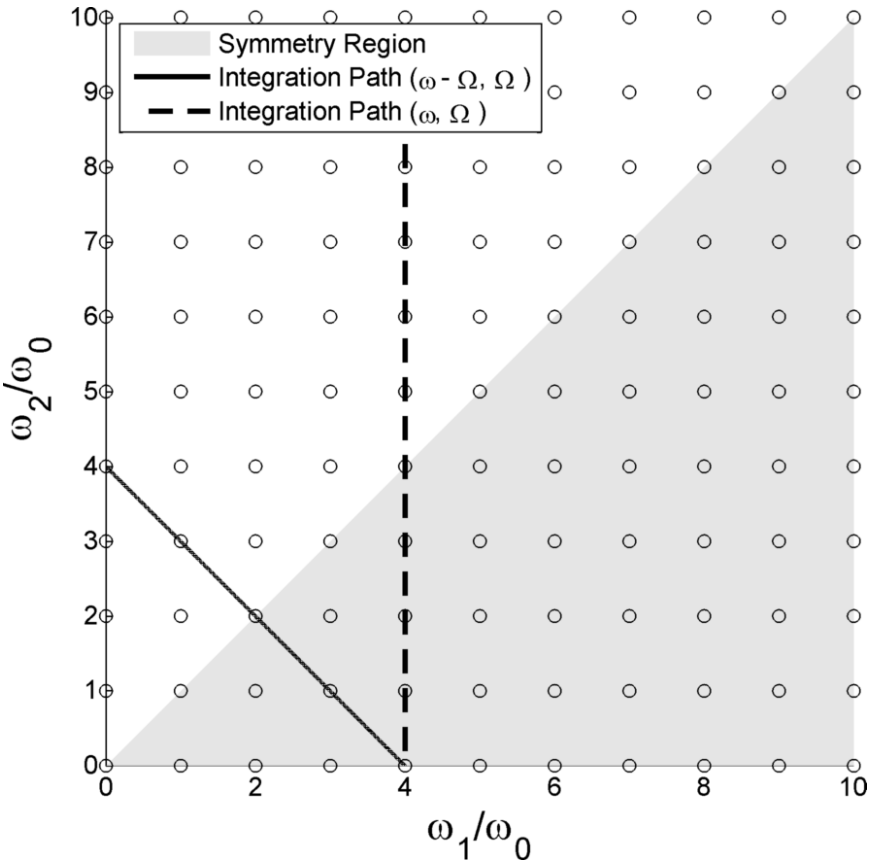

Figure 3.2: A depiction of integration paths for Eq. (3.50) on bispectral axes for $\omega/\omega_0 = 4$. Dots show resonant interactions for a single-frequency source radiating at ω_0.

3.3 Evolution Equation for the Bispectrum

We now proceed to develop an evolution equation similar to Eq. (3.31) but for the bispectrum. In place of Eqs. (3.21) we now require pressures at three different instants in time:

$$p_0 = p(x, \tau) \qquad p_1 = p(x, \tau + \psi_1) \qquad p_2 = p(x, \tau + \psi_2) \tag{3.51}$$

Instead of the two Eqs. (3.23) we have three, which when added together give

$$\frac{\partial(p_0 p_1 p_2)}{\partial x} = \eta \left(p_0 p_1 \frac{\partial p_2^2}{\partial \tau} + p_0 \frac{\partial p_1^2}{\partial \tau} p_2 + \frac{\partial p_0^2}{\partial \tau} p_1 p_2 \right) \tag{3.52}$$

According to the definition of triple correlation given in Eq. (2.5), after taking the expected value of Eq. (3.52) we have

$$\frac{\partial R_{ppp}}{\partial x} = \eta \left(E \left[p_0 p_1 \frac{\partial p_2^2}{\partial \tau} + p_0 \frac{\partial p_1^2}{\partial \tau} p_2 + \frac{\partial p_0^2}{\partial \tau} p_1 p_2 \right] \right) \tag{3.53}$$

Following the general procedure in Eqs. (3.26) and (3.27), we now examine the structure of the individual terms in Eq. (3.53) using independent random variables x, y, and z. With the limit definition of a derivative taken into account, the generic form of the first term on the right-hand side of Eq. (3.53) becomes

$$\begin{aligned} E \left[x(\tau) y(\tau + \psi_y) \frac{dz(\tau + \psi_z)}{d\tau} \right] & \\ &= E \left[x(\tau) y(\tau + \psi_y) \lim_{\epsilon \to 0} \frac{z(\tau + \psi_z + \epsilon) - z(\tau + \psi_z)}{\epsilon} \right] \\ &= \lim_{\epsilon \to 0} \frac{R_{xyz}(\psi_y, \psi_z + \epsilon) - R_{xyz}(\psi_y, \psi_z)}{\epsilon} \\ &= \frac{d}{d\psi_z} R_{xyz}(\psi_y, \psi_z) \end{aligned} \tag{3.54}$$

Simply interchanging the symbols y and z yields

$$E\left[x(\tau)\frac{dy(\tau+\psi_y)}{d\tau}z(\tau+\psi_z)\right] = \frac{d}{d\psi_y}R_{xyz}(\psi_y,\psi_z) \tag{3.55}$$

The last term of Eq. (3.53) involves the derivative of the non-delayed signal, and it becomes

$$\begin{aligned} E\left[\frac{dx(\tau)}{d\tau}y(\tau+\psi_y)z(\tau+\psi_z)\right] &= E\left[\lim_{\epsilon\to 0}\frac{x(\tau+\epsilon)-x(\tau)}{\epsilon}y(\tau+\psi_y)z(\tau+\psi_z)\right] \\ &= \lim_{\epsilon\to 0}\frac{R_{xyz}(\psi_y-\epsilon,\psi_z-\epsilon)-R_{xyz}(\psi_y,\psi_z)}{\epsilon} \\ &= -\left(\frac{\partial}{\partial\psi_y}+\frac{\partial}{\partial\psi_z}\right)R_{xyz}(\psi_y,\psi_z) \end{aligned} \tag{3.56}$$

The expected values of the terms on the right-hand side of Eq. (3.53) become

$$\begin{aligned} E\left[p_0 p_1\frac{\partial p_2^2}{\partial\tau}\right] &= \frac{\partial R_{ppp^2}}{\partial\psi_2} \\ E\left[p_0\frac{\partial p_1^2}{\partial\tau}p_2\right] &= \frac{\partial R_{pp^2p}}{\partial\psi_1} \\ E\left[\frac{\partial p_0^2}{\partial\tau}p_1 p_2\right] &= -\frac{\partial R_{p^2pp}}{\partial\psi_1}-\frac{\partial R_{p^2pp}}{\partial\psi_2} \end{aligned} \tag{3.57}$$

and thus

$$\frac{\partial R_{ppp}}{\partial x} = \eta\left[\frac{\partial}{\partial\psi_1}(R_{pp^2p}-R_{p^2pp})+\frac{\partial}{\partial\psi_2}(R_{ppp^2}-R_{p^2pp})\right] \tag{3.58}$$

Then, if we take the two-dimensional Fourier transform as defined in Eq. (2.6), we arrive at

$$\begin{aligned} \frac{\partial S_{ppp}(\omega_1,\omega_2)}{\partial x} &= j\omega_1\eta S_{pp^2p}(\omega_1,\omega_2)+j\omega_2\eta S_{ppp^2}(\omega_1,\omega_2) \\ &\quad -j(\omega_1+\omega_2)\eta S_{p^2pp}(\omega_1,\omega_2) \end{aligned} \tag{3.59}$$

This final result shows how the bispectrum changes over distance according to spectra at fourth order. However, because of the squared terms, the derivative of the bispectrum can be calculated with spectra at third order with p^2 substituted as one of the signals. This calculation will be further explored in Chap. 4.

3.4 Application to Radiation from a Sinusoidal Source

Although many waveforms are difficult to predict when they propagate nonlinearly, sinusoids have been studied extensively and analytical solutions exist for both pre- and post-shock distances [28, 30, 31]. Here, we use known solutions for the nonlinear propagation of a sinusoid to observe the behavior of Q_{p^2p} at small distances from the source. We use this small-distance assumption to provide a tractable comparison between analysis and computation.

Let us begin with a time-harmonic waveform expressed as a summation of its harmonics,

$$p = \frac{1}{2} \sum_{n=-\infty}^{\infty} p_n e^{jn\omega_0\tau} \tag{3.60}$$

where

$$p_n = \frac{1}{\pi} \int_{-\pi}^{\pi} p(\omega_0\tau) e^{-jn\omega_0\tau} \, d(\omega_0\tau) \tag{3.61}$$

is the n^{th} harmonic, found by taking the Fourier transform of pressure in non-dimensional coordinates $\omega_0\tau$. Let q represent the squared waveform, such that

$$q = p^2 = \frac{1}{2} \sum_{n=-\infty}^{\infty} q_n e^{jn\omega_0\tau} \tag{3.62}$$

In order to find q_n in terms of p_n, we now write q as the square of the right-hand side of Eq. (3.60):

$$q = \frac{1}{4} \sum_{\ell=-\infty}^{\infty} \sum_{m=-\infty}^{\infty} p_\ell p_m e^{j(\ell+m)\omega_0 \tau} \tag{3.63}$$

and replace $\ell + m$ with n such that

$$q = \frac{1}{2} \sum_{n=-\infty}^{\infty} \left(\frac{1}{2} \sum_{m=-\infty}^{\infty} p_m p_{n-m} \right) e^{jn\omega_0 \tau} \tag{3.64}$$

By inspection, q_n is then

$$q_n = \frac{1}{2} \sum_{m=-\infty}^{\infty} p_m p_{n-m} \tag{3.65}$$

or, written exclusively with positive m,

$$q_n = \frac{1}{2} \sum_{m=1}^{n-1} p_m p_{n-m} + \sum_{m=n+1}^{\infty} p_m p_{m-n}^* \tag{3.66}$$

making use of the relation $p_{-n} = p_n^*$, and assuming no static pressure component at $m = 0$.

We now connect these harmonic formulas to spectral densities. Power spectral density is obtained from the product of pressure components as

$$S_{pp,n} = p_n^* p_n = |p_n|^2 \tag{3.67}$$

and the cross-spectral densities of pressure with its square are written as

$$S_{p^2 p,n} = q_n^* p_n \tag{3.68}$$

and

$$S_{p p^2,n} = p_n^* q_n \tag{3.69}$$

Recall from Eq. (3.35) that the change in power spectral density can be described with S_{p^2p}. If we apply that information to the present harmonic representation, we find that

$$\begin{aligned}\frac{\partial |p_n|^2}{\partial x} &= 2\eta n\omega_0 \Im\{S_{p^2p,n}\} \\ &= 2\eta n\omega_0 \Im\{S^*_{pp^2,n}\} \\ &= -2\eta n\omega_0 \Im\{S_{pp^2,n}\} \\ &= -2\eta n\omega_0 \Im\{p_n^* q_n\} \end{aligned} \tag{3.70}$$

Let the intensity of the n^{th} harmonic be written as

$$I_n = \frac{|p_n|^2}{2\rho_0 c_0} \tag{3.71}$$

and thus the change in power spectral density and change in intensity can be related to one another:

$$\frac{\partial |p_n|^2}{\partial x} = 2\rho_0 c_0 \frac{\partial I_n}{\partial x} \tag{3.72}$$

Solving for the change in intensity with the inclusion of Eq. (3.70), we find

$$\frac{\partial I_n}{\partial x} = -\frac{\eta\omega_0}{\rho_0 c_0} n \Im\{p_n^* q_n\} \tag{3.73}$$

We then replace η and q_n with known values and arrive at

$$\frac{\partial I_n}{\partial x} = -\frac{\beta\omega_0}{4\rho_0^2 c_0^4} n \Im\left\{p_n^* \sum_{m=-\infty}^{\infty} p_m p_{n-m}\right\} \tag{3.74}$$

For odd waveforms, such as the Fubini solution, let pressure be given

as a Fourier sine series such that

$$\begin{aligned} p &= \sum_{n=1}^{\infty} b_n \sin n\omega_0\tau \\ &= \frac{1}{2j}\sum_{n=1}^{\infty} b_n \left(e^{jn\omega_0\tau} - e^{-jn\omega_0\tau}\right) \\ &= \frac{1}{2j}\sum_{n=-\infty}^{\infty} b_n e^{jn\omega_0\tau} \\ &= \frac{1}{2}\sum_{n=-\infty}^{\infty} p_n e^{jn\omega_0\tau} \end{aligned} \tag{3.75}$$

where b_n is the n^{th} harmonic coefficient. By inspection, we see from Eq. (3.75) that

$$p_n = -jb_n \tag{3.76}$$

This formula can be applied to Eq. (3.74) such that the contents of the $\Im\{\cdot\}$ operator become

$$\begin{aligned} p_n^* \sum_{m=-\infty}^{\infty} p_m p_{n-m} &= (jb_n) \sum_{m=-\infty}^{\infty} (-jb_m)(-jb_{n-m}) \\ &= -jb_n \sum_{m=-\infty}^{\infty} b_m b_{n-m} \end{aligned} \tag{3.77}$$

and Eq. (3.74) becomes

$$\frac{\partial I_n}{\partial x} = \frac{\beta\omega_0}{4\rho_0^2 c_0^4} n b_n \sum_{m=-\infty}^{\infty} b_m b_{n-m} \tag{3.78}$$

We thus arrive at a formula for change in intensity that is consistent with Fenlon [35].

We now proceed to express the quad-spectral density in a form similar to Eq. (3.78) based on the Fourier sine series in Eq. (3.75). This will permit

us to derive a perturbation solution that can be used to check our numerical computations. Beginning with Eqs. (3.36), (3.65), (3.68), and (3.76) we write for the n^{th} harmonic component of the quad-spectral density

$$\begin{aligned} Q_{p^2p,n} &= \Im\{S_{p^2p,n}\} \\ &= \Im\{p_n q_n^*\} \\ &= \frac{1}{2}\Im\left\{p_n \sum_{m=-\infty}^{\infty} p_m^* p_{n-m}^*\right\} \\ &= \frac{1}{2}\Im\left\{jb_n \sum_{m=-\infty}^{\infty} b_m b_{n-m}\right\} \end{aligned} \tag{3.79}$$

and thus

$$Q_{p^2p,n} = \frac{1}{2} b_n \sum_{m=-\infty}^{\infty} b_m b_{n-m} \tag{3.80}$$

We now introduce the dimensionless spectral amplitude

$$B_n = \frac{b_n}{p_0} \tag{3.81}$$

such that the dimensionless form of the quad-spectral density becomes, designated by a prime,

$$Q'_{p^2p,n} = \frac{1}{2} B_n \sum_{m=-\infty}^{\infty} B_m B_{n-m} \tag{3.82}$$

With Eq. (3.82) rewritten to use only positive m, it becomes

$$Q'_{p^2p,n} = \frac{B_n}{2}\left(\sum_{m=1}^{n-1} B_m B_{n-m} - 2\sum_{m=n+1}^{\infty} B_m B_{m-n}\right) \tag{3.83}$$

The values of B_n can be found through perturbation methods, which

results in the following, to leading order [28]:

$$B_1 = 1 \tag{3.84a}$$

$$B_2 = \frac{1}{2}\sigma \tag{3.84b}$$

$$B_3 = \frac{3}{8}\sigma^2 \tag{3.84c}$$

Equations (3.84) follow directly from Taylor series expansion of the Fubini coefficients in Eq. (3.11). These values of B_n can then be used to find the leading order values of $Q'_{p^2p,n}$, which are

$$\begin{aligned} Q'_{p^2p,1} &= \frac{B_1}{2}\left(0 - 2\sum_{m=2}^{\infty} B_m B_{m-1}\right) \\ &= -B_1\left(B_2 B_1 + B_3 B_2 + \cdots\right) \\ &= -\frac{1}{2}\sigma + O(\sigma^3) \end{aligned} \tag{3.85}$$

$$\begin{aligned} Q'_{p^2p,2} &= \frac{B_2}{2}\left(B_1^2 - 2\sum_{m=3}^{\infty} B_m B_{m-2}\right) \\ &= \frac{1}{2}B_1^2 B_2 - B_2\left(B_3 B_1 + B_4 B_2 + \cdots\right) \\ &= \frac{1}{4}\sigma + O(\sigma^3) \end{aligned} \tag{3.86}$$

$$\begin{aligned} Q'_{p^2p,3} &= \frac{B_3}{2}\left(\sum_{m=1}^{2} B_m B_{3-m} - 2\sum_{m=4}^{\infty} B_m B_{m-3}\right) \\ &= B_1 B_2 B_3 - B_3\left(B_4 B_1 + \cdots\right) \\ &= \frac{3}{16}\sigma^3 + O(\sigma^5) \end{aligned} \tag{3.87}$$

We may now form the following ratios to leading order in σ (with the prime

on $Q_{p^2p,n}$ no longer needed):

$$\frac{Q_{p^2p,2}}{Q_{p^2p,1}} = -\frac{\sigma/4}{\sigma/2} = -\frac{1}{2} \tag{3.88}$$

$$\frac{Q_{p^2p,3}}{Q_{p^2p,1}} = -\frac{3\sigma^3/16}{\sigma/2} = -\frac{3}{8}\sigma^2 \tag{3.89}$$

Equations (3.88) and (3.89) provide a test of our numerical calculation of the quad-spectral density in Chap. 5 in the limit $\sigma \to 0$.

Equations (3.88) and (3.89) also lead to an observation that is consistent with established models of nonlinear wave propagation. We see that the term at the fundamental frequency ω is greater in magnitude and opposite in sign compared to the other terms, indicating that energy is leaving the fundamental and entering the higher harmonics. According to the Fubini solution for monofrequency sound waves in the pre-shock region as described by Blackstock, Hamilton, and Pierce [28] and shown plotted in Fig. 3.1, the fundamental shows a decrease in amplitude as its energy is shifted upward to the other harmonics. Equations (3.88) and (3.89) are thus consistent in this regard.

Chapter 4

Numerical Techniques

In this chapter, numerical techniques for simulating the propagation of finite-amplitude sound and calculating statistical properties according to formulas in Chap. 2 and 3 are presented.

4.1 Waveform Generation and Propagation

Nonlinear propagation of arbitrarily shaped waveforms is accomplished through the use of the BurgersTX code developed at the University of Texas at Austin [13, 14] with some adaptations for waveform generation and data output. The form of the BurgersTX code used in this thesis can be found at `http://people.bu.edu/robinc/kzk/burgers.html`. This computer code solves the Burgers equation, Eq. (3.14), in the time domain, which is convenient for modeling the nonlinear propagation of random waveforms.

The BurgersTX code enables waveform input in two different ways: importing a data file, or creating a sinusoidal waveform within a subroutine. In the version modified for this paper, internal generation was selected so that the program could be looped to propagate a series of waves without the necessity of calling other programs.

We require a series of independently generated waves rather than one long signal because of simulation considerations. Dividing a long signal into shorter records for analysis is appropriate for experimentally measured data because the source is constantly changing, though still ergodic. Each record taken from the continuous stream can be regarded as independent from the other records, and the bispectrum can then be used to highlight phase relationships over propagation distance. In simulation, taking small records from one long signal means that every record has identical frequency and phase information. These shared characteristics cause every record to be fully correlated to the others, and as a result, bispectral analysis provides no new insight into the propagation process.

In selecting waveforms to study, we begin with sinusoids. Waves radiated by monofrequency sources have been studied extensively in nonlinear acoustics, and analytic solutions for harmonic amplitudes are known, such as the curves shown in Fig. 3.1. These analytic results can be compared to observed amplitudes as a benchmark test of the propagation routine.

For the sinusoidal case, explicit analytic solutions are known for the harmonic amplitudes, as discussed in Sec. 3.1. Harmonic amplitudes were calculated through discrete Fourier transforms of the numerically propagated signals using BurgersTX at distances in increments of $\Delta\sigma = 0.1$ for $0 \leq \sigma \leq 1$ and for several integer values of σ at greater distances. As shown in Fig. 4.1, the calculated harmonics agree with the analytic solution given by Eq. (3.12). In the analytic model there is no absorption prior to shock formation, and after

shock formation all absorption is assumed to occur at the shocks and is taken into account by weak shock theory. In the code we used $\Gamma = 100$ for the value of the Gol'dberg number, which indicates very small but nonzero absorption, and enough to provide stability of the code following shock formation.

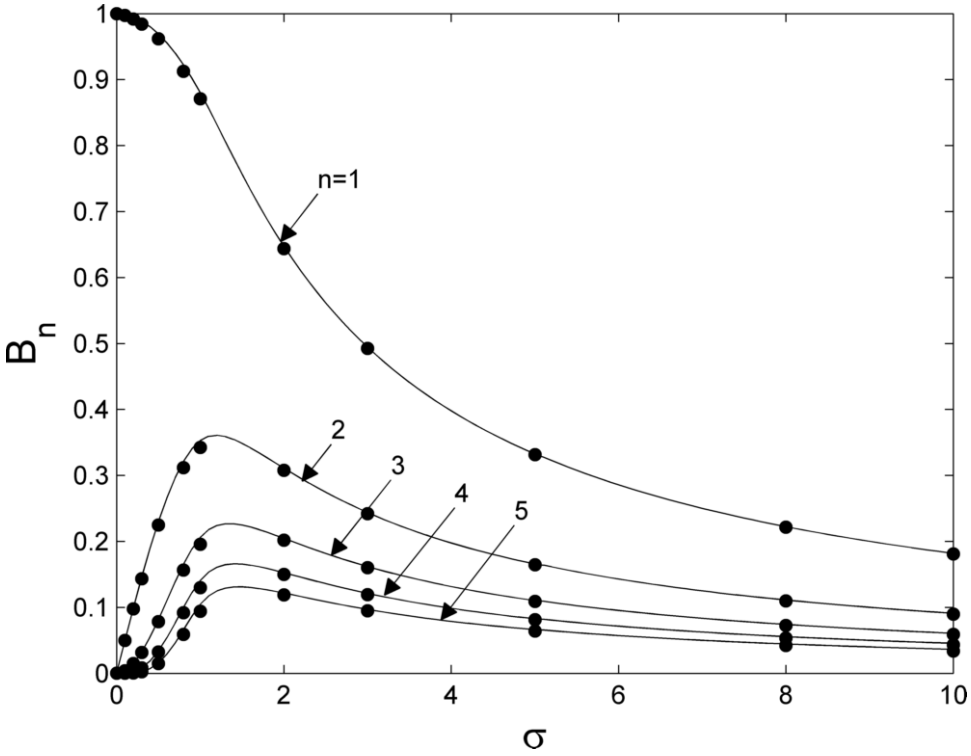

Figure 4.1: Comparison of analytic and numerical solutions for the harmonic amplitudes B_n in Eq. (3.12). Solid lines show the analytic values, found from the known solution as discussed in Sec. 3.1. Dots show the numerical values, found from discrete Fourier transforms of an initially sinusoidal waveform.

Propagated sinusoids were also used to calculate quad-spectral densities in increments of $\Delta\sigma = 0.01$ starting at the source. In Eq. (3.88) it was found that for $\sigma \ll 1$ the magnitude of $Q_{p^2p,2}$ for the second harmonic is half the

magnitude of $Q_{p^2p,1}$ for the fundamental. This behavior is revealed by the numerical result for the magnitude of $Q_{p^2p,2}/Q_{p^2p,1}$ calculated numerically and presented in Fig. 4.2(a). It was also found in Eq. (3.87) that the magnitude of $Q_{p^2p,3}$ for the third harmonic grows cubically with σ close to the source, and therefore its ratio to the magnitude of $Q_{p^2p,1}$ for the fundamental, which grows linearly with σ close to the source, is shown in Eq. (3.89) to be quadratic in σ. The quadratic dependence on σ of the magnitude of the ratio $Q_{p^2p,3}/Q_{p^2p,1}$ is displayed by the numerical results presented in Fig. 4.2(b). Although not plotted in Fig. 4.2(b), the relative rate of growth predicted by Eq. (3.89), $\frac{3}{8}\sigma^2$, exceeds the relative rate of growth in Fig. 4.2(b) that was obtained numerically by approximately a factor of 2, i.e., the latter is closer to $\frac{3}{16}\sigma^2$. The source of this discrepancy is unknown at this time.

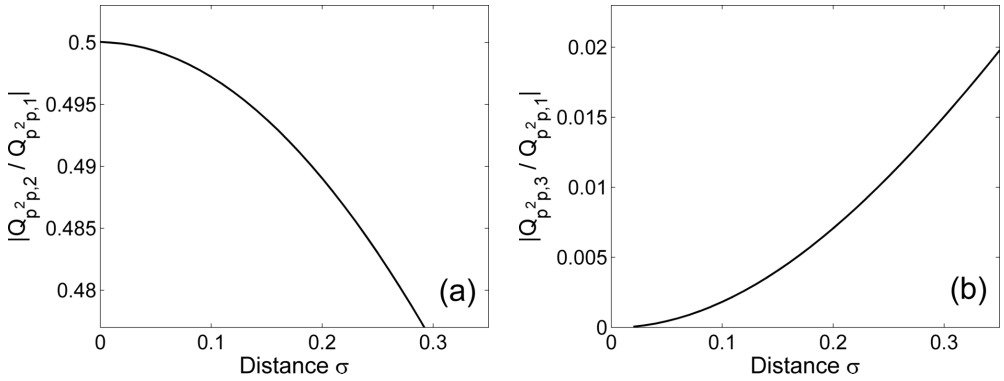

Figure 4.2: Numerically calculated quad-spectral densities close to the source for (a) the second harmonic and (b) the third harmonic, normalized by the quad-spectral density for the source frequency. These values were calculated from numerical simulations of waves propagated away from a sinusoidal source.

After monofrequency waves, bifrequency waves are propagated and analyzed, followed by bandlimited Gaussian white noise. For sinusoids, the single

frequency present in the initial waveform is used as the center frequency f_0. For all other signals, the center frequency is chosen as the mean of the nominal upper and lower frequencies defining the frequency range before propagation.

For each type of waveform, one hundred records are generated, propagated, and analyzed. This number was chosen in order to reduce statistical error and thus reach reasonable levels of statistical significance as measured by Elgar and Guza [36]. For testing purposes, calculations of the bicoherence and skewness function have also been made with fifty records, and no qualitative difference has been observed apart from a slight decrease in overall amplitude. No change has been observed in the main features of these functions.

Individual record length was chosen according to resolution requirements in the time and frequency domains. To accurately model shocks in the waveform, it is necessary to use a sufficiently high temporal resolution. The faster the rise time of a shock, the greater is the density of points required for adequate resolution of the wave profile in this region. For plane waves, shock rise time is inversely proportional to the Gol'dberg number Γ, defined in Eq. (3.17). The Gol'dberg number can be considered as a ratio of the effects of nonlinearity to the effects of dissipation. Nonlinearity will cause a waveform to steepen, whereas dissipation will cause a waveform to smooth out. For $\Gamma \gg 1$, the effects of nonlinearity are initially much greater than the effects of dissipation, and the waveform will steepen relatively quickly and ultimately form shocks. The Burgers equation, presented as Eq. (3.14), includes

the Gol'dberg number when written in dimensionless form,

$$\frac{\partial P}{\partial \sigma} - \frac{1}{\Gamma}\frac{\partial^2 P}{\partial \theta^2} = P\frac{\partial P}{\partial \theta} \tag{4.1}$$

where $P = p/p_0$ is dimensionless pressure and $\theta = \omega_0 \tau$ is dimensionless time. The Gol'dberg number, then, has a strong influence on the propagated waveform solution.

For the Gol'dberg number considered in our simulations, $\Gamma = 100$, and for the bandwidths of the source waveforms considered (up to 100%), 400 points per cycle at the center frequency of the source bandwidth were found to be sufficient to adequately resolve the shocks for our purposes.

In the figures of Chap. 5, portions of sample waveforms are plotted to show that all shocks were adequately resolved. The number of cycles per record was chosen such that the resolution in the frequency domain would be appropriate for visual interpretation of the data. Increasing record length in the time domain decreases the width of frequency bins in a discrete Fourier transform. Frequency bins that are too small would cause narrow peaks on the bispectral axes to be difficult to see, but frequency bins that are too large would cause details in the structure of the bispectrum to be obscured. A value of 100 cycles per record was found to be appropriate for these criteria. As a result, all analyzed data records are 40,000 points in length, and the Nyquist frequency is 50 times the center frequency.

Before each simulation, the records are padded with additional waveform cycles so that effects at the edges of the waveform do not influence the

data of interest. Each record is also padded with several cycles' worth of zeros so that the signal has space to expand within the BurgersTX program. This "expansion" is a consequence of a pulse becoming longer in duration as it propagates primarily as a result of absorption, which acts as a low-pass filter.

Zero padding requires special consideration when generating waveforms with specific spectral characteristics. Multifrequency signals are generated by summations of sinusoids, and the use of arbitrary frequency spacing would result in power spectral densities with spectral leakage. This spectral leakage can be avoided, however, by choosing a frequency spacing equivalent to the locations of frequency bins of the discrete Fourier transform. For this reason, the frequency bins were chosen according to the analysis length (40,000 points) as opposed to the full length of the padded signal. With a rectangular window, this frequency distribution would result in flat spectra for bandlimited noise. This behavior is not observed in this thesis, though, due to the application of a Hamming window on the waveform, as recommended for bispectral analysis by Nikias and Petropulu [16].

For every record, a random phase is applied to every frequency component via a pseudorandom number generator with uniform distribution. This process ensures that the bispectrum shows relative phase interactions and not just artifacts of shared absolute phase in the initial records.

Waves having initially only one frequency have a predictable amplitude regardless of phase randomization, but when multiple frequencies are present in the initial signal the peak amplitude may vary considerably. To make fair

comparisons between mono- and multi-frequency signals, it is therefore appropriate to normalize by signal energy rather than by peak signal amplitude. To this end, every initial record is scaled to have the same root-mean-square (RMS) amplitude. In accordance of the normalization used in Sec. 3.1, the energy is set equivalent to that of a sinusoidal source waveform which, when propagated without absorption, forms a shock at $\sigma = 1$.

For each waveform generated with the modified BurgersTX code, output is produced at a series of different distances and saved to individual text files. These records are later used to calculate spectra according to the process described in Sec. 4.2.

4.2 Statistical Analysis

Statistical analysis of the propagated waveforms is conducted in Matlab through a procedure very similar to that described by Kim and Powers [23] but expanded to include multiple formulas for the multiple statistics of interest, such as the skewness function.

The general computation method is as follows:

1. Choose an appropriate noise level and apply this noise to a copy of the record to be used for the normalized spectra.[1] The original record

[1]Step 1 is not generally necessary for computations of spectra, and it is not used here for any of the spectra that are not normalized. However, this step is required for the normalized bispectra (bicoherence and skewness function), at least for waveforms that have been generated numerically. Because the normalizations have power spectra in the denominator,

without noise should be retained for the non-normalized spectra.

2. Subtract the mean from record, thus permitting the equivalence of the covariance and correlation functions as discussed in Sec. 2.1.

3. Apply a data window to record. A Hamming window was selected, as is consistent with Nikias and Petropulu [16] and Gee et al. 2005 [4].

4. Compute Fourier amplitudes according to Eq. (2.18), repeated here for convenience:

$$X_k(m) = \frac{1}{N} \sum_{n=1}^{N} x_k(n) e^{-i2\pi mn/N} \tag{4.2}$$

where $m = 1, \cdots, N/2$ and $k = 1, \cdots, K$. K is the number of data records of length N points, x is an individual record, and m and n are vector indices that can apply to time or frequency. To save computation time, only the first half of the frequency vector is used ($m = 1, \cdots, N/2$), since the second half is conjugate symmetric and thus contains the same information as the first half. Matlab's FFT function does not include the factor $1/N$, and therefore the values returned by Matlab's FFT algorithm must by multiplied by 1/N in order to match Eq. (4.2).

---

any region of the spectrum with zero energy causes undefined values from division by zero. This problem is solved with the addition of a small level of white Gaussian noise to each signal before computation of its Fourier transform. To ensure that the noise would have minimal impact on the signal, the noise level was set to be 40 dB below signal level for each record. In practice, it would not be necessary to add noise to measured data because the recording system would already have a noise floor, thus eliminating the danger of dividing by zero.

5. Estimate the spectra according to the following discretized formulas, where X is the Fourier transform of the pressure signal p and Y is the Fourier transform of the squared pressure signal p^2.

   (a) Power spectral density S_{pp}:

$$S_{pp}(m) = \frac{1}{K}\sum_{k=1}^{K} X_k^*(m)X_k(m) \tag{4.3}$$

   (b) Bispectrum S_{ppp}:

$$S_{ppp}(m,n) = \frac{1}{K}\sum_{k=1}^{K} X_k^*(m+n)X_k(m)X_k(n) \tag{4.4}$$

   (c) Bispectrum derivative factors S_{p^2pp}, S_{pp^2p}, and S_{ppp^2}:

$$S_{p^2pp}(m,n) = \frac{1}{K}\sum_{k=1}^{K} Y_k^*(m+n)X_k(m)X_k(n) \tag{4.5}$$

$$S_{pp^2p}(m,n) = \frac{1}{K}\sum_{k=1}^{K} X_k^*(m+n)Y_k(m)X_k(n) \tag{4.6}$$

$$S_{ppp^2}(m,n) = \frac{1}{K}\sum_{k=1}^{K} X_k^*(m+n)X_k(m)Y_k(n) \tag{4.7}$$

   (d) Bispectrum derivative function dS_{ppp}/dx:

$$\begin{aligned}\frac{d}{dx}S_{ppp}(m,n) = j\eta[&f(m)(S_{pp^2p}(m,n) - S_{p^2pp}(m,n)) \\ &+ f(n)(S_{ppp^2}(m,n) - S_{p^2pp}(m,n))]\end{aligned} \tag{4.8}$$

   (e) Bicoherence b:

$$\hat{b}(m,n) = \frac{\left|\frac{1}{K}\sum_{k=1}^{K} X_k(m)X_k(n)X_k^*(m+n)\right|}{\left[\frac{1}{K}\sum_{k=1}^{K}|X_k(m)X_k(n)|^2\right]^{1/2}\left[\frac{1}{K}\sum_{k=1}^{K}|X_k^*(m+n)|^2\right]^{1/2}} \tag{4.9}$$

(f) Skewness function s:

$$\hat{s}(m,n) = \frac{\left|\frac{1}{K}\sum_{k=1}^{K} X_k(m)X_k(n)X_k^*(m+n)\right|}{\left[\frac{1}{K}\sum_{k=1}^{K}|X_k(m)|^2\right]^{1/2}\left[\frac{1}{K}\sum_{k=1}^{K}|X_k(n)|^2\right]^{1/2}\left[\frac{1}{K}\sum_{k=1}^{K}|X_k^*(m+n)|^2\right]^{1/2}} \tag{4.10}$$

Note that in these computations, the spectra are directly based on the Fourier transforms and are not scaled according to specific units such as Pa^2/Hz. As a result, amplitude axes for the figures in Chap. 5 are given in arbitrary units.

It should also be noted that a Higher Order Spectral Analysis Toolbox exists for Matlab, but it was not used here. Code was written independently for this thesis in order to obtain greater clarity, understanding, and control of the analysis.

Chapter 5

Results

A variety of signals were propagated from initial state through shock formation and old age, up to $\sigma = 10$. Groups of related signals were then used to calculate spectra at these distances, which are shown in the figures of this chapter. These figures span multiple pages in order to include a variety of plots at a number of distances.

This chapter is laid out as follows. Each section corresponds to a different type of source waveform: sinusoids, bifrequency sources, narrowband noise, and wideband noise. The evolution of the waveforms and spectra over distance are described in the most detail in Sec. 5.1, the subject of which is radiation from a monofrequency source, and noteworthy differences between source waveform types are discussed in the remaining sections.

The figures in each of the sections in this chapter are structured into four subsections of two pages each. The first two pages of each figure show the full waveform in the left column and ten cycles of the waveform in the right column. The next two pages show power spectral density S_{pp} in the left column and quad-spectral density Q_{p^2p} in the right column. After that, the bispectrum S_{ppp} appears in the left column and its rate of change dS_{ppp}/dx

appears in the right column. Finally, bicoherence b appears in the left column and skewness function s appears in the right column.

Each figure subsection is comprised of six rows—one row for each distance. The distances at which these plots are displayed range from $\sigma = 0$ to $\sigma = 10$, chosen to show the evolution of the waveforms and spectra.

All plots related to a given source waveform are included within a single figure, but information about the source and distance is provided in a heading on every page.

5.1 Initially Sinusoidal Waves

The simplest source waveforms contain just one frequency, expressed as a sinusoid. All signals here began with unity amplitude and random phase. Figure 5.1 shows the evolution of an initially sinusoidal waveform as it is propagated nonlinearly to $\sigma = 10$.

The first two pages of Fig. 5.1 show the full waveform on the left and a portion of the waveform on the right. The full waveform provides an overview of the waveform envelope. For waves with initially sinusoidal conditions, the envelope appears flat. Because we are modeling propagation that is essentially lossless except at shocks, the peak-to-peak amplitude remains constant until shock formation, which occurs at $\sigma = 1$. The amplitude then decreases as energy is dissipated at the shocks and the wave assumes a stable decaying sawtooth shape.

The portion of the waveform on the right is ten cycles long to provide a detailed view of the waveform steepening. At $\sigma = 0$, the waveform is a sinusoid because it has not yet begun propagation. As the wave propagates, the peaks travel faster than the troughs, thus forming shocks. Individual data points have been plotted to show that the waveform is sufficiently resolved even at its shocks, as discussed in Sec. 4.1.

The next two pages of Fig. 5.1 show plots of spectral quantities S_{pp} and Q_{p^2p}. At $\sigma = 0$, only one spike appears in S_{pp}, as a sinusoidal wave contains energy at only one frequency. Nonlinear propagation causes the generation of harmonics, which begin to grow immediately, even at $\sigma = 0.01$. The amplitudes of the harmonics are consistent with the known solution, as was shown in Fig. 4.1. Recall that noise was added only to waveforms used in the calculation of the normalized spectra, so no noise was added to the waveforms used in computing power spectral density. As a result, the -40 dB noise level discussed in a footnote in Sec. 4.2 does not apply here. The amplitudes of S_{pp} and Q_{p^2p} are based on the original scaling of the waveforms and the use of the formulas listed in Sec. 4.2.

Although S_{pp} is plotted on a decibel scale, Q_{p^2p} is plotted on a linear scale to show the sign of the quantity. For σ approaching zero we expect two spikes, one at $f/f_0 = 1$ and then another at $f/f_0 = 2$ with half the amplitude and opposite sign, as predicted by Eq. (3.88). From the analysis in Sec. 3.4 we also expect all higher harmonics to go to zero as $\sigma \to 0$. This behavior is clearly demonstrated at $\sigma = 0.01$, where a downward spike with value -6×10^{-4} is

followed by an upward spike with value 3×10^{-4}. We do not see exactly the expected behavior at $\sigma = 0$, but recall that Eq. (3.88) was derived by assuming that the wave has propagated a very small but nevertheless finite distance away from the source in order to account for initial generation of the second and third harmonics. At $\sigma = 0.01$ we see from Eq. (3.89) that the value of Q_{p^2p} at $f/f_0 = 3$ is four orders of magnitude smaller than the values at $f/f_0 = 1$ and $f/f_0 = 2$. At $\sigma = 0$ the waveform contains only the source frequency, and from Eqs. (3.85)–(3.87) we see that $Q_{p^2p} \to 0$ as $\sigma \to 0$. The reason for the computed nonzero values of Q_{p^2p} shown at $f/f_0 = 1$ and $f/f_0 = 2$ for $\sigma = 0$ is most likely associated with machine precision; note that the values at $\sigma = 0$ are 15 orders of magnitude smaller than at $\sigma = 0.01$.

As the wave propagates, positive spikes in Q_{p^2p} appear at all harmonics. Energy leaves the fundamental, as shown by the negative spike, and this energy enters the other harmonics, as shown by the positive spikes. Up to $\sigma = 0.3$ it can be seen that the second harmonic is the main beneficiary of the energy leaving the source frequency component. Once sufficient energy has developed at $f/f_0 = 2$, this frequency component also provides energy to other harmonics, which is indicated by a sign change in the spike at $f/f_0 = 2$ between $\sigma = 1$ and $\sigma = 3$. In the sawtooth region $3 \leq \sigma \leq 10$, Q_{p^2p} is characterized by a single prominent negative spike at the source frequency.

Following the plots of S_{pp} and Q_{p^2p} in Fig. 5.1, surface plots are provided for S_{ppp} (left columns) and dS_{ppp}/dx (right columns). At $\sigma = 0$ we expect the bispectrum to be zero, as no harmonic interactions have yet taken place.

However, peaks exist at frequency coordinates (1,1), (1,0), and by symmetry, (0,1), where coordinates are in the form of $(f_1/f_0, f_2/f_0)$. This occurs because all signal energy is concentrated at the fundamental frequency, and when the bispectral density is calculated numerically, interactions associated with that frequency bin are seen as larger than interactions of frequencies in bins that contain no energy at all. As the wave begins to propagate at $\sigma = 0.01$, the main peak jumps by more than 50 dB and many other peaks appear. This behavior further suggests that the bispectrum at $\sigma = 0$ is nonzero for numerical rather than physical reasons.

Another physical-versus-numerical issue is found in the surface plots of S_{ppp}, where amplitude is very low outside the initial peak. This region of low values appears as a plateau. However, the plateau is not a physical feature but rather a computational limit as the small pressure amplitudes approach machine precision. As energy spreads throughout the frequency space during propagation, this floor gradually elevates.

Spreading of energy to harmonics of the source frequency is shown in the plots of S_{ppp} as the appearance of spikes at integer values of $(f_1/f_0, f_2/f_0)$. These spikes begin small but then grow as energy accumulates at the corresponding frequencies. As the wave propagates through the sawtooth region beyond $\sigma = 3$, all spikes decrease in amplitude with the wave's gradual loss of energy. This behavior is expected, as the system is nondispersive, and therefore all spectral interactions are very efficient.

The derivative dS_{ppp}/dx is shown in the right column next to the bis-

pectrum S_{ppp} [recall Eq. (3.59)]. It was found numerically that for initially sinusoidal waveforms, dS_{ppp}/dx is purely imaginary at integer multiples of the fundamental frequency. The imaginary part of this quantity was plotted in order to enable the observation of sign change. Just as the sign of Q_{p^2p} indicates the flow of energy into or out of a frequency bin, it is possible that the sign of dS_{ppp}/dx indicates a flow of energy into or out of frequency bins associated with certain spectral interactions. All spikes in dS_{ppp}/dx are initially positive [although for $\sigma < 1$ only the spike at (1,1) is easily seen in the figures], but at $\sigma = 1$ the spike at (1,1) is negative, and several more lower harmonics become negative as the wave reaches $\sigma = 3$. The sign changes observed for these harmonics occur at distances similar to where the sign of Q_{p^2p} changes.

Note also that for $\sigma > 0$ the shape of the quad-spectral density matches closely that of the derivative $\Im\{dS_{ppp}/dx\}$ in a slice across the fundamental frequency, as might be expected since both functions predict development of their corresponding spectral densities. This behavior is especially noticeable in Fig. 5.4, which provides spectral plots for a wideband source condition.

The last two pages of Fig. 5.1 show the bicoherence and skewness function side by side. At $\sigma = 0$, both the bicoherence and skewness function appear to have no structure at all, which might be expected, as the peaks observed in the bispectrum are canceled out through division by the power spectral density [recall Eqs. (2.16) and (2.20)]. At $\sigma = 0.01$, the normalized bispectra already show signs of structure as spikes at (1,1) appear well above the background noise. The amplitude of this spike is given by the peak level

of the scale, shown as a bar next to each plot. As the wave propagates, spikes in the bicoherence and skewness function spread across the domain at integer coordinates. Since these functions compare spectral interaction to spectral energy, this behavior shows that the amount of interaction at these frequency pairs is large compared to the energy present at each frequency component.

For consistency with related literature [4, 7] and for precise visualization of frequency bins, the bicoherence and skewness function have been plotted as a flat image rather than as a three-dimensional surface. Although it may be difficult to see the structure in the present case of a monofrequency source due to the narrowness of the spikes, structure will be more clearly apparent in the other waveform types shown in later sections.

At all distances, visual similarities between the bicoherence and skewness function suggest that both measures perform the same fundamental task of showing harmonic interactions relative to power spectral density. For cursory comparisons between datasets with records of identical length, the bicoherence may be adequate. However, the skewness function may be more reliable for comparison between datasets due to its independence of record length, as discussed by Hinich and Wolinsky [24]. As an additional benefit, the skewness function does not require any special calculation of bifrequency spectral density but rather can be assembled directly from the bispectrum and power spectral densities, as seen from Eq. (2.20).

Monofrequency Source

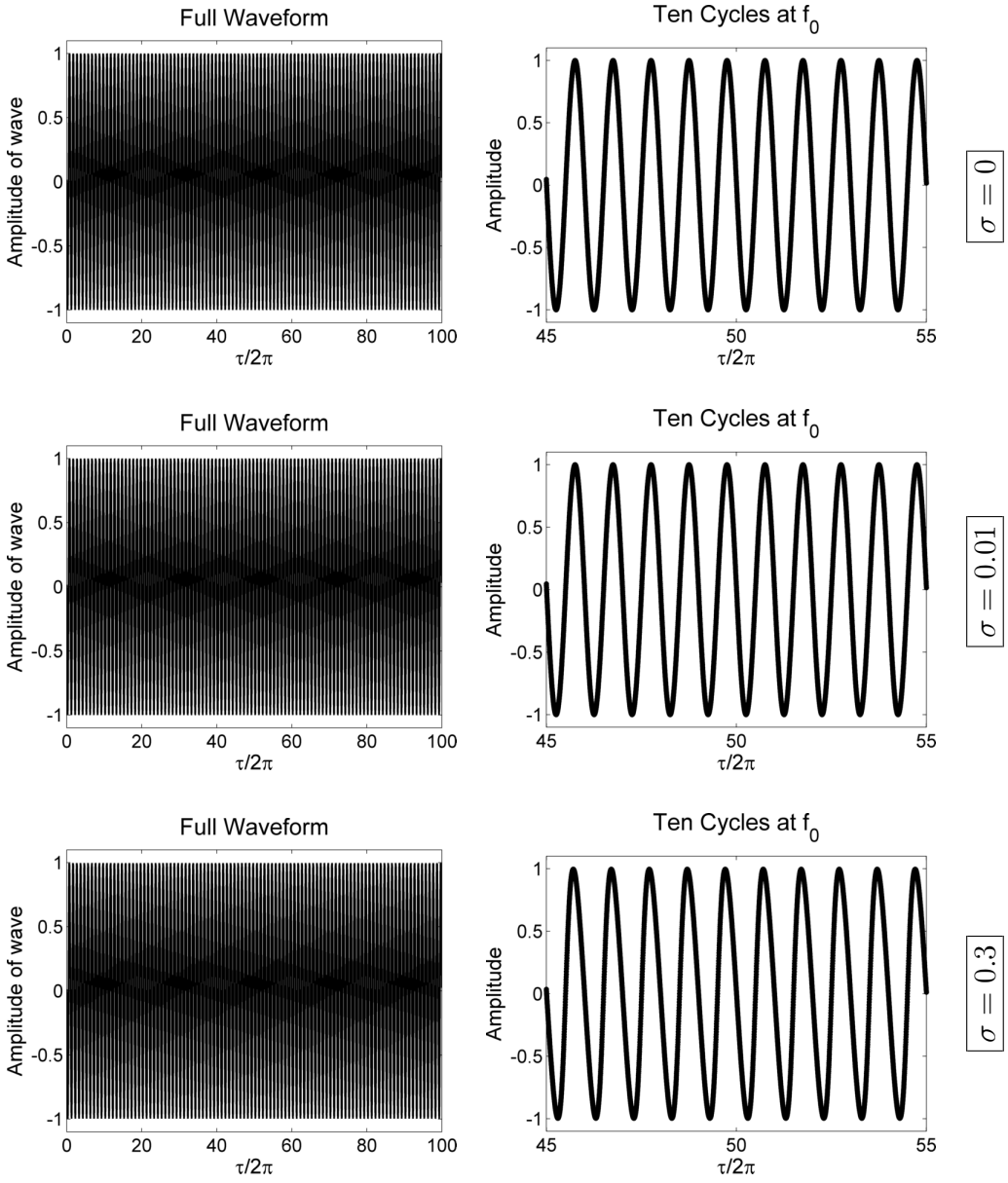

Figure 5.1: Waveforms and spectra for waves radiated by a monofrequency source.

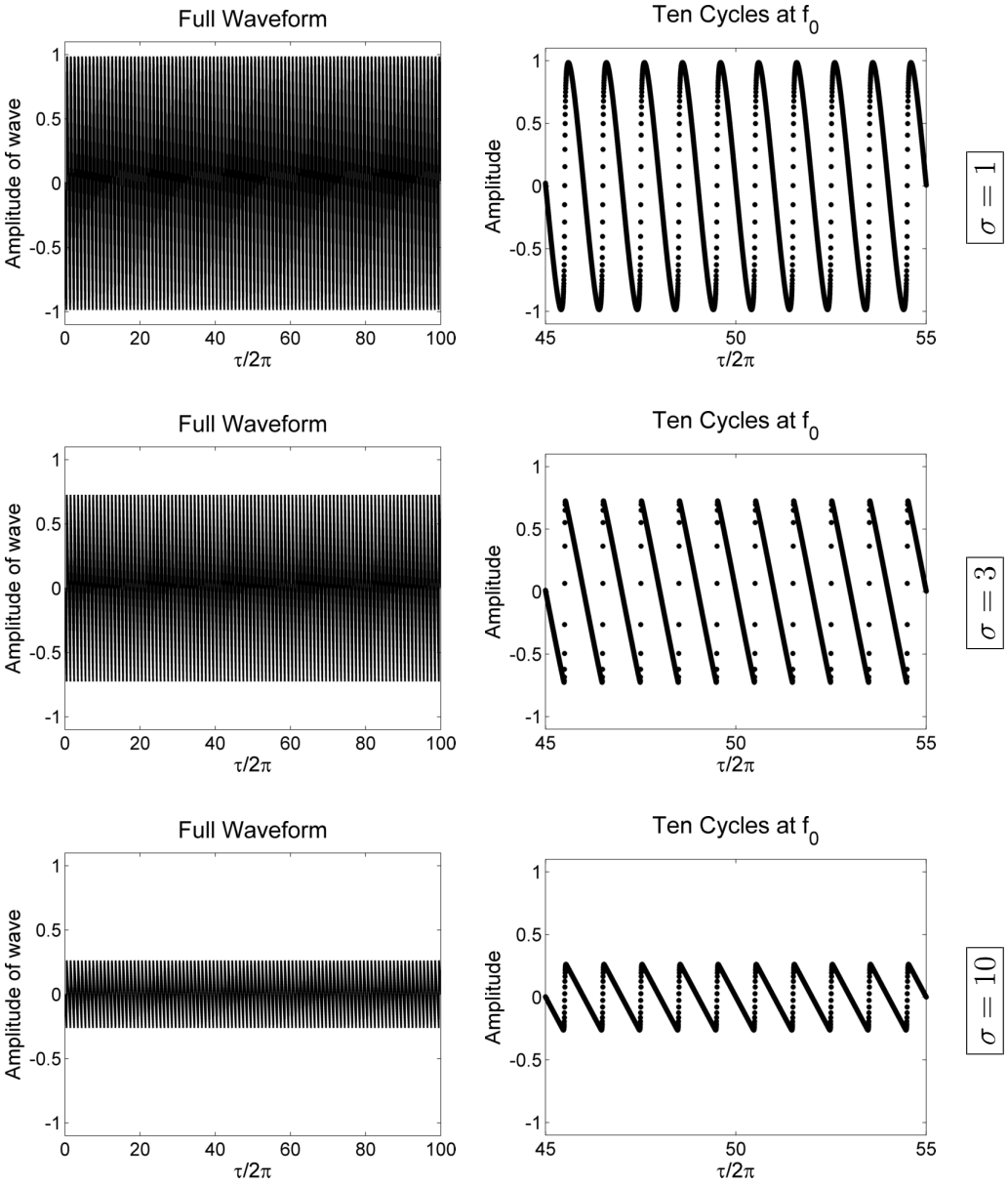

Figure 5.1 (continued).

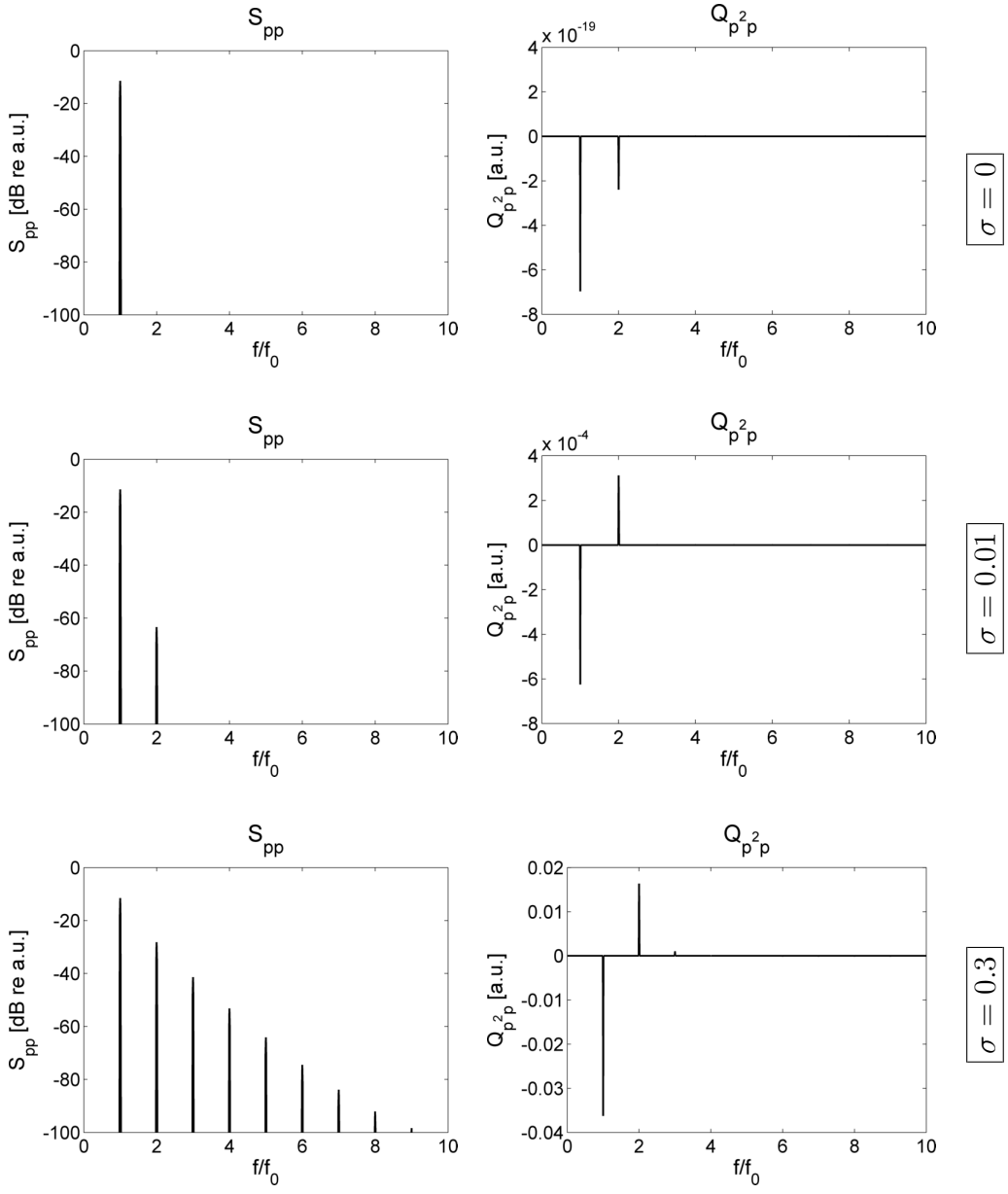

Figure 5.1 (continued).

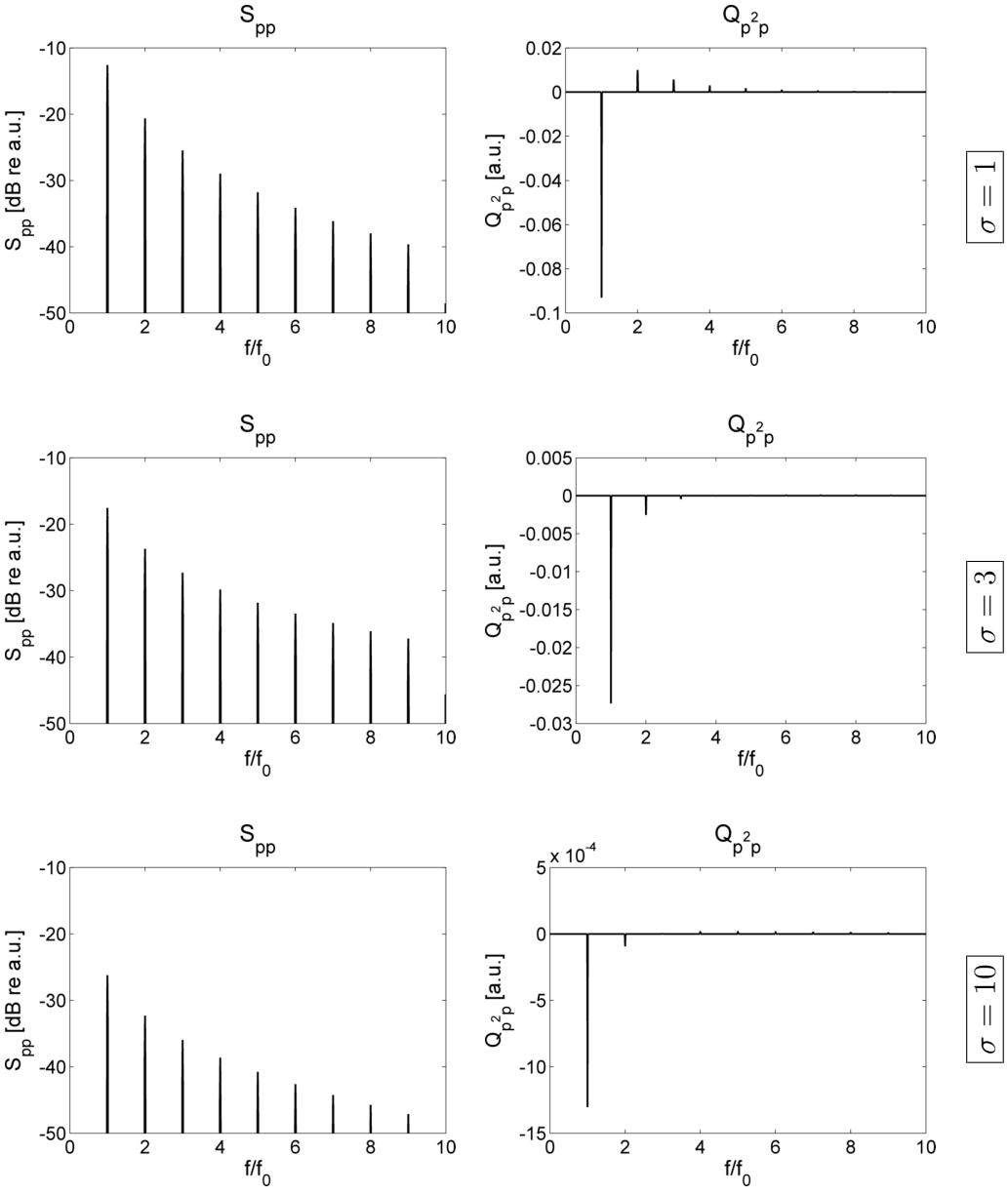

Figure 5.1 (continued).

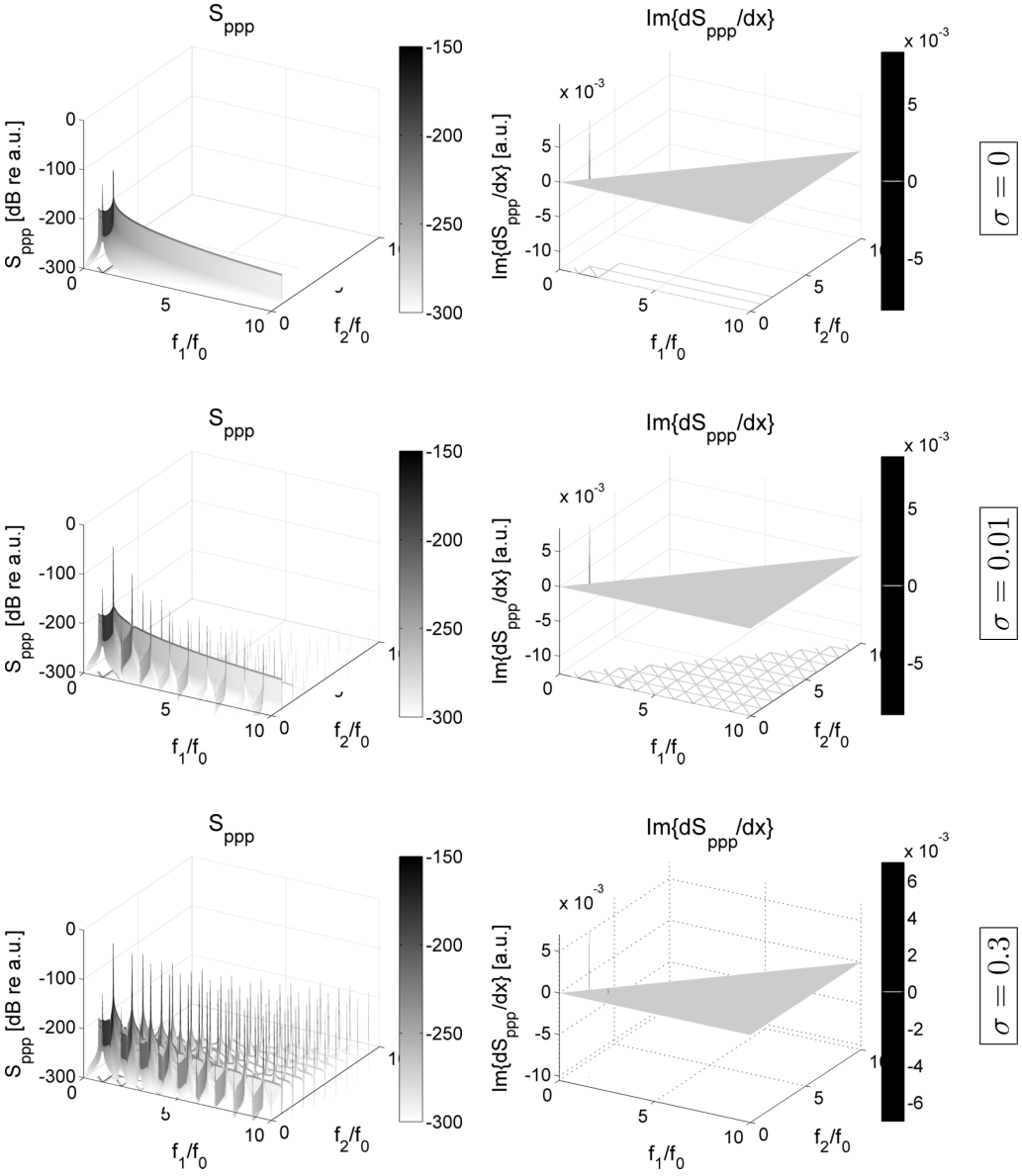

Figure 5.1 (continued).

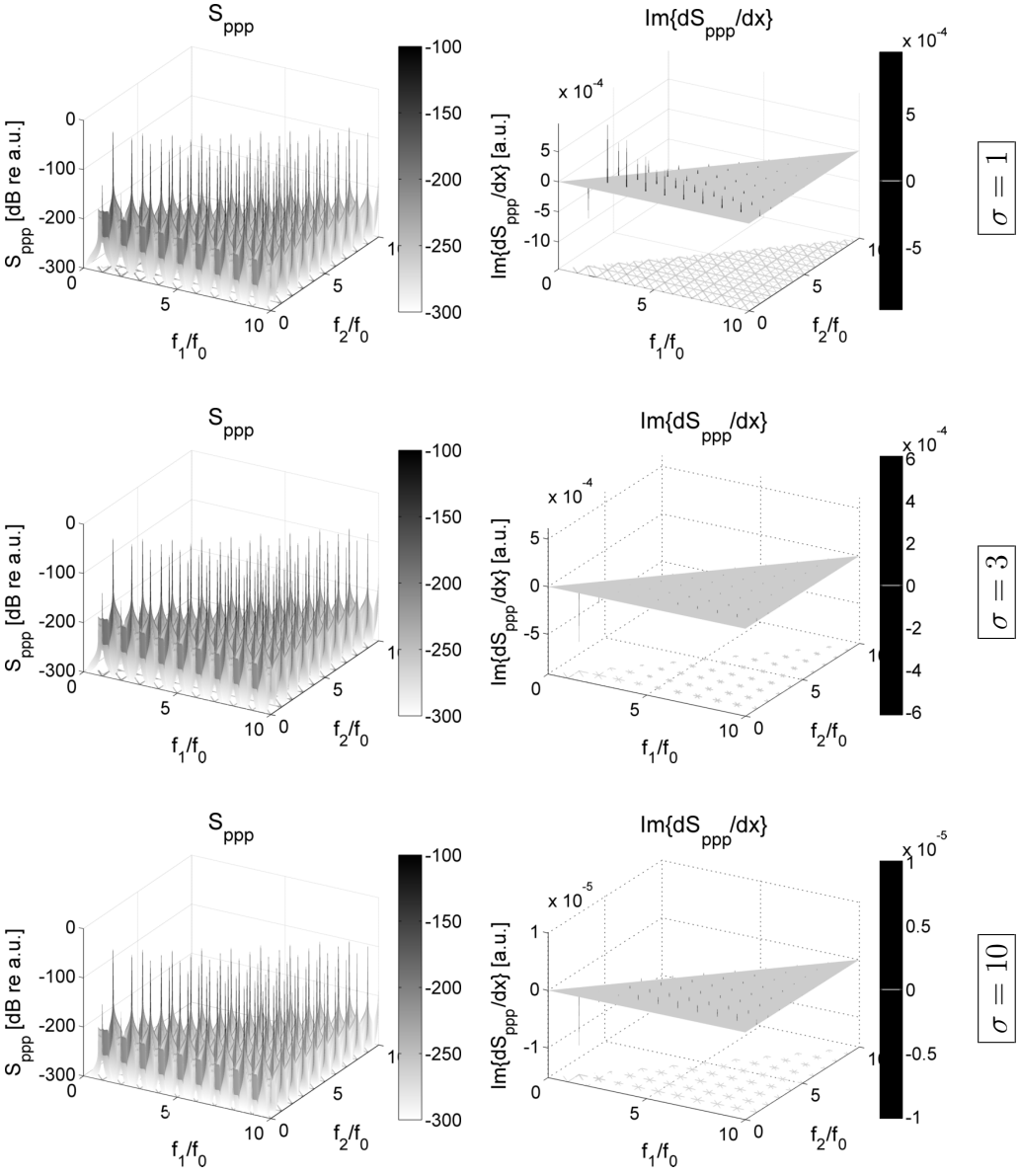

Figure 5.1 (continued).

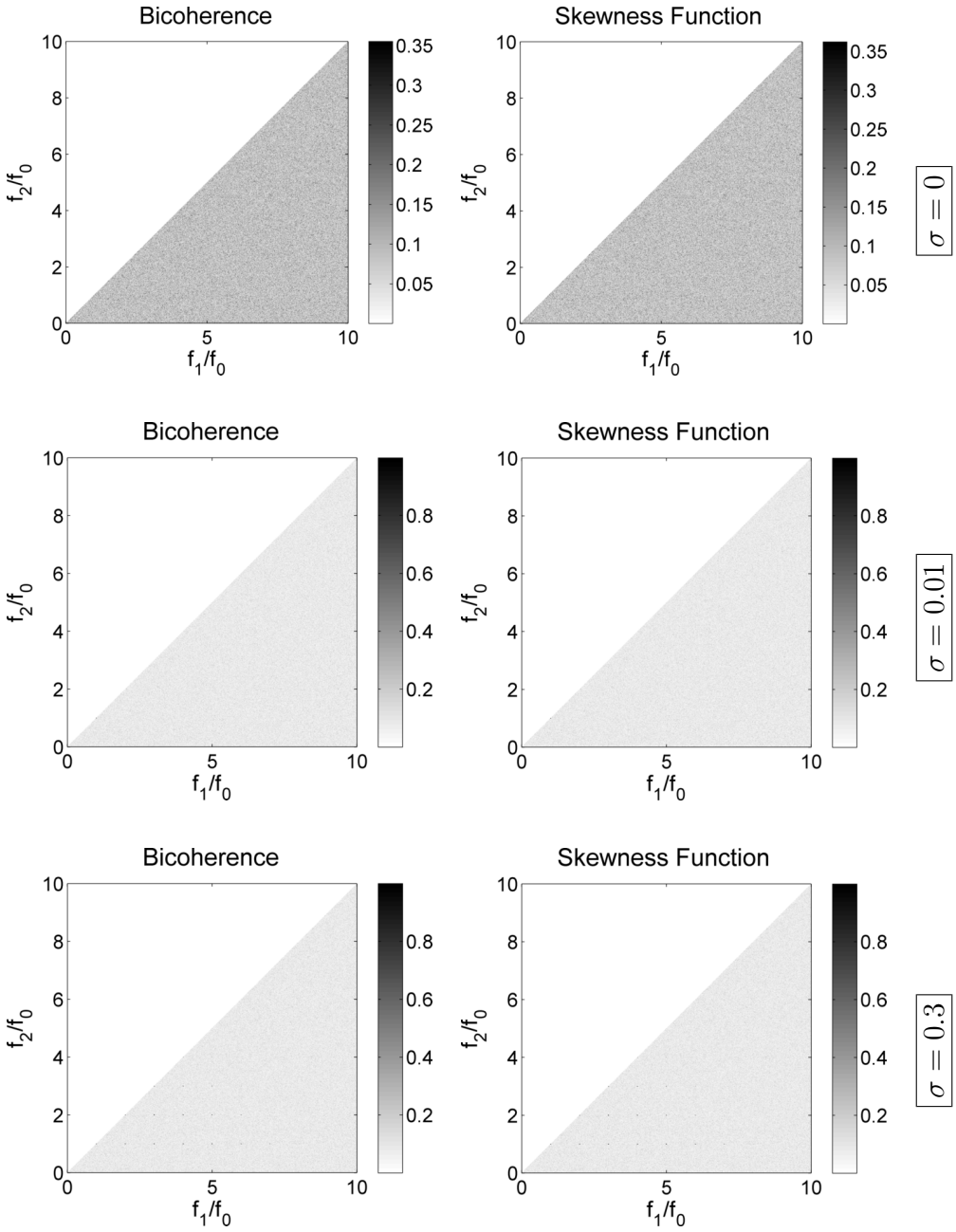

Figure 5.1 (continued).

Monofrequency Source

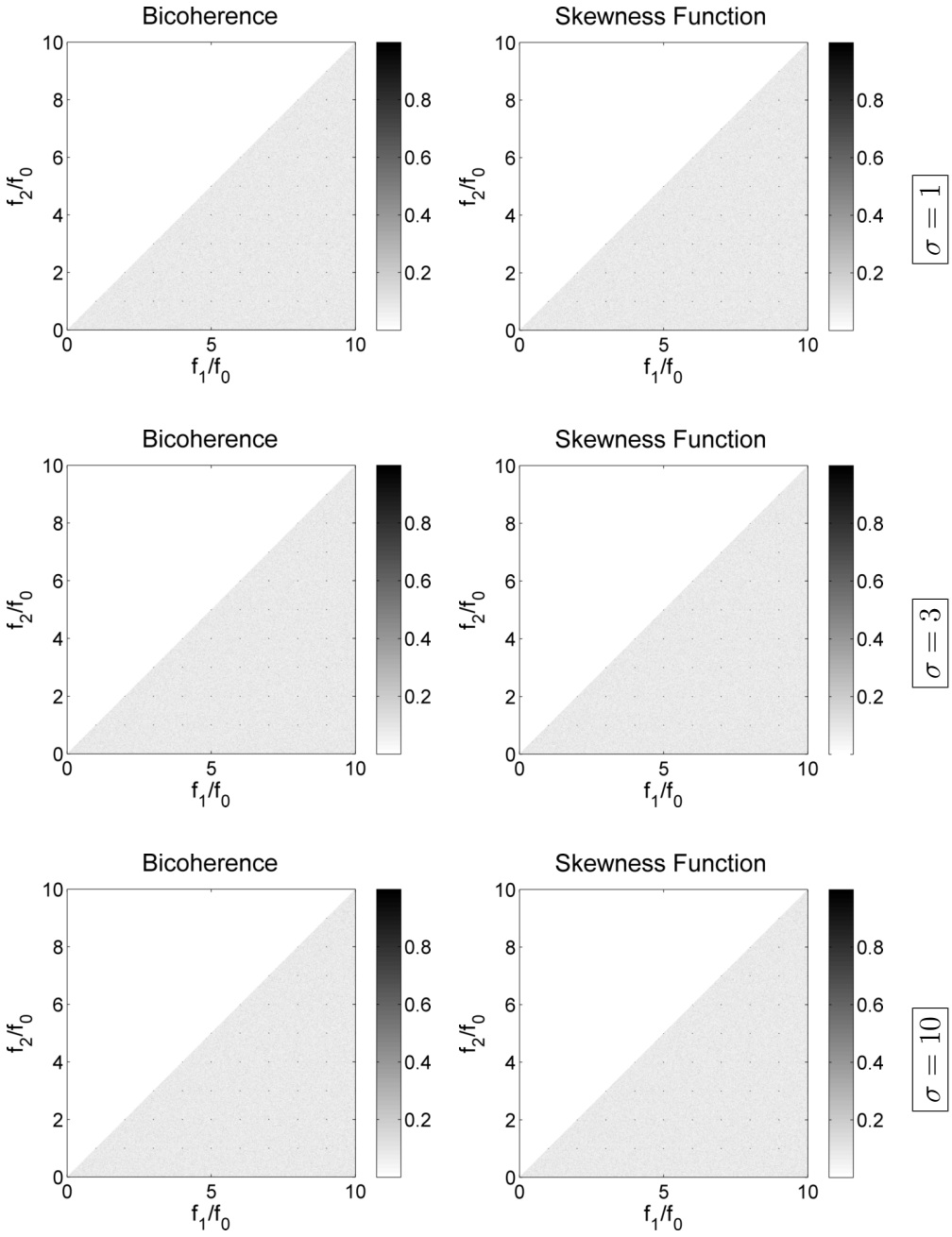

Figure 5.1 (continued).

5.2 Initially Bifrequency Waves

In this section we consider waves radiated from bifrequency sources. Every signal was created with a sinusoid at frequency $0.95f_0$ and another sinusoid at frequency $1.05f_0$, each with random phase. The phase was taken to be a random variable with a uniform probability density function between 0 and 2π. Figure 5.2 shows the waveforms and spectra for this source waveform at the same distances as in Fig. 5.1.

The presence of two dominant, neighboring frequencies in the waveform is revealed by a pattern of beats with a periodicity 10 times that of the mean source frequency. Shock formation still occurs at $\sigma = 1$, corresponding to a sinusoidal source radiating at the mean source frequency and at the same peak amplitude as the bifrequency source waveform.

Propagation of the initially bifrequency waveform is seen to generate a much richer frequency spectrum than propagation of sound from a monofrequency source, shown in Fig. 5.1. This is due in large part to the proximity of the two source frequencies, differing from one another by only 10%. It is convenient for discussion to express the source frequencies as $\frac{19}{20}f_0$ and $\frac{21}{20}f_0$, thus making the difference frequency generated by the primary waves $\frac{21}{20}f_0 - \frac{19}{20}f_0 = \frac{2}{20}f_0$, which is one tenth of the mean primary frequency f_0. Nonlinear propagation results in a power spectrum containing 20 times the density of spectral lines as in the case of a monofrequency source in Fig. 5.1, with spectral lines ultimately appearing at all integer multiples of $\frac{1}{20}f_0$. This proliferation of spectral lines may be illustrated as follows. For brevity we will

refer to the primary frequencies $\frac{19}{20}f_0$ and $\frac{21}{20}f_0$ as simply 19 and 21, meaning 19 or 21 times the frequency $\frac{1}{20}f_0$. Through quadratic nonlinearity the following interactions occur: 19 and 21 will generate the difference frequency 2, and then 2 will generate all of the "even frequencies" 4, 6, 8, etc. Both 19 and 21 will interact with all of these "even frequencies" to produce the "odd frequencies" 1, 3, 5, etc. Therefore every integer from 1 to 20 and beyond appears, resulting in 20 spectral lines in the frequency band from 0 and f_0 (and from f_0 to $2f_0$, etc.).

The evolution of the quad-spectral density is qualitatively the same as for the monofrequency source. At $\sigma = 0.3$ it shows, expectedly, that the second harmonic of each source frequency, and the sum frequency, are the main beneficiaries of the energy radiated at the source frequencies. By comparison, transfer of energy to the difference frequency is far less efficient. In the sawtooth region starting at $\sigma = 3$ and beyond, Q_{p^2p} looks much the same as for the monofrequency source. Note also that just as in Fig. 5.1, the shape of the derivative dS_{ppp}/dx along a single dimension exhibits similarity to the shape of the quad-spectral density.

Peaks in the bispectra begin as narrow spikes centered at the harmonics of the source frequencies, and more spikes grow around these regions as the wave propagates. After the wave passes $\sigma = 1$, these spikes become increasingly dense and difficult to distinguish from one another, since interactions occur between increasingly many frequency bins. This behavior is present in all of the plotted higher order spectra: bispectrum, derivative of the bispec-

trum, bicoherence, and skewness function.

As in Fig. 5.1, the normalized bispectra (bicoherence and skewness function) have no structure at $\sigma = 0$ but immediately show signs of structure upon propagation. The primary difference for the bifrequency case is that the spectral interactions occur at more frequency pairs compared to the monofrequency case. These narrow spikes spread to fill all sum and difference frequencies, resulting in a textured appearance.

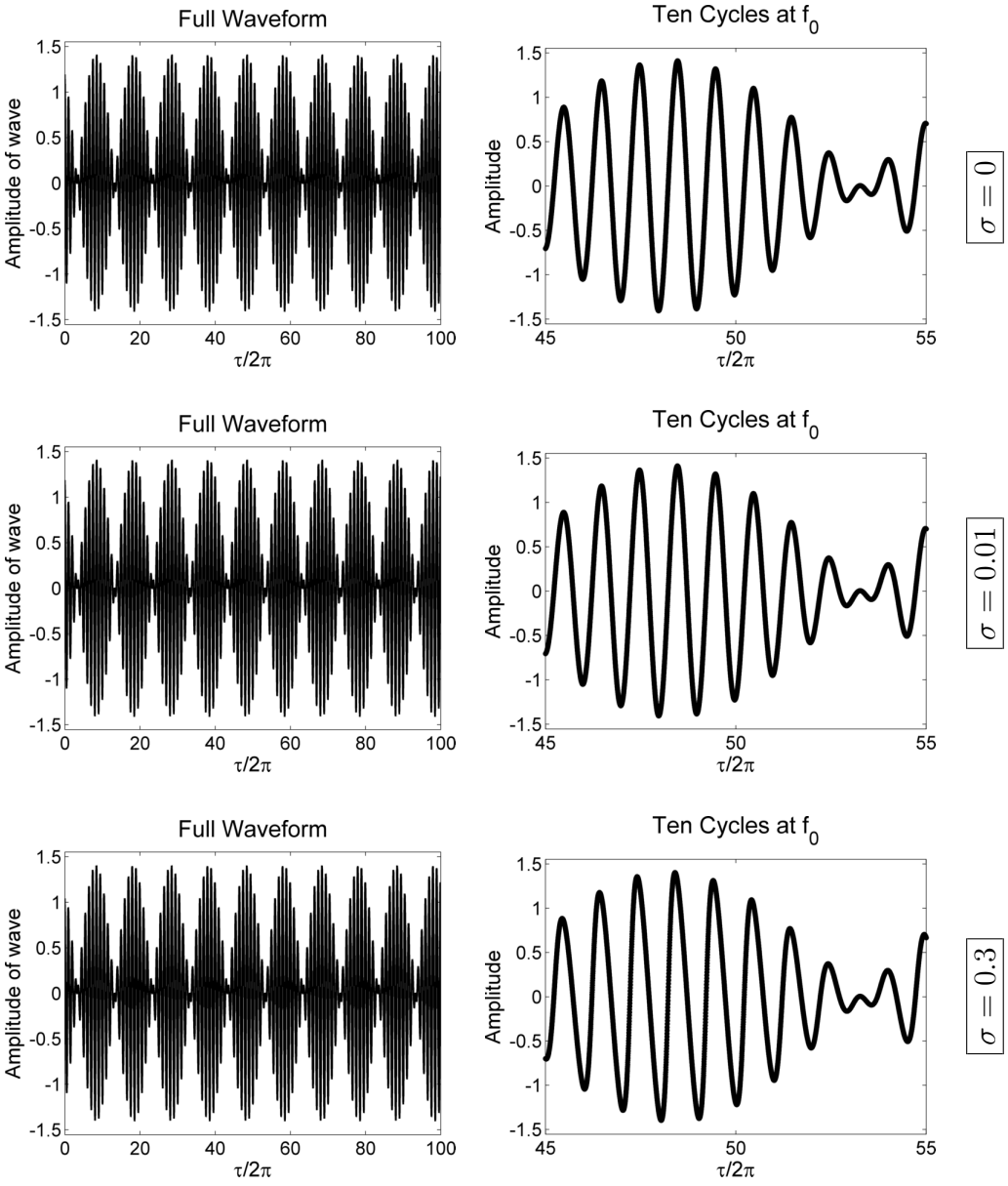

Figure 5.2: Waveforms and spectra for waves radiated by a bifrequency source.

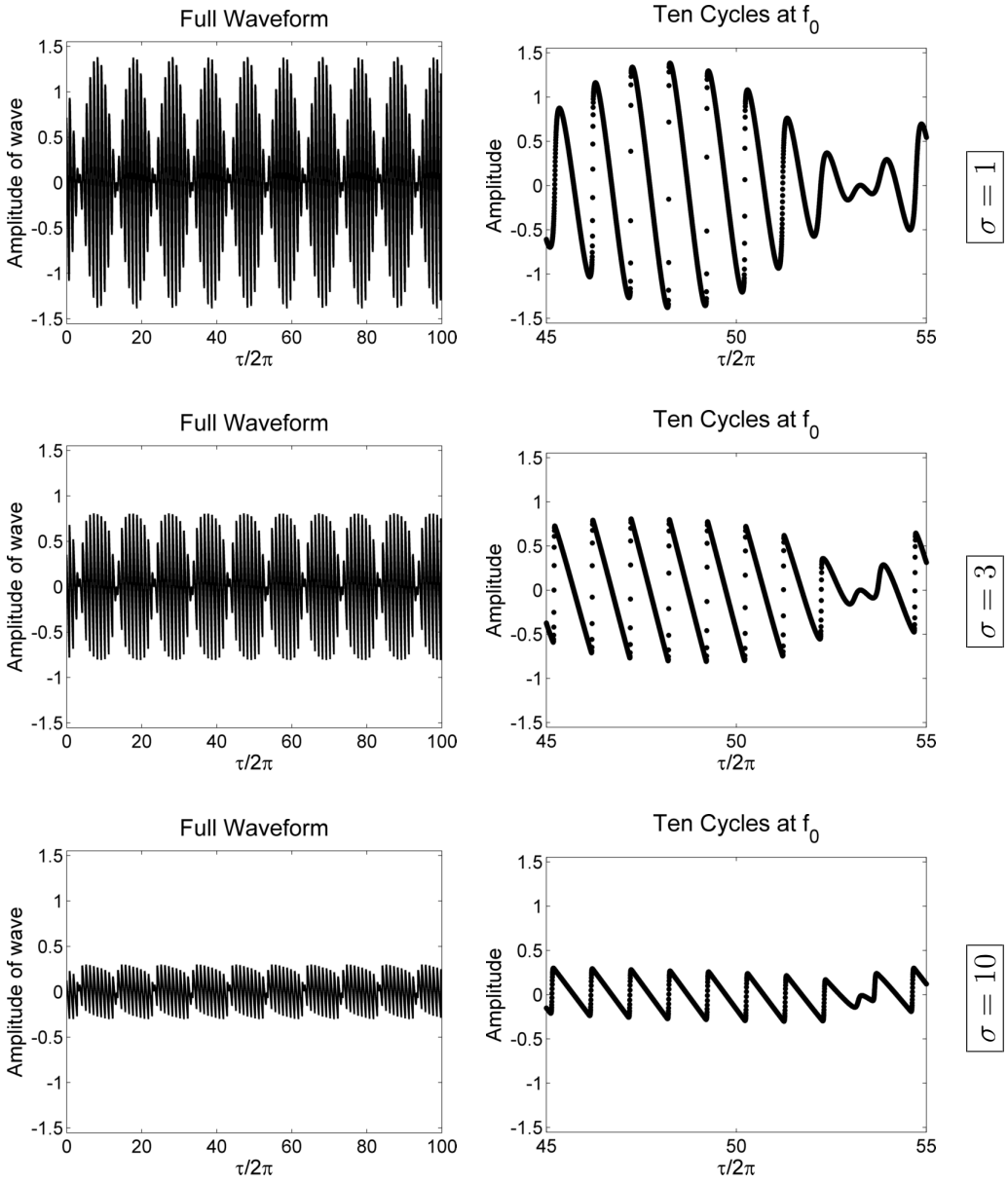

Figure 5.2 (continued).

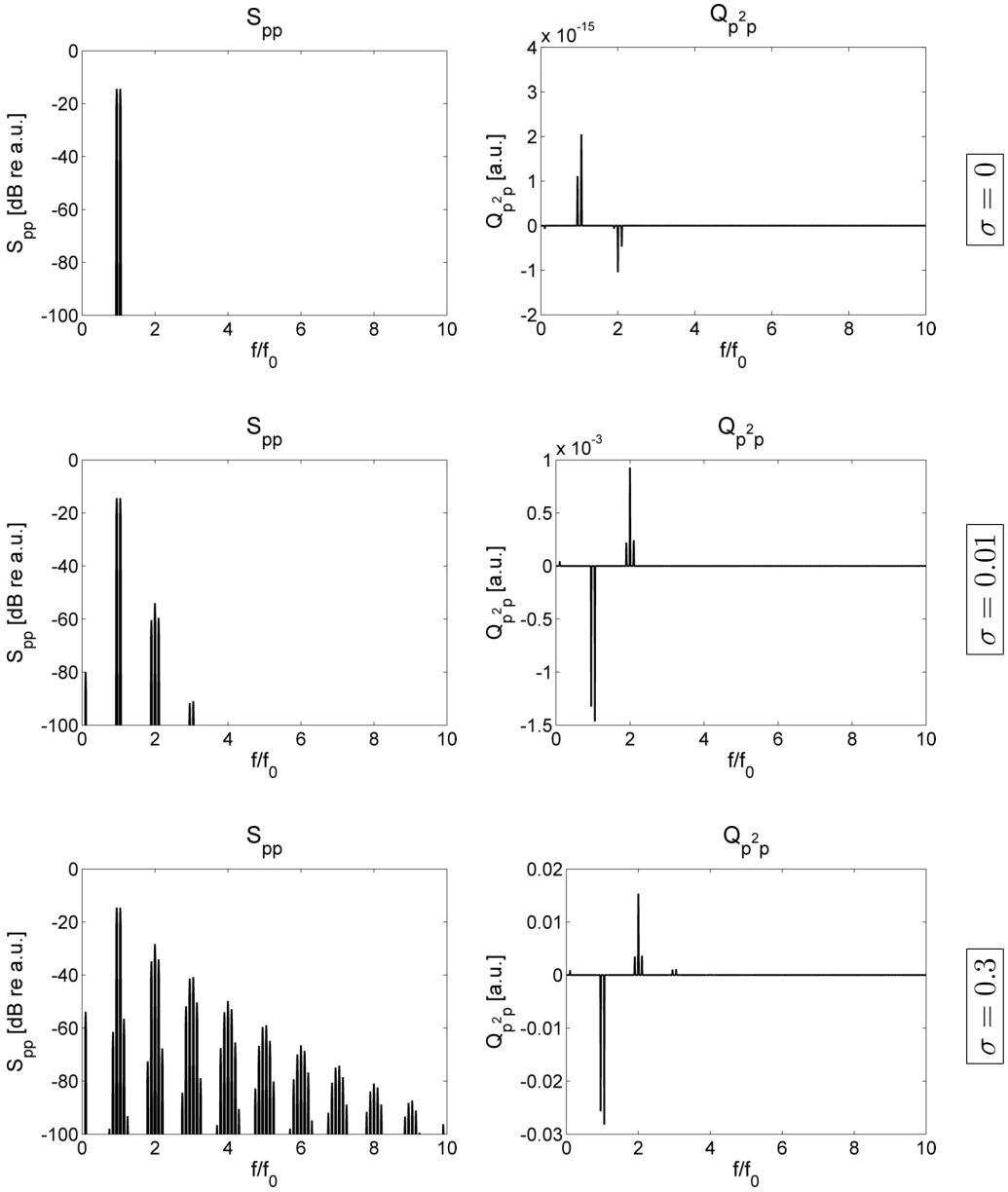

Figure 5.2 (continued).

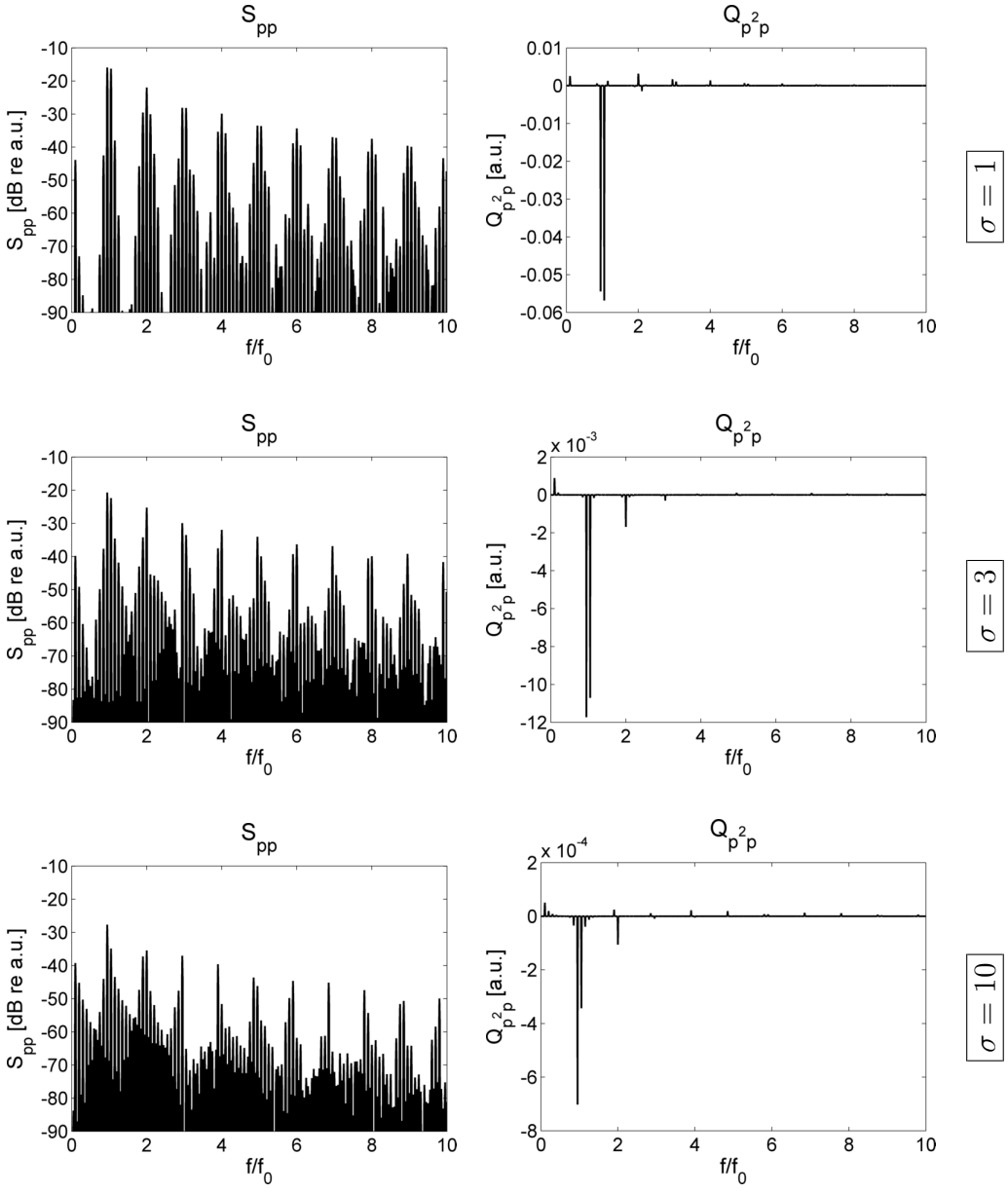

Figure 5.2 (continued).

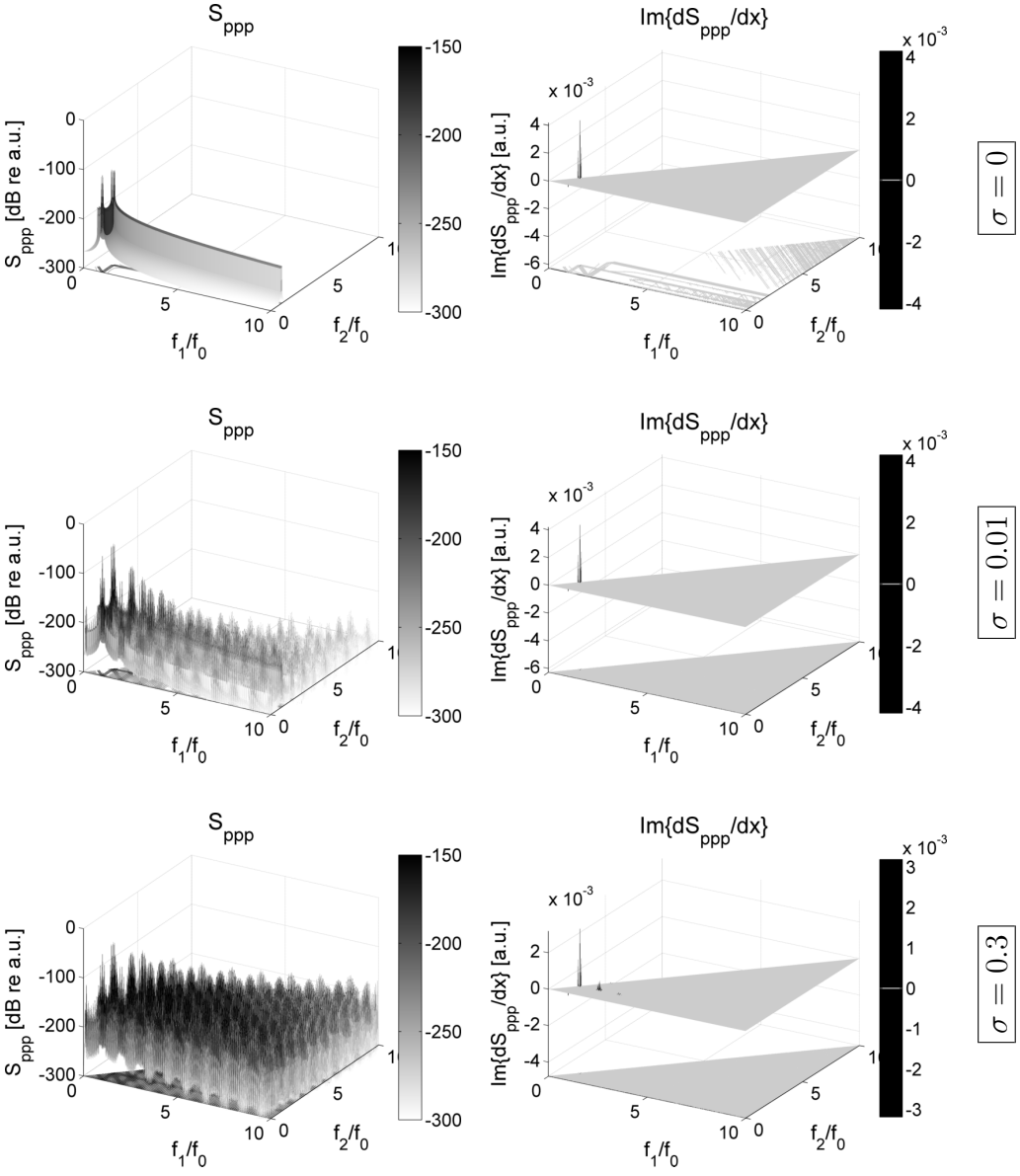

Figure 5.2 (continued).

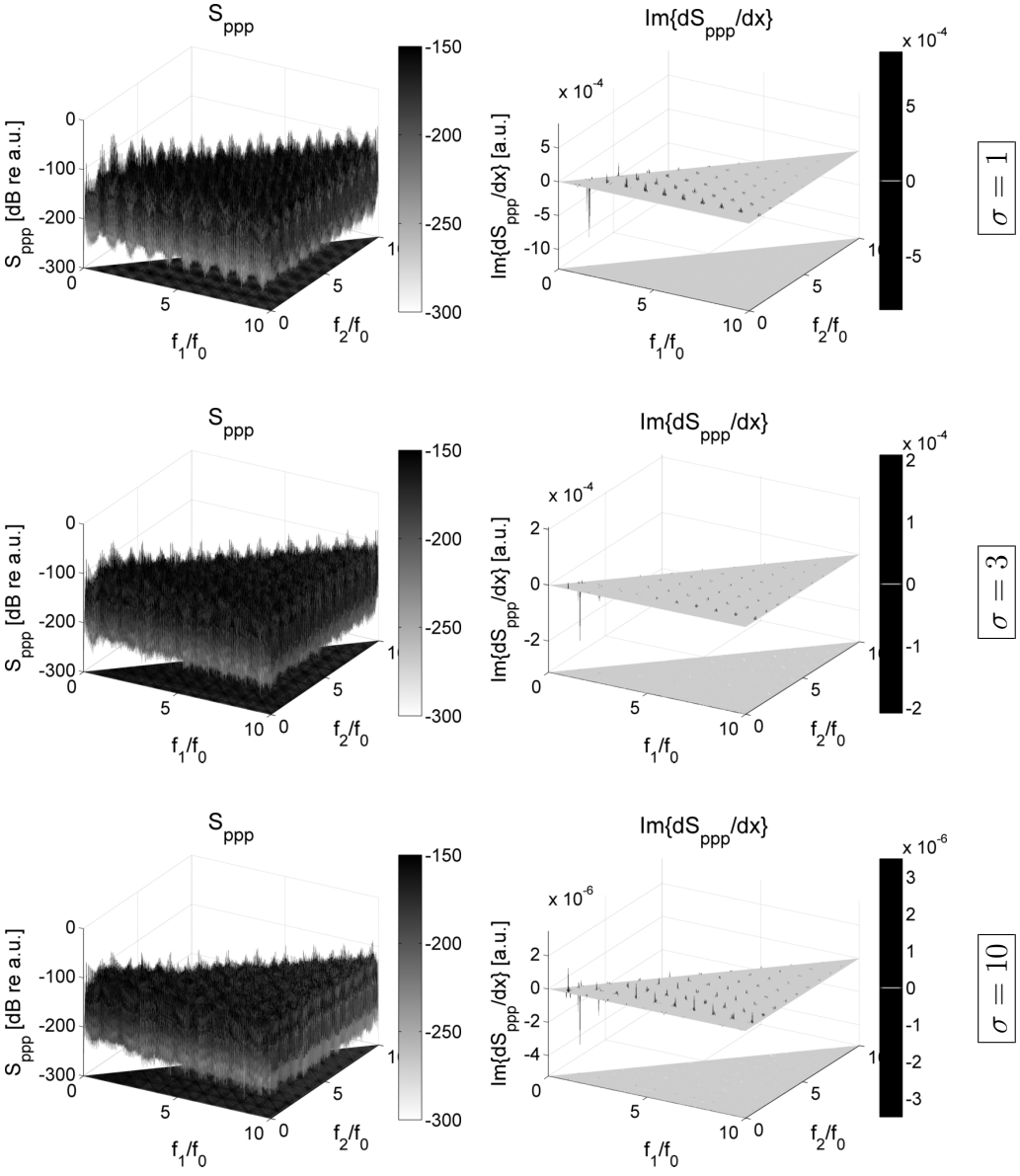

Figure 5.2 (continued).

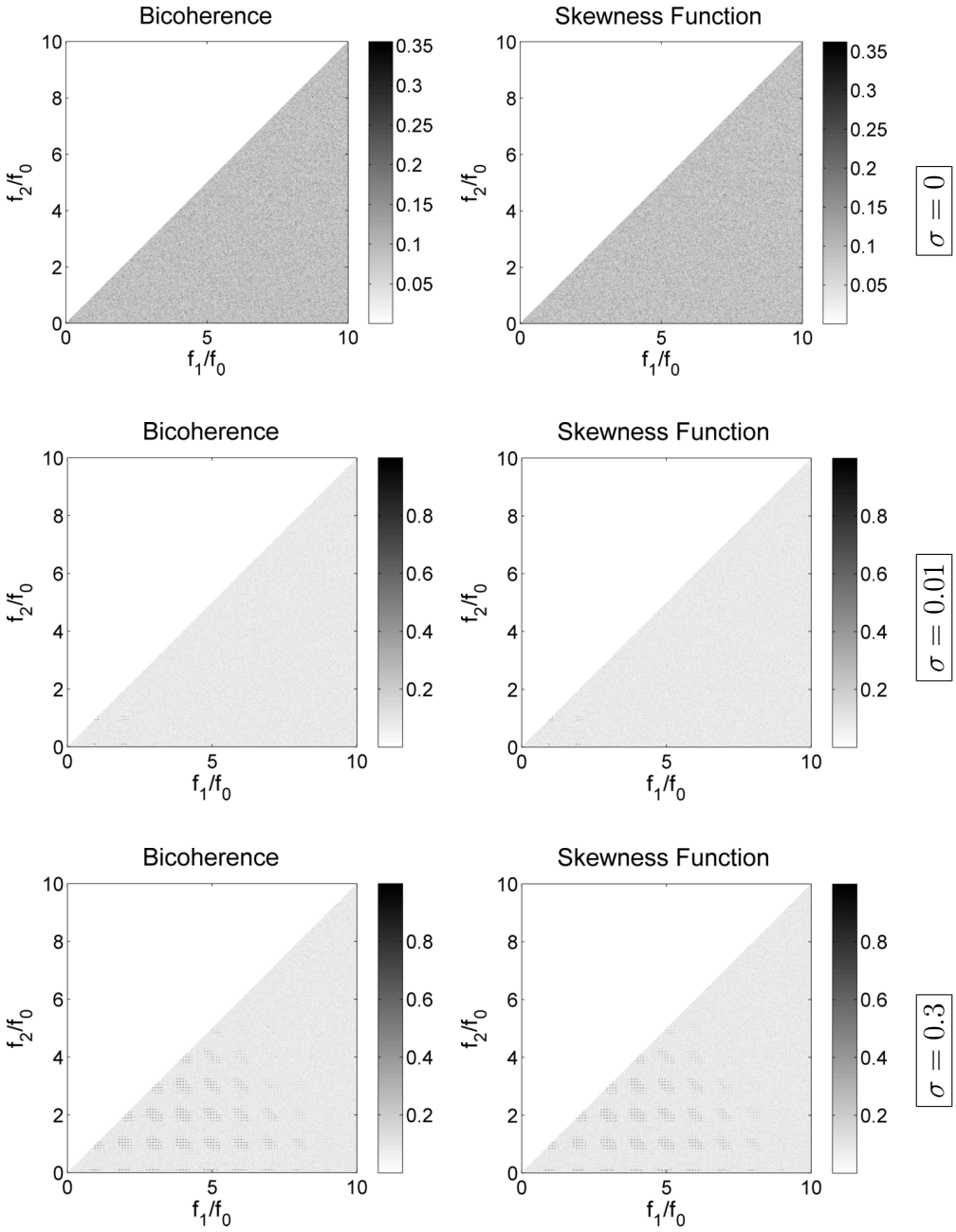

Figure 5.2 (continued).

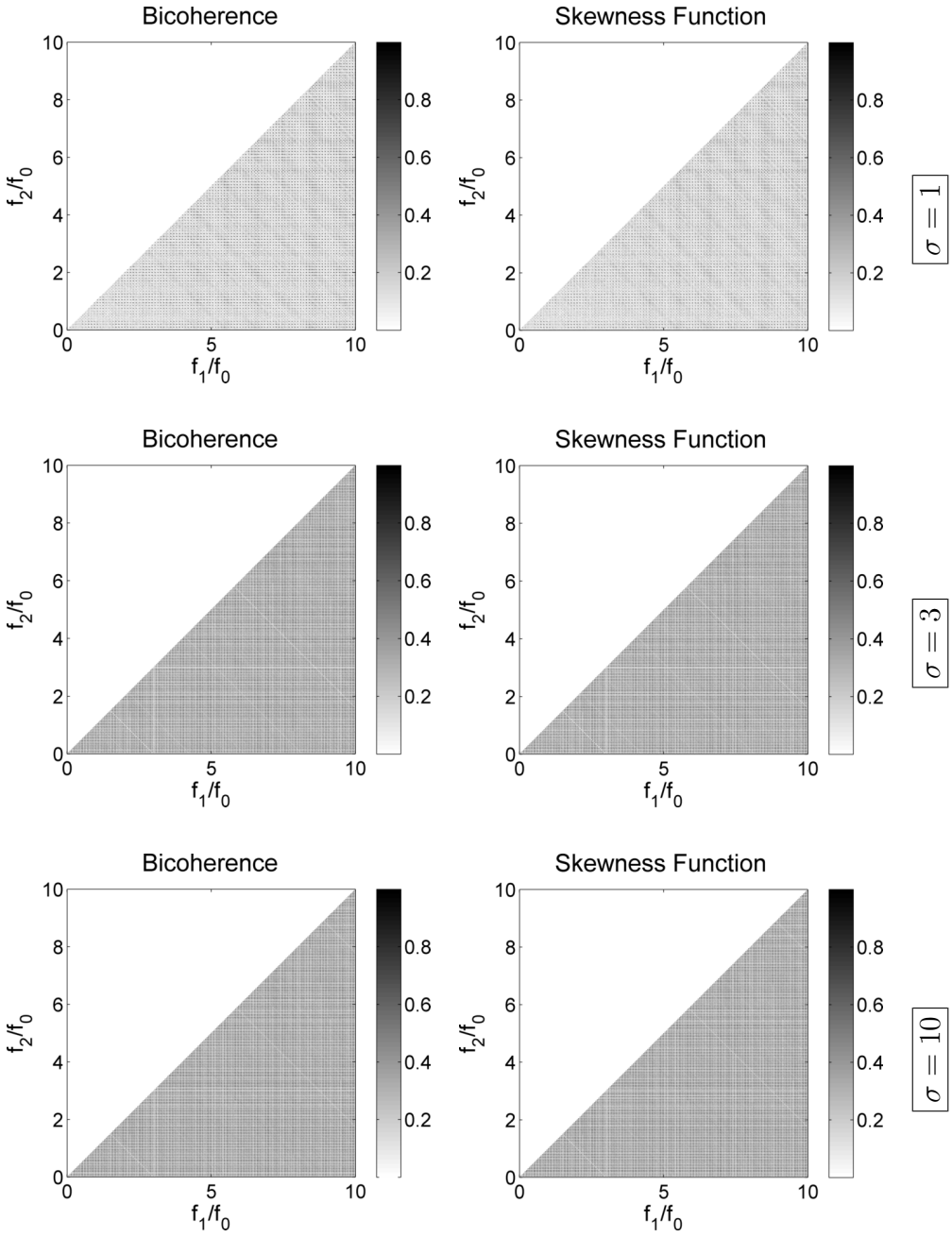

Figure 5.2 (continued).

5.3 Narrowband Noise

We now consider the evolution of waves that initially span the same frequency range as those of Sec. 5.2 ($0.95f_0$ to $1.05f_0$) but include all frequencies in between. The noise was generated by dividing the frequency band from $0.95f_0$ to $1.05f_0$ into ten equally spaced spectral lines with uniform amplitude, assigning each a random phase, summing them up, and then normalizing the resulting waveform to have the same rms value as a sinusoid with unit amplitude. Waveforms and plots for this case are provided in Fig. 5.3. Generally speaking, all of the plots are qualitatively the same as for the bifrequency source (Fig. 5.2) with the same bandwidth (10%). The main difference is that spectral lines in Fig. 5.2 have merged into continuous distributions in Fig. 5.3.

As the waveforms have been generated to contain frequency components exactly in line with the FFT frequency bins, one may expect the power spectral density to have a perfectly flat top. However, recall that a Hamming window is applied to every record for bispectral analysis, as is recommended by Nikias and Petropulu [16]. For consistency, this window is also applied to all other spectral calculations, and this windowing is the cause of the uneven top of the power spectral density.

The quad-spectral density can be both positive and negative near f_0 at $\sigma = 0$. However, we reiterate that the values of Q_{p^2p} are near numerical precision and are too small to be considered meaningful.

In the narrowband noise case, the bispectrum takes on an undulating

appearance, as opposed to the spiked appearance of Fig. 5.2. This occurs because of the continuous distribution of energy throughout the bandwidth. Furthermore, the increased number of frequencies available for interaction causes energy to spread faster to the frequency spaces between the harmonics. As a result, the total dynamic range of the bispectrum for a narrowband source is much smaller than that for a bifrequency source, especially beyond $\sigma = 1$.

For a continuous spectral distribution, the derivative of the bispectrum exhibits both positive and negative peaks in a given harmonic region, which is a pattern not shared here by the quad-spectral density. As dS_{ppp}/dx provides information about interactions between several frequencies, it is likely that energy is both entering and leaving the region of a given harmonic in ways that are not revealed by Q_{p^2p}.

Evidence that energy spreads quickly to the regions between the harmonics can also be found in the normalized bispectra (bicoherence and skewness function). These functions show vertical and oblique lines between the harmonics near $\sigma = 1$ where frequency interactions are taking place but power spectral density levels are low. These lines are not clearly visible in Fig. 5.2 because in the case of the bifrequency source condition the distinct frequency interactions form spikes instead of lines. As the wave propagates, the normalized bispectra eventually appear uniform in value, showing that interactions have spread to all frequency pairs.

Narrowband (10% Bandwidth) Source

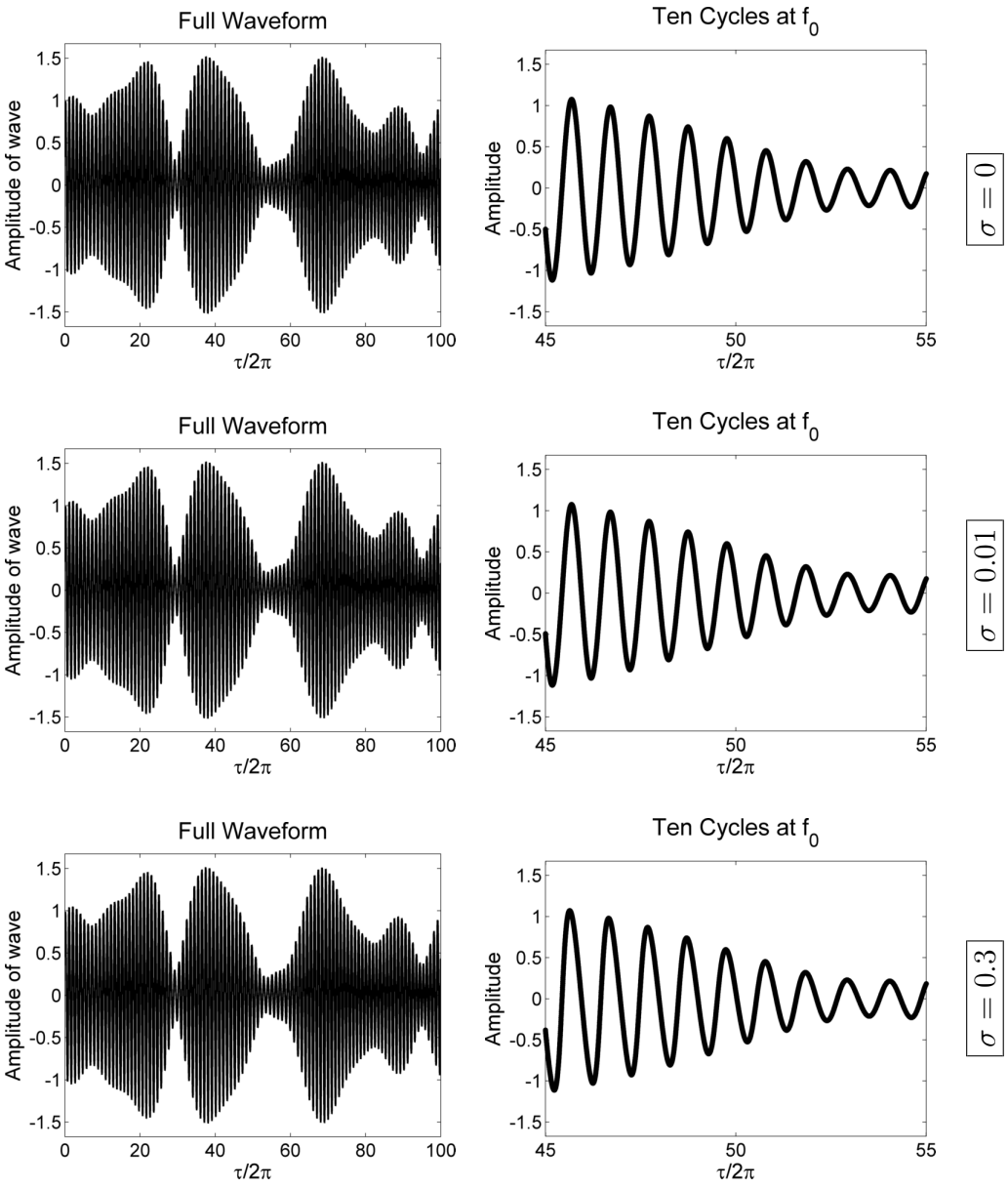

Figure 5.3: Waveforms and spectra for waves radiated by a narrowband source.

Narrowband (10% Bandwidth) Source

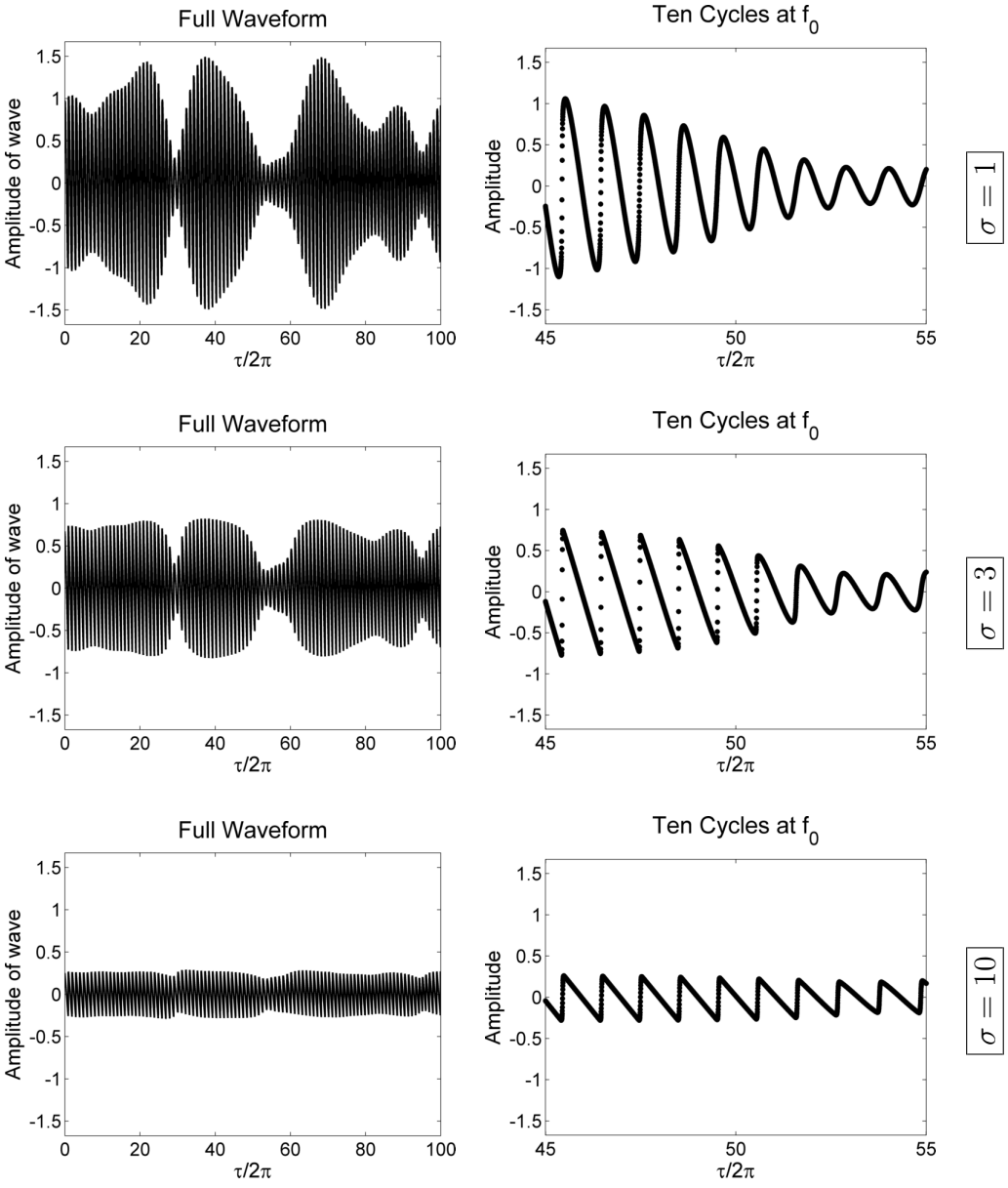

Figure 5.3 (continued).

Narrowband (10% Bandwidth) Source

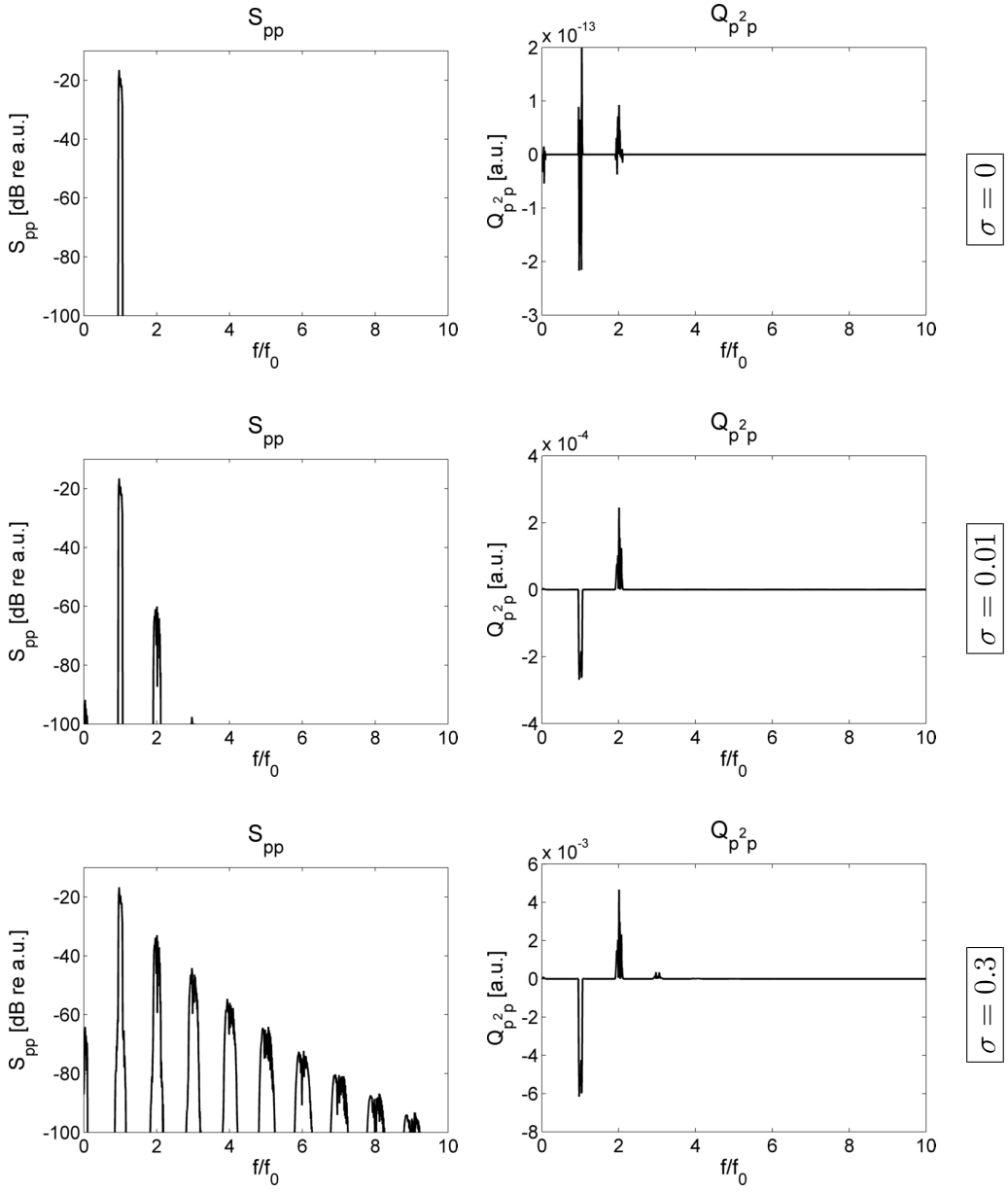

Figure 5.3 (continued).

Narrowband (10% Bandwidth) Source

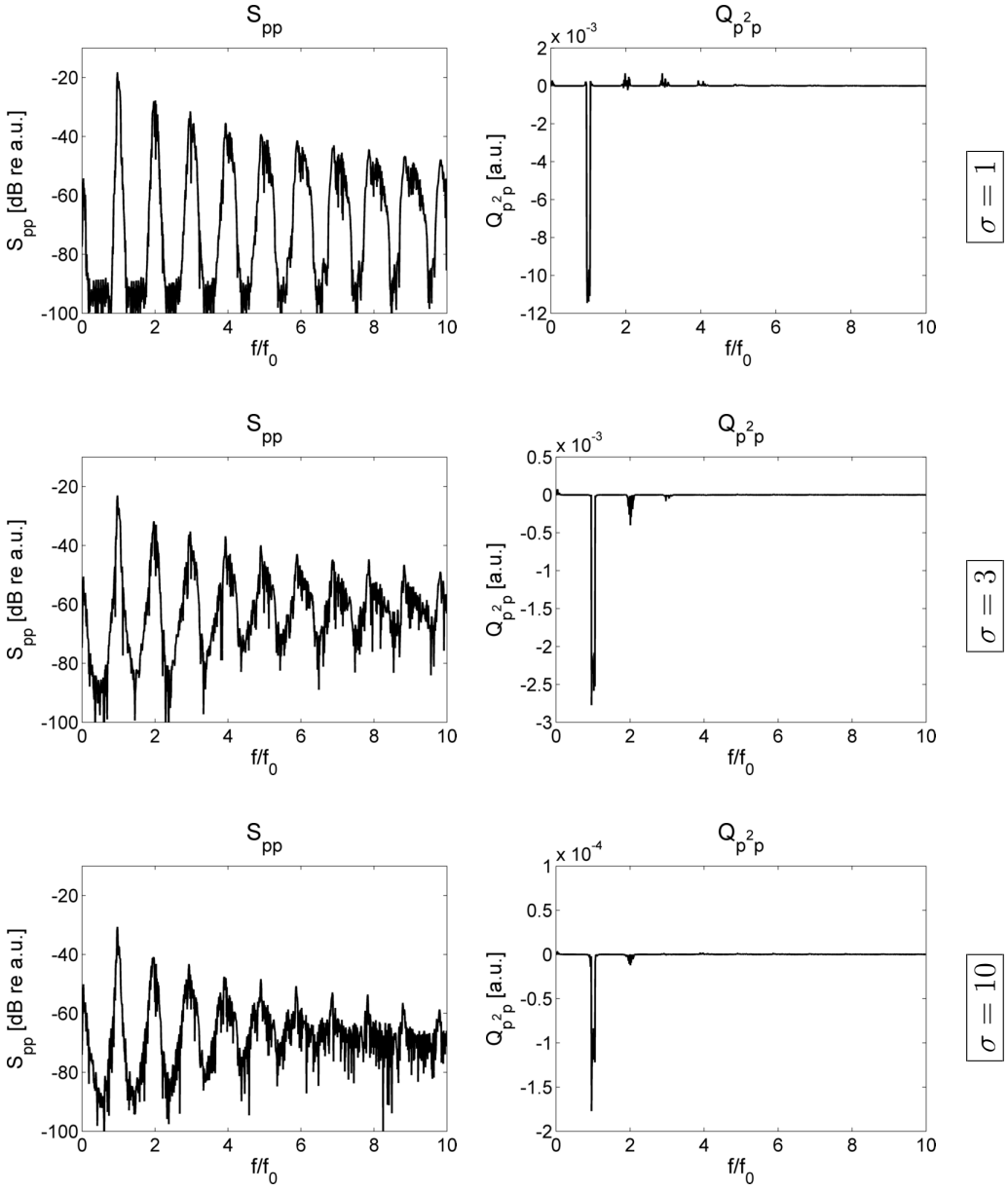

Figure 5.3 (continued).

Narrowband (10% Bandwidth) Source

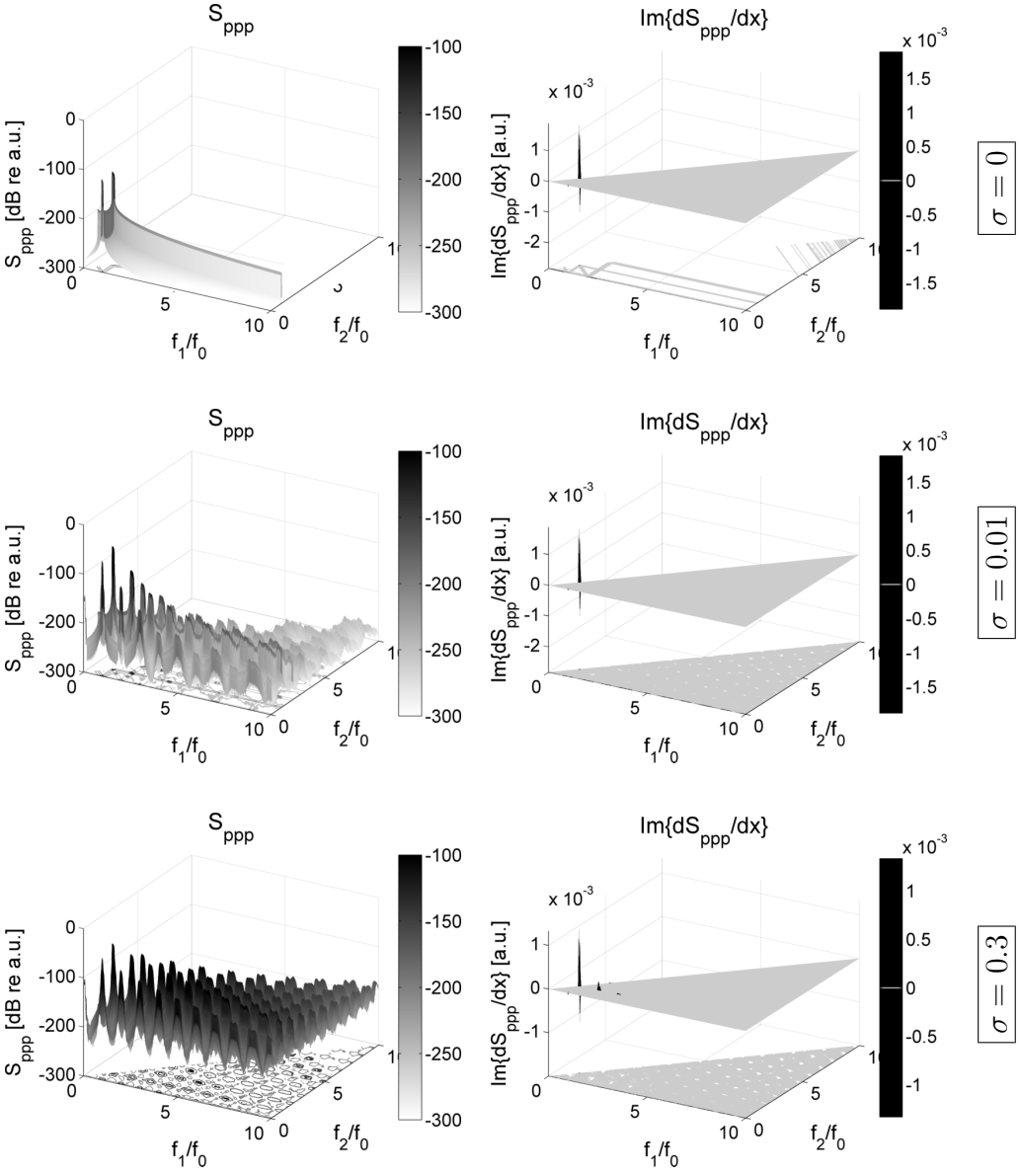

Figure 5.3 (continued).

Narrowband (10% Bandwidth) Source

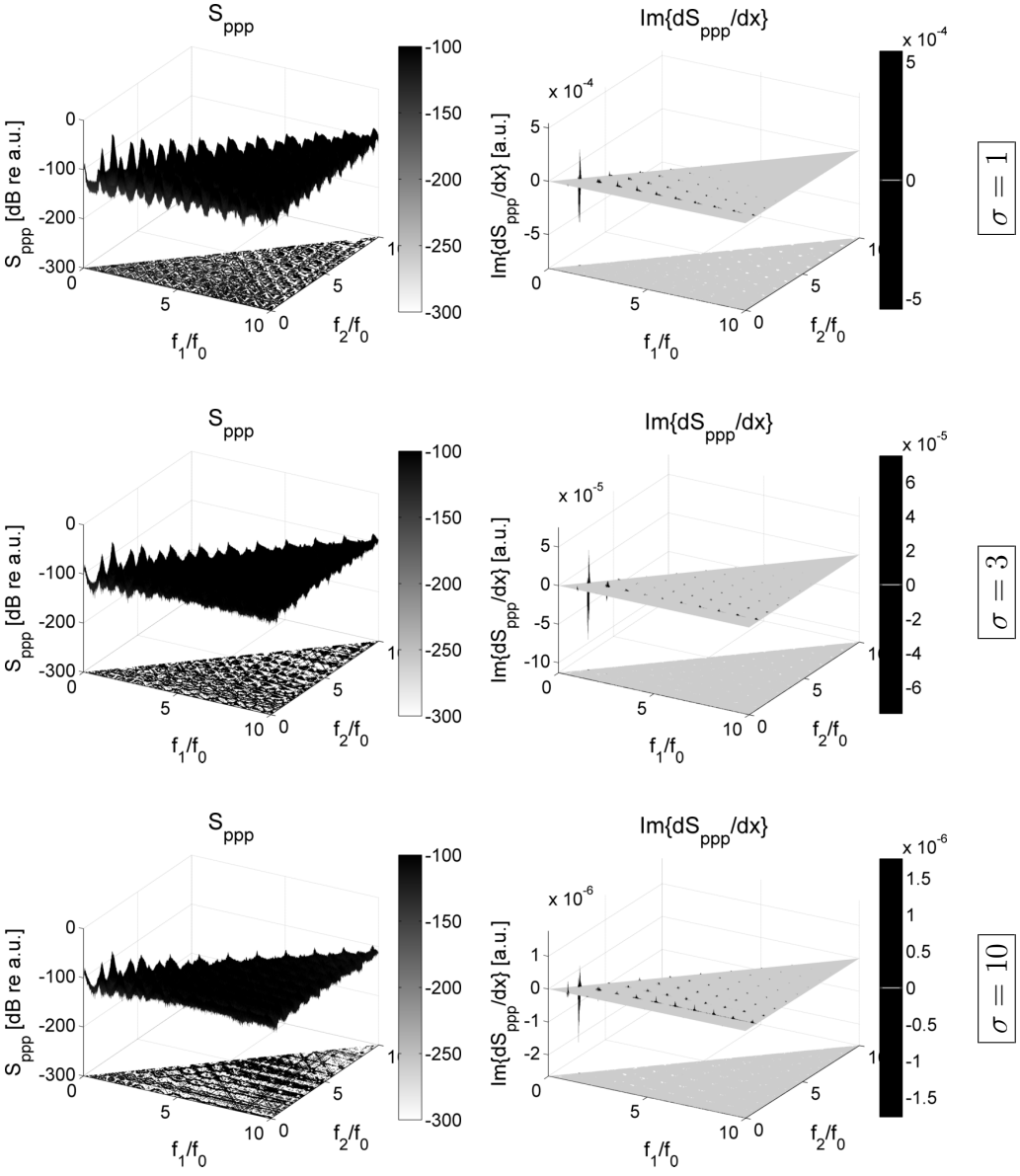

Figure 5.3 (continued).

Narrowband (10% Bandwidth) Source

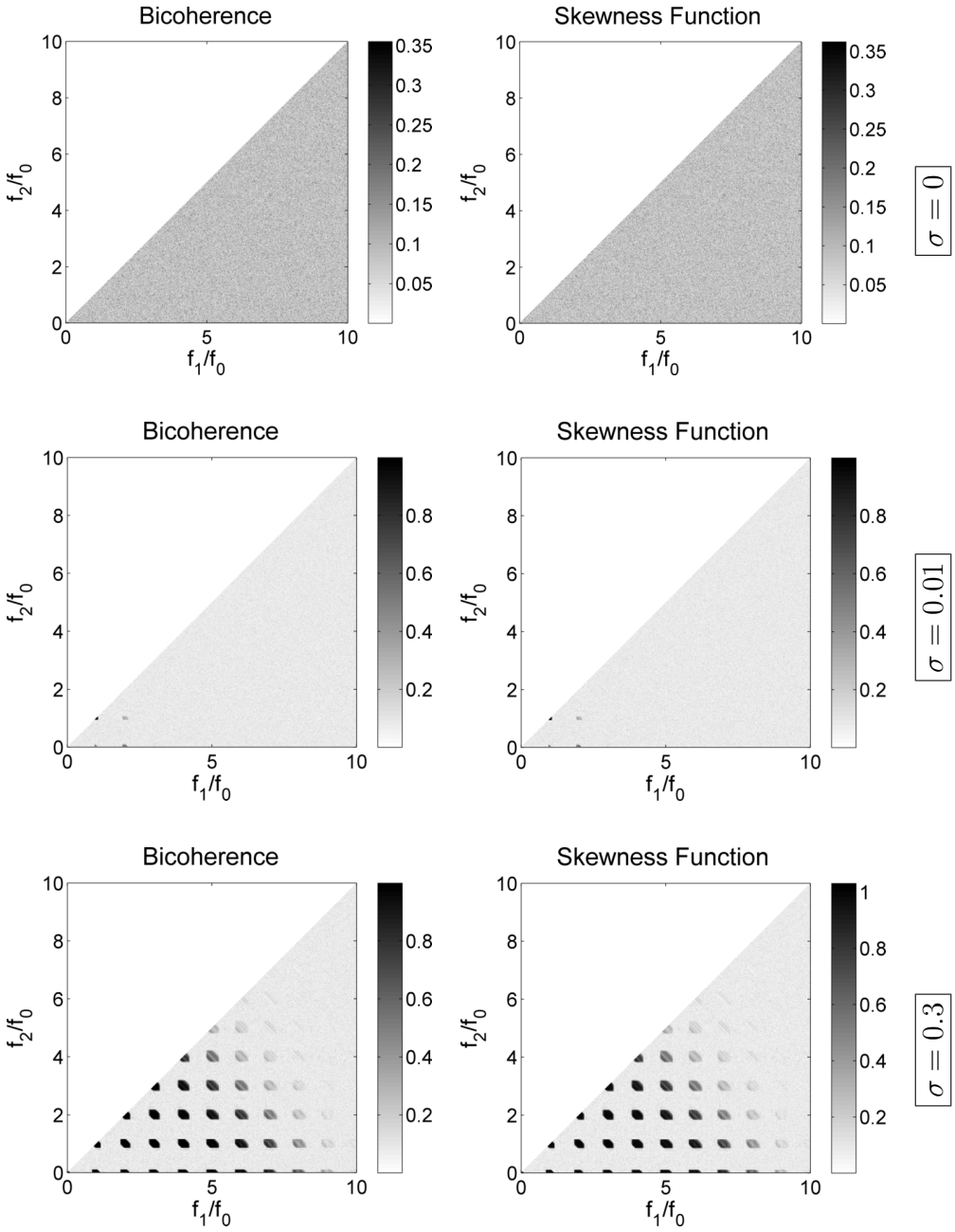

Figure 5.3 (continued).

Narrowband (10% Bandwidth) Source

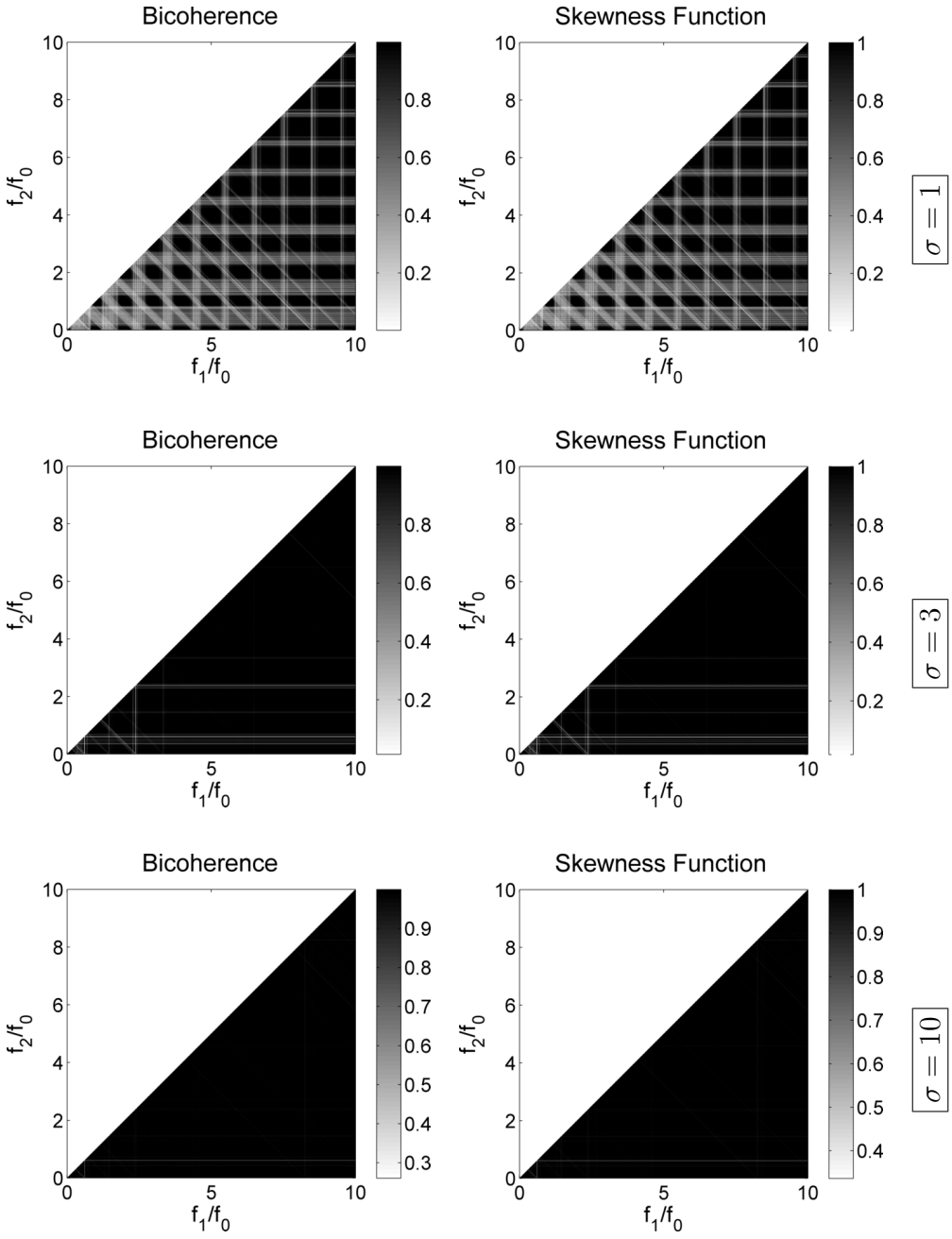

Figure 5.3 (continued).

5.4 Wideband Noise

We now consider the evolution of a waveform with 100% bandwidth at the source. That is, frequencies here range from $0.5f_0$ to $1.5f_0$. Plots of waveforms and spectra are given in Fig. 5.4.

The waveform begins with a highly variable envelope, but as the large amplitude swings are attenuated through nonlinear propagation, the waveform eventually reaches a relatively even peak-to-peak amplitude.

As the wave propagates, the power spectrum evolves rapidly into a continuous spectrum of wideband noise at all frequencies. Notice also the "difference frequencies" that appear in the band $0 \leq f/f_0 \leq 0.5$ beginning at $\sigma = 0.3$. There is a qualitative difference in the quad-spectral density compared with that for the narrowband noise source (Fig. 5.3). Beyond $\sigma = 1$, the prominently positive values of Q_{p^2p} in Fig. 5.4 at frequencies $f/f_0 < 0.5$ indicate that these difference frequencies are receiving significant energy input from the source frequencies, and at $\sigma = 1$ the values of Q_{p^2p} for the difference frequencies are comparable to those for the sum frequencies. This is not the case for narrowband noise. Moreover, at greater distances only the difference frequencies appear to be benefitting significantly from energy transferred out of the primary frequencies.

As for the bispectrum, distinguishing features near the source rapidly fade as the waveform distorts nonlinearly and the power spectrum broadens substantially, and by $\sigma = 1$ any features originally in the bispectrum are all

but gone. This is not surprising and it has been observed by others [4, 7]. The bispectrum is an indicator of phase coherence between triads of frequency components interacting together through quadratic nonlinearity. Since the medium being modeled (a thermoviscous fluid) is nondispersive and only 1D propagation is considered, all frequency combinations of the form $f_1 + f_2 = f_3$, which covers all possible quadratic interactions, are synchronous nonlinear interactions. In the case of broadband noise, with power spectra such as those computed for $\sigma \geq 1$, there is a continuum of frequency pairs (f_1, f_2) whose nonlinear interactions with frequencies $f_3 = f_1 + f_2$ are synchronous. Ultimately the only distinguishing feature in the bispectrum is the slightly higher values close to $(f_1/f_0, f_2/f_0) = (1, 1)$, due only to the slightly higher efficiency of these nonlinear interactions resulting from the higher spectrum levels in this frequency region.

The derivative of the bispectrum for a wideband source emphasizes low frequency interactions over the high frequency interactions, as is consistent with the shape of the quad-spectral density. Because the initial waveform contains sufficient bandwidth to generate substantial difference frequency components, these difference frequencies then contribute to overall spectral interactions.

The bicoherence and skewness function further confirm this emphasis on spectral interactions at low frequencies. The region of high coherence first spreads toward low frequencies and then later expands to the higher frequencies. Note also that the increased bandwidth in Fig. 5.4 causes the normalized

bispectra to saturate faster than in the narrowband case shown in Fig. 5.3.

Wideband (100% Bandwidth) Source

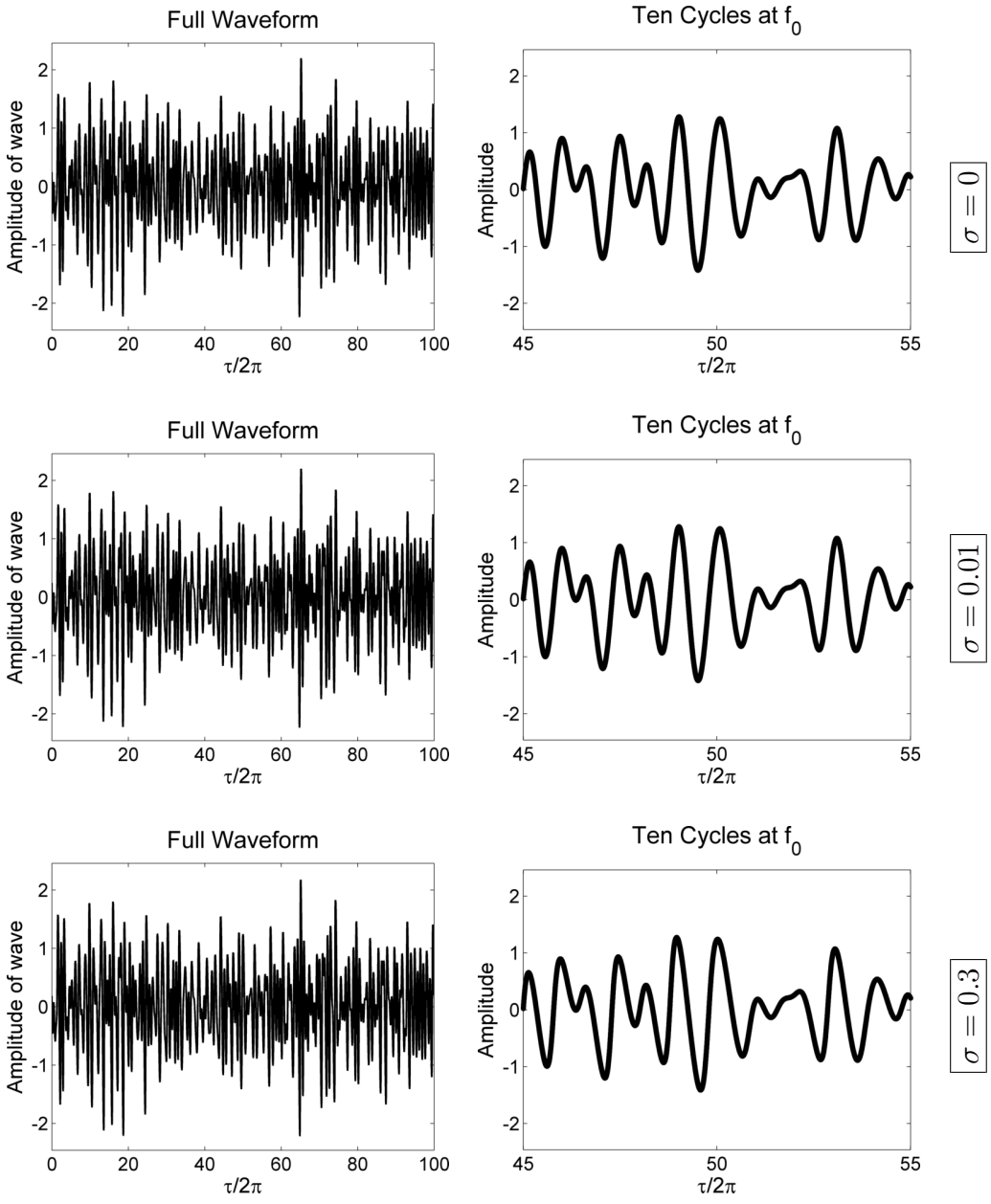

Figure 5.4: Waveforms and spectra for waves radiated by a wideband source.

Wideband (100% Bandwidth) Source

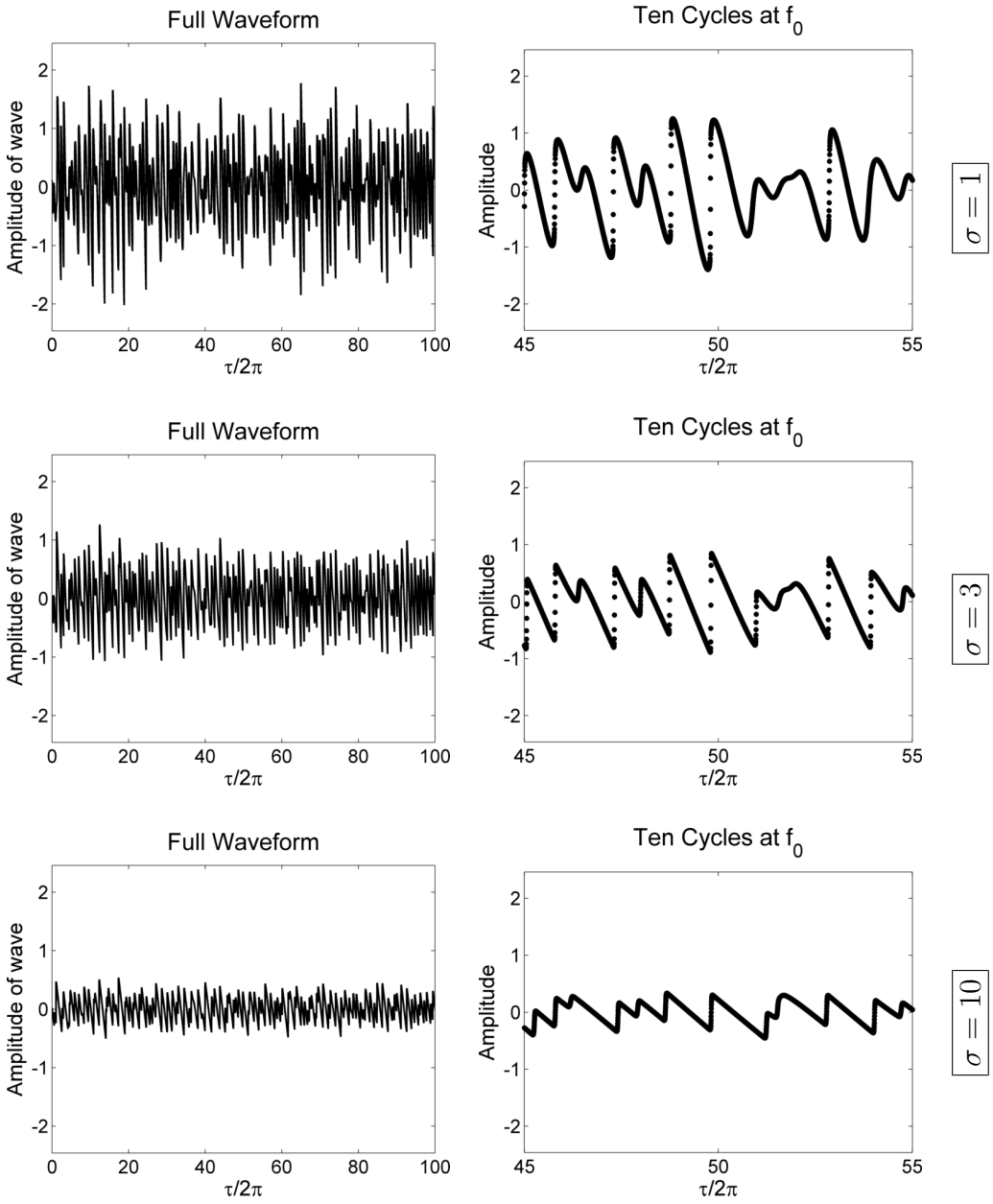

Figure 5.4 (continued).

Wideband (100% Bandwidth) Source

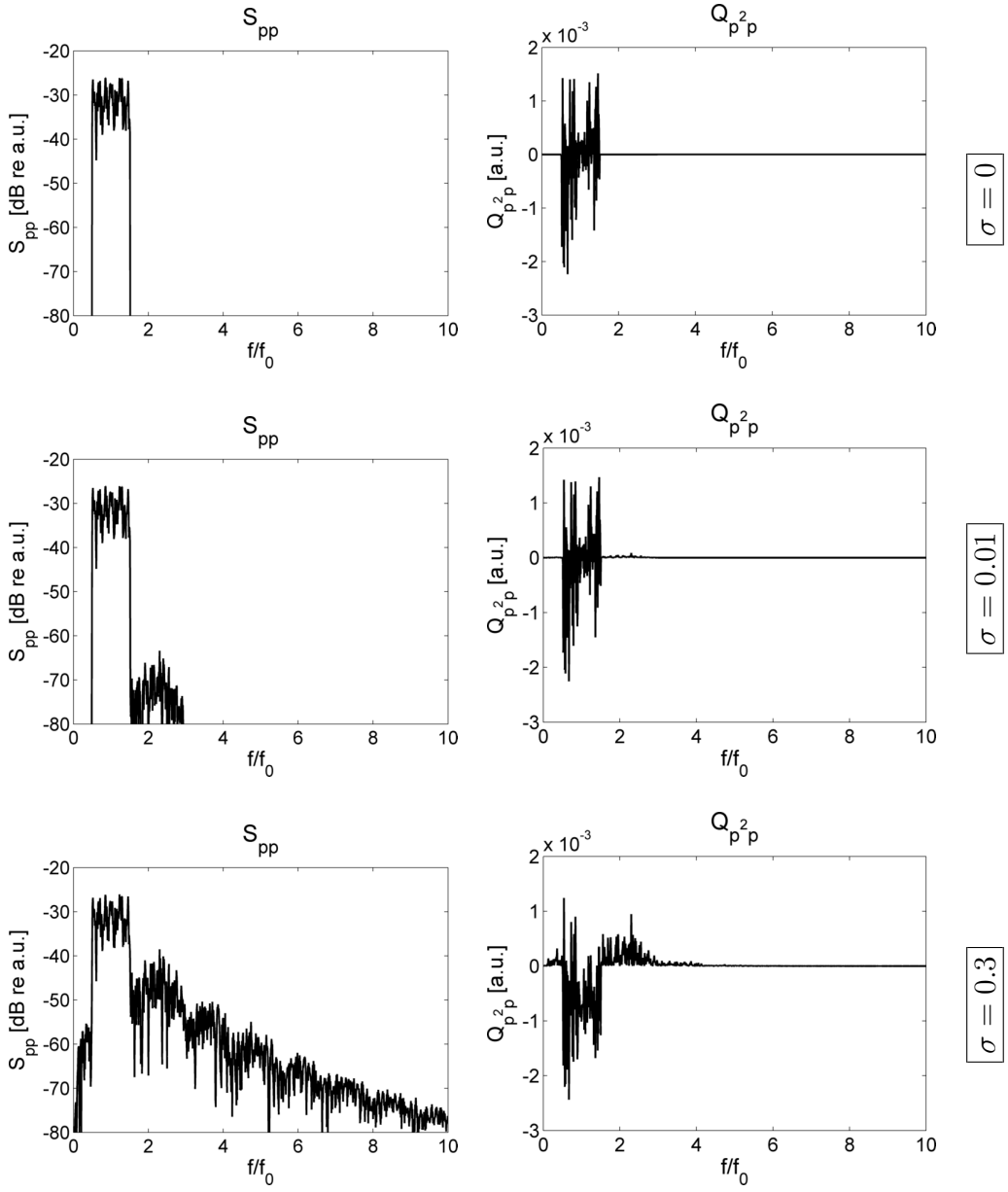

Figure 5.4 (continued).

Wideband (100% Bandwidth) Source

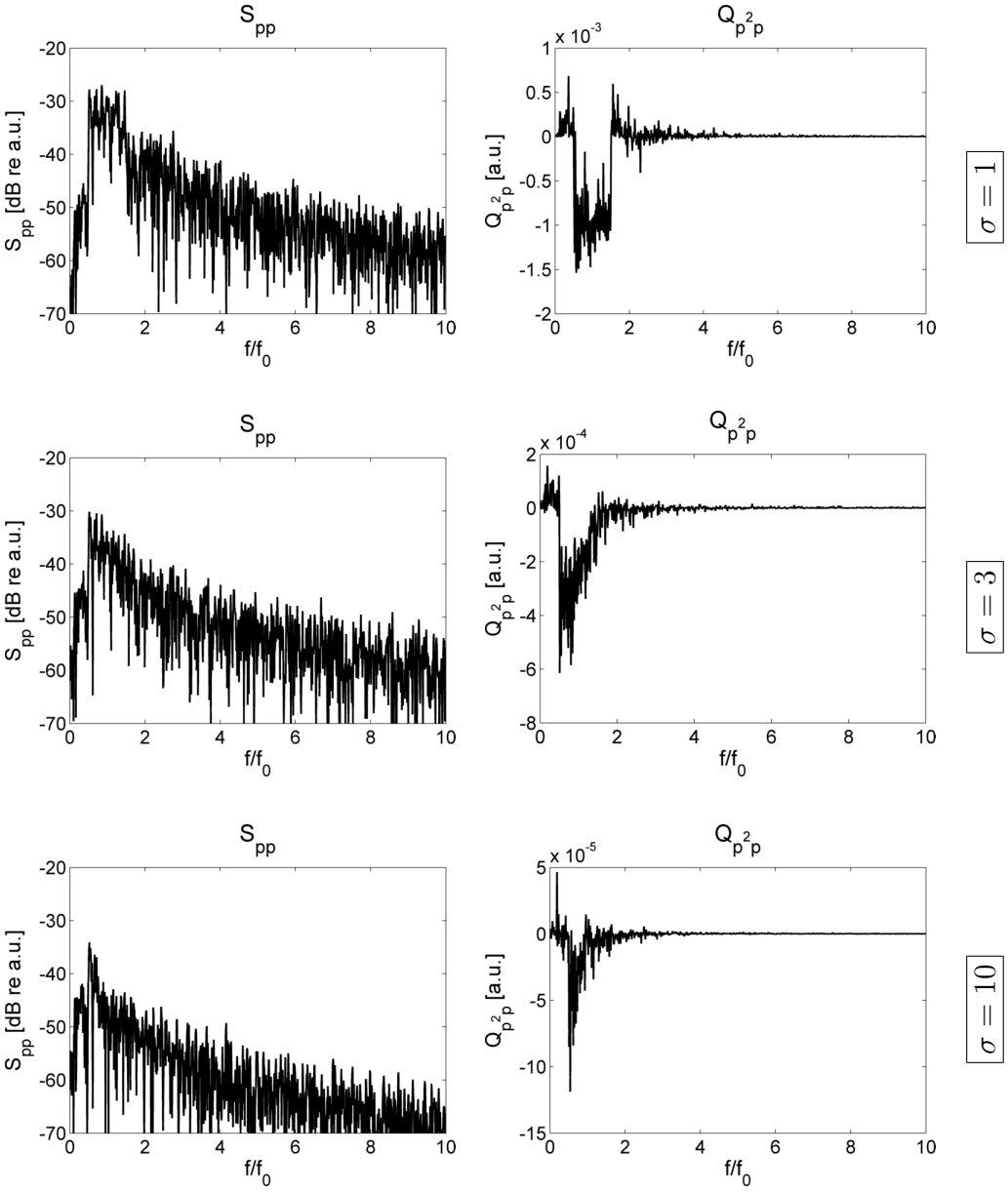

Figure 5.4 (continued).

Wideband (100% Bandwidth) Source

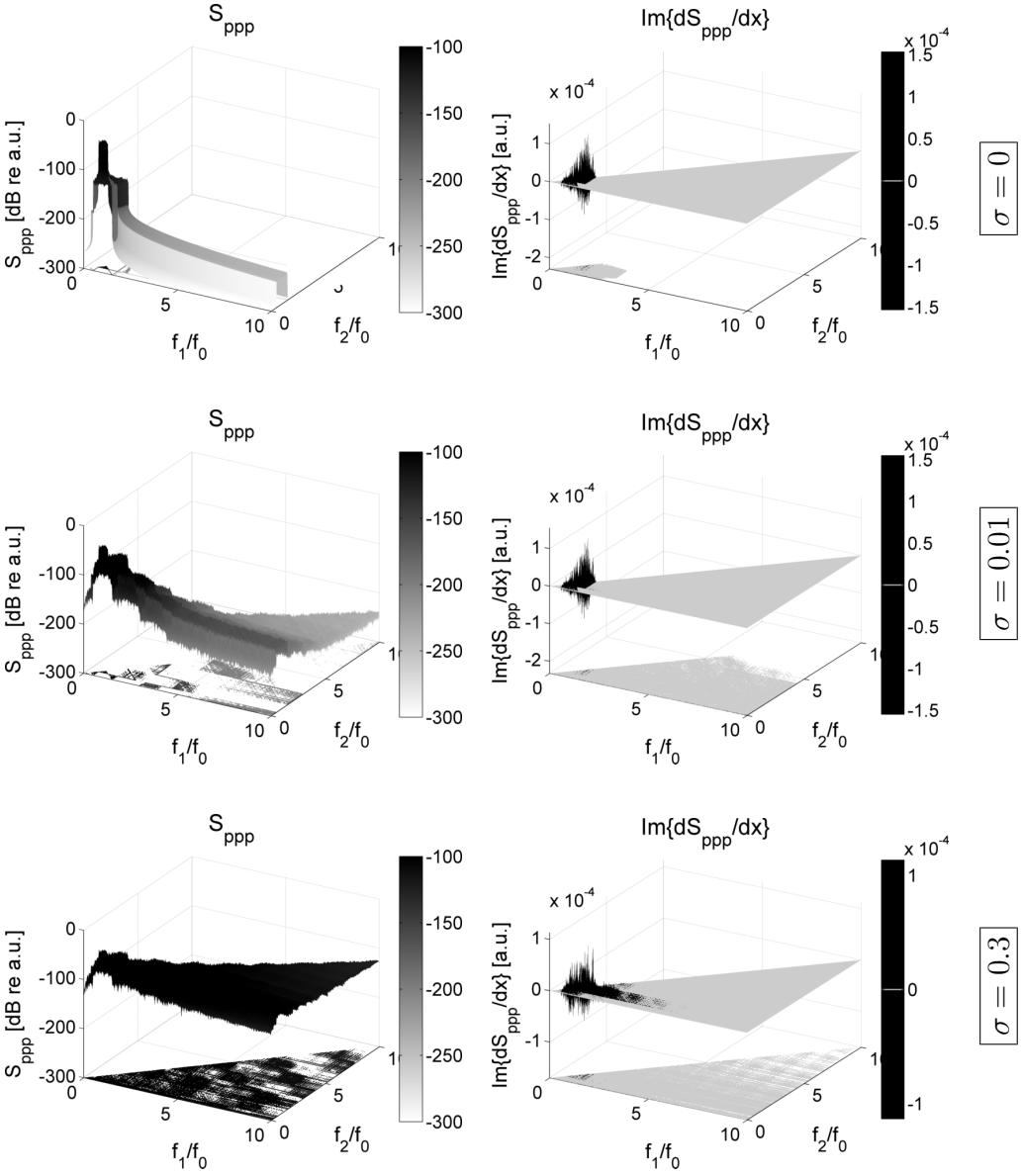

Figure 5.4 (continued).

Wideband (100% Bandwidth) Source

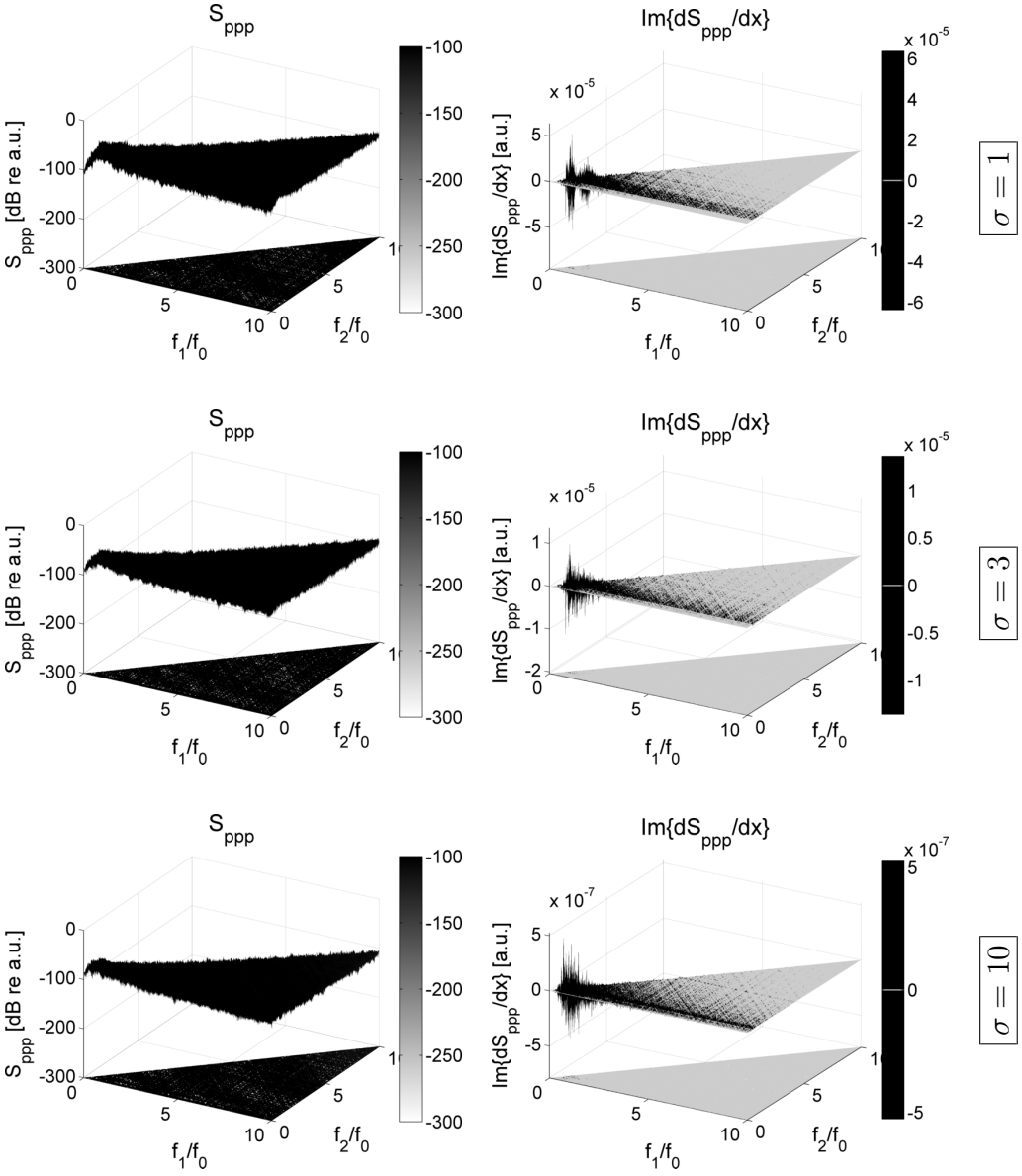

Figure 5.4 (continued).

Wideband (100% Bandwidth) Source

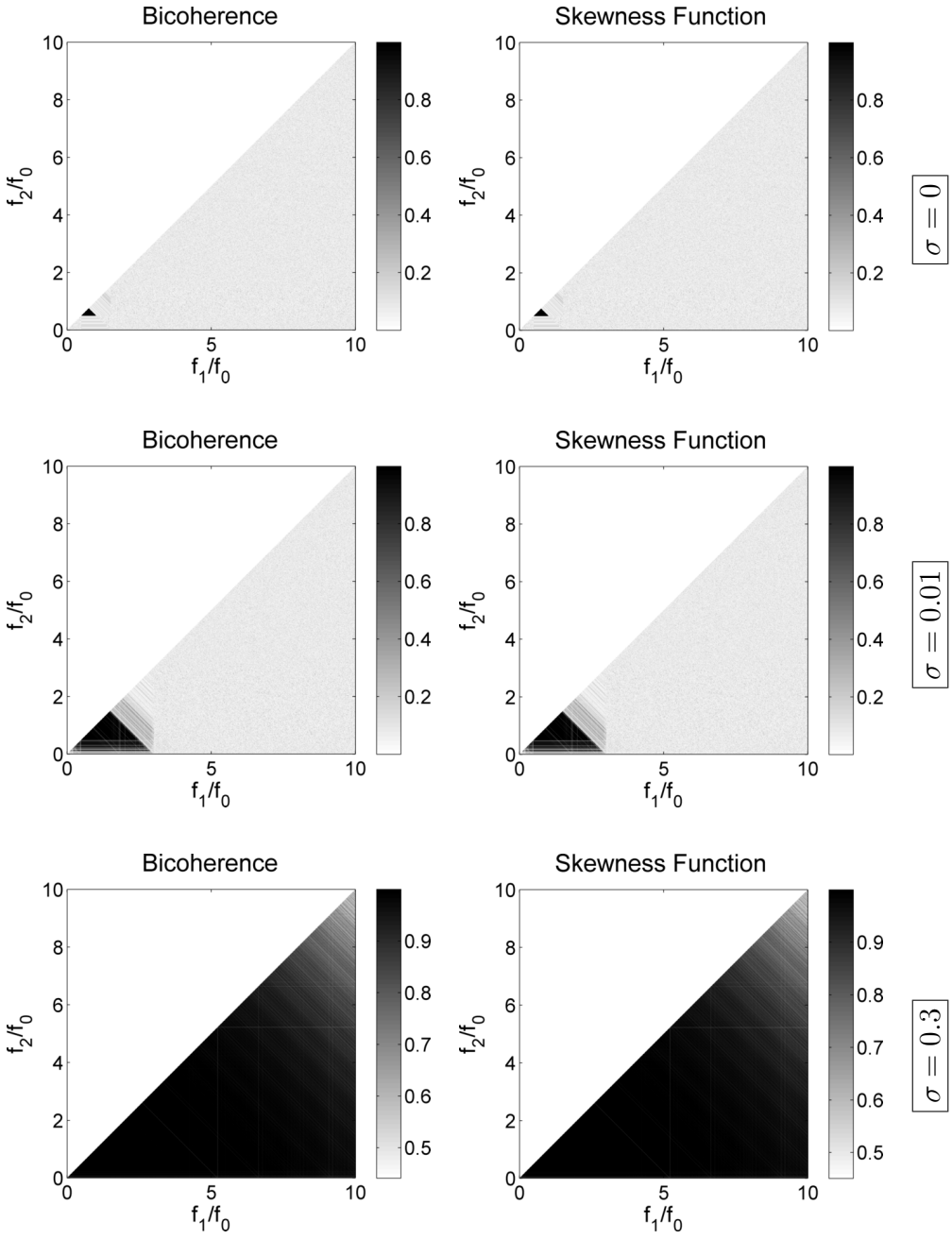

Figure 5.4 (continued).

Wideband (100% Bandwidth) Source

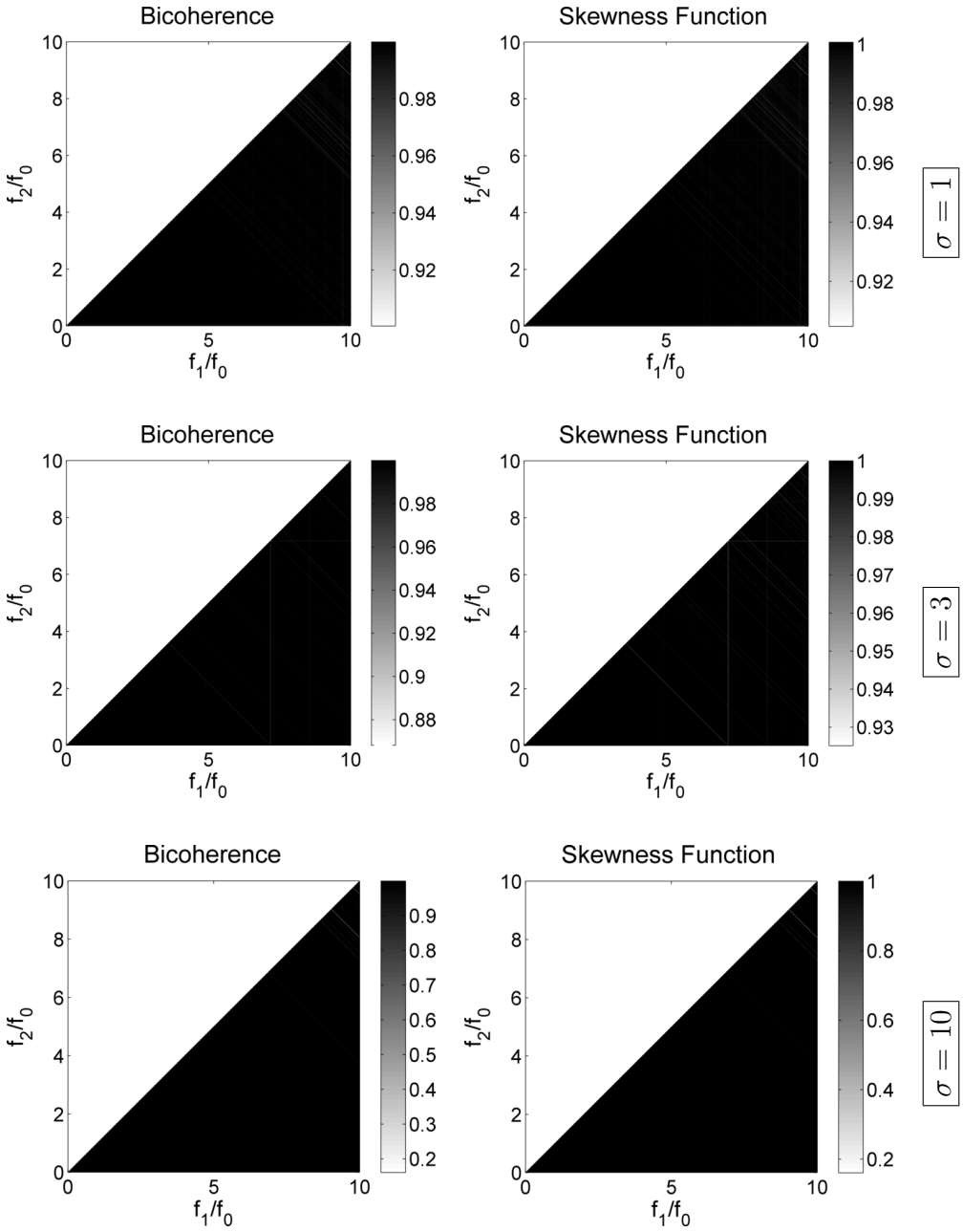

Figure 5.4 (continued).

Chapter 6

Conclusion

In this chapter we review topics covered in this thesis and the results of our calculations, and we address possible ways to expand upon the current research.

6.1 Conclusions

The purpose of this thesis was to present higher order spectra in the context of acoustics, relate the bispectrum to nonlinear sound propagation, and provide examples of bispectra for representative waveforms.

Chapter 1 provided the introduction and literature review. Analytic nonlinear propagation models exist for sinusoids, but with more complicated waveforms, such as jet engine noise, numerical methods are necessary. The bispectrum may be helpful in evaluating the nonlinearity of such sources, but in order for such analysis to be useful, bispectral attributes for known waveforms must be established.

Formulas for the bispectrum were presented in Chap. 2. More details on higher-order spectra can be found in the text by Nikias and Petropulu [16]. The bispectrum can be calculated from covariance functions or from Fourier

transforms, as is also true with power spectral density. However, the bispectrum maintains phase information that can be used to indicate nonlinearity and highlight relationships between frequencies.

It was also noted that the bispectrum can be normalized in multiple ways, and thus the "bicoherence" does not mean the same thing to all people. Although Kim and Powers [23] used a normalization that provides a convenient result between 0 and 1, Hinich and Wolinsky [24] have observed that the normalization of Kim and Powers varies with record length and cannot be considered as a rigorous statistical measure. For completeness, both normalizations were used in this thesis: "bicoherence" to represent the normalization of Kim and Powers, and "skewness function" to represent the normalization of Hinich and Wolinsky.

In Chap. 3, the evolution of power and bispectral densities was discussed. As Morfey and Howell introduced [1] and Falco further explored [2], the quad-spectral density Q_{p^2p} quantifies energy transfer into and out of frequency bands of the signal's spectrum. A similar derivation was carried out in this thesis for the bispectrum to find the derivative of the bispectrum dS_{ppp}/dx. The chapter concluded with a perturbation solution for Q_{p^2p} near the source of an initially sinusoidal wave.

Chapter 4 discussed issues concerning the signal processing employed in this thesis, including waveform generation and analysis. The numerical simulations of wave propagation were accomplished with a code that solves the Burgers equation in the time domain. Numerical calculations of the quad-

spectral density for radiation from a monofrequency source were compared with perturbation solutions derived in Chap. 3 in order to verify the computational procedure. Guidelines were provided for numerically calculating a variety of spectral quantities.

Chapter 5 presented graphical results from the numerical simulations described in Chap. 4. Each section of the chapter considered a different source waveform: monofrequency, bifrequency, narrowband noise, and wideband noise. Each case included the calculation of power spectral density, quad-spectral density, bispectrum, spatial derivative of the bispectrum, bicoherence, and skewness function at several distances chosen to highlight the evolution of the waveforms and spectra.

For the monofrequency, bifrequency, and narrowband sources, all energy in the propagating waveform is originally derived from a small band of source frequencies. As a result, the quad-spectral density prior to shock formation is characterized by a large negative spike in the source frequency area of the spectrum and smaller positive spikes at the other harmonics. This pattern correctly indicates that harmonic generation in the preshock region occurs mainly at the expense of energy leaving the source frequency component(s). The value of Q_{p^2p} at the second harmonic becomes negative in the sawtooth region, which indicates that the second harmonic behaves more like a source of energy for other harmonics at this stage of propagation.

The bispectrum displays interactions at all possible sum and difference frequencies interacting in its corresponding waveform. In the early stages of

propagation, energy exists only at the source frequency(ies) and a few harmonics. As a result, bispectra have low values at the upper harmonics until nonlinear propagation causes energy to expand to those frequency regions. After shock formation, peaks achieve a nominally equal value at all sum and difference frequencies formed by harmonics of the source frequency(ies). In the monofrequency case, spikes are observed at all integer multiples of the source frequency, whereas in the bifrequency case, those spikes are transformed into clusters of spikes around harmonics of the mean frequency. In the narrowband case, broad peaks appear around harmonics of the mean frequency, and in the wideband case, plateaus appear in the same frequency locations. In the sense of general shape, the appearance of the bispectrum at sum- and difference-frequency regions corresponds to what is observed in the power spectrum.

The bispectrum for radiation from a narrowband source (10% bandwidth, just like the bifrequency source) resembles quite closely that for the bifrequency source, except that the former appears to have a smoother texture. This variation occurs due to a continuous distribution of frequencies, which provides more frequencies for spectral interaction.

In the case of broadband noise (100% bandwidth) we seem to recover results for the bispectrum much like those reported by Gee et al. [4, 7]. Specifically, beyond the shock formation distance the magnitude of the bispectrum is roughly uniform over the entire frequency space, even if monotonically decreasing slightly away from the point $(f_1/f_0, f_2/f_0) = (1, 1)$ in the bifrequency plane, where f_0 is the center frequency of the noise source. For comparison,

the maximum of the power spectrum is located where $f/f_0 = 1$. The reason for the uniform shape of the bispectrum in the case of broadband noise is that all frequency components have comparable amplitudes and interact resonantly in the absence of dispersion. The bispectrum, being defined in such a way that it highlights resonant nonlinear interactions, therefore yields values similar in magnitude for all frequency pairs.

In the absence of prominent distinguishing features in the bispectra for broadband noise, further information can be found from the derivative of the bispectrum with respect to the coordinate along the direction of propagation. It was observed that this derivative is large in regions near $(f_1/f_0, f_2/f_0) = (1, 1)$ in the bifrequency plane. This result is also not surprising, that the evolution of the bispectrum would be most rapid for interactions of frequency pairs in which one falls inside the band of frequencies in the source spectrum, as these frequency components always have the greatest amplitude and serve as primary waves.

6.2 Future Work

The current project was limited in scope to basic bispectral calculations for nonlinearly propagated noise in one dimension, and this research could go in several different directions.

In this thesis we have computed raw bispectra, but it may be informative to also consider levels of statistical significance for each peak. Hinich [37] has developed tests for nonlinearity based on bispectra, and the results are cal-

ibrated to produce significance percentages. Such an approach would attach a more statistically meaningful set of numbers to the observed peaks.

One may also consider propagation geometries beyond one dimension. In one-dimensional propagation, all wavenumbers point in the same direction, and thus all harmonic interactions are resonant. If, for example, the sound were to strike a reflective surface, the interaction of direct and reflected waves can result in asynchronous nonlinear interactions due to phase fronts that approach one another at an angle. Bispectral analysis may show interesting results for such an environment, e.g., for intense sound fields in enclosures or resonators.

Another step would be to compare bispectra calculated from numerical simulation versus those obtained from experimental data. Waveforms in this thesis have been constructed from power spectral densities with flat amplitude and random phase. Other waveforms could be generated in a similar manner with different spectral density shapes in order to approximate levels observed in real jet noise. Since bispectra reveal phase relationships within waves, this approach could provide insight into the nature of phase relationships near a jet engine source.

Bibliography

[1] C. L. Morfey and G. P. Howell, "Nonlinear propagation of aircraft noise in the atmosphere", AIAA J. 986–992 (1981).

[2] L. E. Falco, "Single-point nonlinearity indicators for the propagation of high amplitude acoustic signals", Ph.D. thesis, The Pennsylvania State University (2007).

[3] K. L. Gee, T. B. Gabrielson, A. A. Atchley, and V. W. Sparrow, "Preliminary analysis of nonlinearity in F/A-18E/F noise propagation", AIAA (2004), Paper No. AIAA-2004-3009.

[4] K. L. Gee, A. A. Atchley, L. E. Falco, T. B. Gabrielson, and V. W. Sparrow, "Bispectral analysis of high-amplitude jet noise", AIAA (2005), Paper No. AIAA-2005-2937.

[5] K. L. Gee, V. W. Sparrow, A. A. Atchley, and T. B. Gabrielson, "On the perception of crackle in high-amplitude jet noise", AIAA J. **45**, 593–598 (2007).

[6] K. L. Gee, V. W. Sparrow, M. M. James, J. M. Downing, C. M. Hobbs, T. B. Gabrielson, and A. A. Atchley, "The role of nonlinear effects in the propagation of noise from high-power jet aircraft", J. Acoust. Soc. Am. **123**, 4082–4093 (2008).

[7] K. L. Gee, A. A. Atchley, L. E. Falco, M. R. Shepherd, L. S. Ukeiley, B. J. Jansen, and J. M. Seiner, "Bicoherence analysis of model-scale jet noise", JASA Express Letters **128**, EL211–EL216 (2010).

[8] J. E. Ffowcs Williams, J. Simson, and V. J. Virchis, "'Crackle': an annoying component in jet noise", Journal of Fluid Mechanics **71**, 251–271 (1975).

[9] J. H. Ginsberg and M. F. Hamilton, "Computational methods", in *Nonlinear Acoustics*, edited by M. F. Hamilton and D. T. Blackstock, Chapter 11, 309–341 (Academic Press, San Diego) (1998).

[10] F. H. Fenlon, "A recursive procedure for computing the nonlinear spectral interactions of progressive finite-amplitude waves in nondispersive fluids", J. Acoust. Soc. Am. **50**, 1299–1312 (1971).

[11] A. Korpel, "Frequency approach to nonlinear dispersive waves", J. Acoust. Soc. Am. **67**, 1954–1958 (1980).

[12] F. M. Pestorius and D. T. Blackstock, "Propagation of finite-amplitude noise", in *Finite-Amplitude Wave Effects in Fluids*, edited by L. Bjørnø, 24–29 (IPC Science and Technology Press, Guildford, Surrey, England) (1974).

[13] Y.-S. Lee and M. F. Hamilton, "Time-domain modeling of pulsed finite-amplitude sound beams", J. Acoust. Soc. Am. **97**, 906–917 (2005).

[14] R. O. Cleveland, M. F. Hamilton, and D. T. Blackstock, "Time-domain modeling of finite-amplitude sound in relaxing fluids", J. Acoust. Soc. Am. **99**, 3312–3318 (1996).

[15] R. O. Cleveland, J. P. Chambers, H. E. Bass, R. Raspet, D. T. Blackstock, and M. F. Hamilton, "Comparison of computer codes for the propagation of sonic boom waveforms through isothermal atmospheres", J. Acoust. Soc. Am. **100**, 3017–3027 (1996).

[16] C. L. Nikias and A. P. Petropulu, *Higher-Order Spectra Analysis: A Nonlinear Signal Processing Framework* (PTR Prentice-Hall, Inc., Englewood Cliffs, New Jersey) (1993).

[17] J. S. Bendat and A. G. Piersol, *Random Data: Analysis and Measurement Procedures*, 2nd edition (Wiley-Interscience, New York) (1986).

[18] C. L. Nikias and M. R. Raghuveer, "Bispectrum estimation: A digital signal processing framework", Proc. IEEE **75**, 869–891 (1987).

[19] M. A. Wolinsky, "Invitation to the bispectrum", Technical Report ARL-TR-88-7, Applied Research Laboratories, The University of Texas at Austin (1988).

[20] K. Hasselmann, W. Munk, and G. MacDonald, "Bispectra of ocean waves", in *Time Series Analysis*, edited by M. Rosenblatt, Chapter 8, 125–139 (Wiley, New York) (1963).

[21] D. R. Brillinger, "An introduction to polyspectra", Ann. Math. Statist. **36**, 1351–1374 (1965).

[22] R. A. Haubrich, "Earth noise, 5 to 500 millicycles per second", J. Geophys. Res. **70**, 1415–1427 (1965).

[23] Y. C. Kim and E. J. Powers, "Digital bispectral analysis and its applications to nonlinear wave interactions", IEEE Trans. Plasma Sci. **PS-7**, 120–131 (1979).

[24] M. J. Hinich and M. Wolinsky, "Normalizing bispectra", J. Statist. Plann. Inference **130**, 405–411 (2005).

[25] M. J. Hinich, "Testing for Gaussianity and linearity of a stationary time series", J. Time. Ser. Anal. **3**, 169–176 (1982).

[26] M. J. Hinich and C. S. Clay, "The application of the discrete Fourier transform in the estimation of power spectra, coherence, and bispectra of geophysical data", Rev. Geophys. **6**, 347–363 (1968).

[27] M. J. Hinich and H. Messer, "On the principal domain of the discrete bispectrum of a stationary signal", IEEE Trans. Signal Process. **43**, 2130–2134 (1995).

[28] D. T. Blackstock, M. F. Hamilton, and A. D. Pierce, "Progressive waves in lossless and lossy fluids", in *Nonlinear Acoustics*, edited by M. F. Hamilton and D. T. Blackstock, Chapter 4, 64–150 (Academic Press, San Diego) (1998).

[29] M. F. Hamilton, "Fundamentals and applications of nonlinear acoustics", in *Nonlinear Wave Propagation in Mechanics*, edited by T. W. Wright, 1–28 (American Society of Mechanical Engineers, New York) (1986).

[30] R. T. Beyer, *Nonlinear Acoustics* (Acoustical Society of America, Woodbury, NY) (1997).

[31] K. A. Naugolnykh and L. A. Ostrovsky, *Nonlinear Wave Processes in Acoustics*, Cambridge Texts in Applied Mathematics (Cambridge University Press, New York) (1998).

[32] D. T. Blackstock, "Connection between the Fay and Fubini solutions for plane sound waves of finite amplitude", J. Acoust. Soc. Am. **39**, 1019–1026 (1966).

[33] P. Menounou and D. T. Blackstock, "A new method to predict the evolution of the power spectral density for a finite-amplitude sound wave", J. Acoust. Soc. Am. **115**, 567–580 (2004).

[34] S. N. Gurbatov, A. N. Malakhov, and N. V. Pronchatov-Rubtsov, "Evolution of higher-order spectra of nonlinear random waves", Izv. Vyssh. Uchebn. Zaved. **29**, 691–697 (1986).

[35] F. H. Fenlon, "Approximate methods for predicting the performance of parametric sources at high acoustic Reynolds numbers", in *Finite-Amplitude Wave Effects in Fluids*, edited by L. Bjørnø, 160–167 (IPC Science and Technology Press, Guildford, Surrey, England) (1974).

[36] S. Elgar and R. T. Guza, "Statistics of bicoherence", IEEE Trans. Acoust. Speech Signal Process. **36**, 1667–1668 (1988).

[37] M. J. Hinich, E. M. Mendes, and L. Stone, "Detecting nonlinearity in time series: Surrogate and bootstrap approaches", Studies in Nonlinear Dynamics and Econometrics **9** (2005), Article 3.

Vita

David E. Gagnon was born in Patuxent River, Maryland. He achieved Eagle Scout rank in 2001 and graduated as a valedictorian from Winter Park High School in 2002. At Virginia Tech, he participated in the Hillcrest Honors Community while pursuing bachelor's degrees in both electrical engineering and music. He also performed with the New River Valley Symphony and served as principal cellist for three of those years. Through the Horton Honors Scholarship, he studied in Germany and Austria for the summer and fall of 2005. After graduation in 2007, David enrolled at The University of Texas at Austin and began work at Applied Research Laboratories through the McKinney Fellowship in Acoustics. During graduate school, he was very involved with the Texas Graduate Christian Fellowship, where he met Nicole Ryan. They were married in 2010, and they have moved to Houston for David's new job at HFP Acoustical Consultants, Inc.

Permanent address: 404 Oxford St., Apt. 1116
Houston, Texas 77007

This thesis was typeset with LaTeX[†] by the author.

[†]LaTeX is a document preparation system developed by Leslie Lamport as a special version of Donald Knuth's TeX Program.